



# Durham E-Theses

---

## *Trapping molecules using photostop*

EARDLEY, JACK,STEWART

### How to cite:

---

EARDLEY, JACK,STEWART (2019) *Trapping molecules using photostop*, Durham theses, Durham University. Available at Durham E-Theses Online: <http://etheses.dur.ac.uk/13166/>

### Use policy

---

The full-text may be used and/or reproduced, and given to third parties in any format or medium, without prior permission or charge, for personal research or study, educational, or not-for-profit purposes provided that:

- a full bibliographic reference is made to the original source
- a [link](#) is made to the metadata record in Durham E-Theses
- the full-text is not changed in any way

The full-text must not be sold in any format or medium without the formal permission of the copyright holders.

Please consult the [full Durham E-Theses policy](#) for further details.

# Trapping molecules using photostop

Jack Stewart Eardley

Submitted for the degree of Doctor of Philosophy

March 2019

## Abstract

Successful magnetic trapping of both SH at a density of  $2.4 \times 10^5 \text{ cm}^{-3}$  and atomic oxygen at a density of  $3000 \pm 900 \text{ cm}^{-3}$  has been demonstrated with respective trapping lifetimes of  $40 \pm 10 \text{ ms}$  and  $82 \pm 3 \text{ ms}$  inside a 0.41 T deep, anti-Helmholtz configuration magnetic trap.

To achieve trapping of these species, a stable precursor was cooled by supersonic expansion in a molecular beam and photodissociated in such a way as to match and oppose a photofragments recoil speed to the precursors molecular beam speed. This process is called photostop.

Velocity-map images have been taken of photostop of atomic oxygen from photodissociation of  $\text{NO}_2$  in a molecular beam. They show that atomic oxygen can be photostopped from a variety of NO photodissociation co-fragments with a suitably broad molecular-beam velocity-distribution. Although photostop is simple and cheap to use, the trapping lifetimes and densities that have been achieved in this thesis are not competitive compared to other methods of trapping similar molecular species. The main problem that presents universally in photostop experiments is due to the large number of fast molecules from the supersonic expansion that pass through the trap after the photostop event. Only a small fraction of the molecules in the molecular beam are stopped and the remaining ones cause significant trap loss through high energy elastic collisions with trapped species.

Work has been carried out to develop the cavity-enhanced laser-induced-fluorescence (CELIF) technique to be used more widely in the cold molecules field. The technique was employed unsuccessfully to measure photostopped SH radicals but was used elsewhere to measure cold SD radicals after Stark deceleration. In addition, the technique has been initially developed for use inside magnetic traps.

Clusters of  $\text{NO} \cdot \text{Ar}_n$  have been studied using  $[1+1']$  REMPI to assess the viability of a new soft-ionisation technique for molecular clusters of atmospheric interest. This work did not show conclusive evidence that  $[1+1']$  REMPI would reduce cluster fragmentation and displayed some interesting but poorly understood data.

# Trapping molecules using photostop

Jack Stewart Eardley

A Thesis presented for the degree of  
Doctor of Philosophy



Department of Chemistry  
University of Durham  
England

March 2019

# Contents

<b>Abstract</b>	
<b>Declaration</b>	<b>iv</b>
<b>1 Background</b>	<b>2</b>
1.1 Fundamental science . . . . .	2
1.1.1 Molecular beams and supersonic expansion . . . . .	3
1.1.2 Laser spectroscopy . . . . .	5
1.1.3 Trapping and guiding fields . . . . .	5
1.2 Relevant prior work . . . . .	5
<b>2 Magnetic trapping of SH radicals</b>	<b>7</b>
2.1 The photostop technique . . . . .	7
2.2 Introduction . . . . .	8
2.3 Experimental . . . . .	9
2.3.1 Pumping and beam speed stability improvements . . . . .	15
2.3.2 Alternative REMPI detection schemes . . . . .	18
2.3.3 Ion counting algorithms . . . . .	20
2.4 Simulation . . . . .	22
2.5 Results and discussion . . . . .	23
2.5.1 Data analysis and error sources . . . . .	23
2.5.2 SH trapping results . . . . .	25
2.6 Conclusions . . . . .	27
<b>3 SH and SD CELIF</b>	<b>29</b>
3.1 SH photostop CELIF experiments . . . . .	29
3.1.1 Experimental . . . . .	29
3.1.2 Results and discussion . . . . .	32
3.1.3 Conclusions . . . . .	34
3.2 SD Stark deceleration CELIF . . . . .	34

3.2.1	Introduction . . . . .	34
3.2.2	Experimental . . . . .	35
3.2.3	Results and discussion . . . . .	36
3.2.4	Conclusions . . . . .	39
3.3	Simulations of CELIF in trapping fields . . . . .	40
3.3.1	Sample simulation results . . . . .	41
<b>4</b>	<b>Atomic oxygen photostop</b>	<b>43</b>
4.1	Introduction . . . . .	43
4.2	Velocity map imaging of oxygen photostop . . . . .	44
4.2.1	Experimental . . . . .	45
4.2.2	Results and discussion . . . . .	48
4.2.3	Conclusions . . . . .	54
4.3	Magnetically trapped oxygen atoms . . . . .	56
4.3.1	Experimental . . . . .	57
4.3.2	Results and discussion . . . . .	59
4.3.3	Conclusions . . . . .	61
<b>5</b>	<b>Unstable cluster detection</b>	<b>64</b>
5.1	Introduction . . . . .	64
5.2	Background . . . . .	64
5.3	Previous work . . . . .	65
5.4	Experimental . . . . .	66
5.4.1	Fitting . . . . .	66
5.5	Results and discussion . . . . .	66
5.6	Conclusion . . . . .	71
<b>6</b>	<b>Conclusions and future work</b>	<b>72</b>
	<b>Appendix</b>	<b>74</b>
<b>A</b>	<b>Basic and Auxiliary Results</b>	<b>74</b>
A.1	Basic Results . . . . .	74
A.1.1	Molecular beam mechanical chopper arm . . . . .	74
<b>B</b>	<b>Derivations</b>	<b>76</b>
B.1	Explanation of oxygen REMPI absolute measurement . . . . .	76
<b>C</b>	<b>Experimental proposals</b>	<b>78</b>
C.1	Super rotor using Photostop and Stark deceleration . . . . .	78
C.1.1	Photostop for creation of quantum state pure high rotational states . . . . .	82

# Declaration

The work in this thesis is based on research largely carried out at the Department of Chemistry, England. No part of this thesis has been submitted elsewhere for any other degree or qualification and it is all my own work unless referenced to the contrary in the text.

The work in this thesis was made possible by a RCUK grant from the EPSRC.

**Copyright © 2019 by Jack Stewart Eardley.**

“The copyright of this thesis rests with the author. No quotations from it should be published without the author’s prior written consent and information derived from it should be acknowledged”.

*Dedicated to*

Dr. John Middleton

# Chapter 1

## Background

This thesis presents a number of experiments which use molecular beams, laser spectroscopy and field potentials to interrogate atoms, molecules and clusters in the gas phase under high vacuum conditions. The first section of this chapter will discuss these tools, as understanding them is essential to understanding this thesis, as well as the ideas behind temperature that are also important to this document.

Cold molecules and atoms are studied for a wide range of reasons by a number of groups around the world. A number of reviews<sup>1-4</sup> and theses<sup>5</sup> have discussed the variety of methods available for creating and working with cold atoms and molecules. Instead of duplicating this work, this report will present the fundamental science necessary to understand the results in this thesis and not a review of the entire field but a short assessment of prior work to put these new results in context.

### 1.1 Fundamental science

The temperature of an ensemble of molecules is defined by the distribution of the molecules in molecular energy states including translational, rotational and vibrational degrees of freedom. If an ensemble consists of molecules that are all in the same energy state then the ensemble has zero temperature; the broader the range of energy states that are occupied, the higher the temperature of the ensemble. To cool a molecular ensemble, the width of a distribution of occupied molecular energy states must be narrowed.

The translational temperature of an ensemble of molecules can also be represented as a matter wave with a de Broglie wavelength defined by

$$\lambda = \left( \frac{2\pi\hbar^2}{mk_{\text{b}}T} \right)^{\frac{1}{2}}, \quad (1.1.1)$$

where  $\hbar$  is the reduced Planck constant,  $m$  is the mass of an individual molecule,  $k_{\text{b}}$  is the Boltzmann constant and  $T$  is the translational temperature. At room temperature this wavelength is vanishingly small and molecules can be considered to be individual particles. When an ensemble



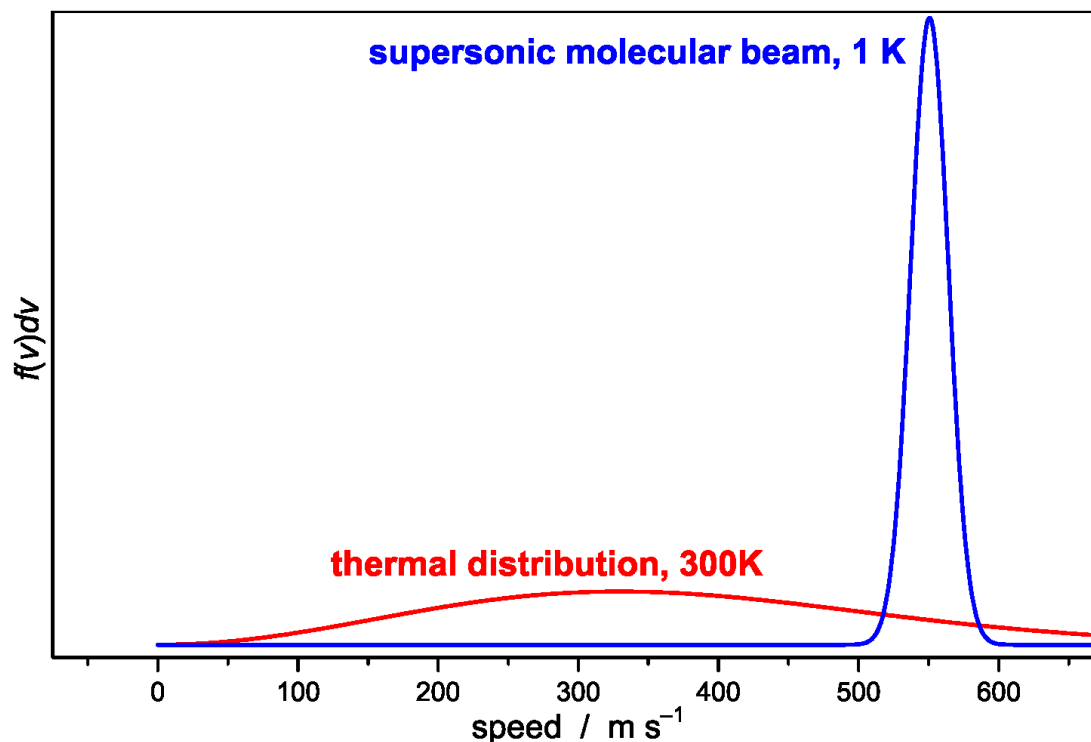


Figure 1.1: Comparison of the Maxwell-Boltzmann, speed distribution of a thermal ensemble of molecules within a nozzle before and in a molecular beam after a supersonic expansion. The narrow speed distribution of the molecular beam shows cooling during the supersonic expansion.

of molecules temperature is in the 1 K to 1 mK range, the de Broglie wavelength generally becomes comparable to the molecules classical size and the molecules are said to be “cold”. When an ensemble of molecules temperature is below 1 mK, the de Broglie wavelength becomes larger than the classical separation distance between the molecules, the molecules will exhibit macroscopic quantum phenomena and are described as being “ultracold”.<sup>6</sup>

### 1.1.1 Molecular beams and supersonic expansion

To study cold or clustered chemical species, the supersonic expansion is an invaluable technique. By simply expanding a pressurised gas sample through an orifice (0.5 - 2 mm diameter) into a low pressure region, typically below  $10^{-4}$  mbar, a room temperature gas is cooled to only a few Kelvin whilst being accelerated to several hundred m/s.<sup>7</sup>

Supersonic expansion is achieved when the average distance between gas particles collisions is much less than the orifice diameter. Under these conditions the gas expands adiabatically and its initial molar enthalpy is converted into kinetic energy in the molecular beam direction. The initial and supersonic temperatures and pressures of the expanding gas can be linked by,

$$\frac{T}{T_0} = \frac{P}{P_0}^{\frac{\gamma-1}{\gamma}}, \quad (1.1.2)$$

in which  $T$  and  $P$  are temperature and pressure, respectively, and  $\gamma$  is the ratio of heat capacities,  $c_p/c_V$ , for the expanding gas. It is clear that the large decrease in pressure in the expansion will be accompanied by a proportional decrease in temperature. The terminal velocity,  $v_t$ , of the supersonic source can be found by,

$$v_t = \sqrt{\frac{2k_b(T_0 - T)}{m} \frac{\gamma}{\gamma - 1}}, \quad (1.1.3)$$

in which  $m$  is the molecular mass of the gas species and  $T$  the translational temperature of the beam. It should be noted that this formula is derived from thermodynamic considerations based on continuous molecular beams, it is normally a good guide for the measured speed of a pulsed molecular beam.

The cooling can be understood on a molecular level by considering the collision frequency. Before the expansion, the gas undergoes collisions in all directions at a GHz frequency creating thermal equilibrium with the gas container. Once the nozzle orifice is opened, molecules near the orifice will move into the vacuum and their collision frequency will drop. Molecules that have entered the vacuum will only experience collisions from faster molecules behind them and slower ones in front of them, this results in a narrowing of the translational velocity distribution. It should be noted that this cooling effect relies on a high gas density in the expansion region such that collisions between molecules happen far more frequently than collisions with the walls of the orifice so that a thermal equilibrium with the gas container is not maintained.

The cooling process is most useful when a poly-atomic molecule of interest is mixed with a much larger quantity of “carrier gas”, usually a noble gas. This not only allows for translational cooling but also for vibrational and rotational cooling of the poly-atomic molecule by collisions with the cold carrier gas in the expansion region. Typically more collisions are needed to cool rotational degrees of freedom than translational and more still to cool vibrational degrees of freedom.

Although the supersonic expansion provides excellent cooling, the cooled molecules do not naturally form anything close to a collimated beam. To achieve this, the supersonic expansion is aimed at an additional hole called a skimmer. This skimmer will only allow molecules to pass through that travel in a straight line from the nozzle orifice to the skimmer, thus creating a molecular beam.

Work on continuous flow molecular beams with a constantly open orifice requires high pumping speed and is wasteful when using pulsed lasers. The molecular beam can be made into a pulsed source of cold directed molecules simply by using a solenoid to move a poppet which can open and close the orifice. There are a number of different designs for mechanisms that open and close the orifice rapidly, in less than 1 ms, but all fundamentally work by using a current pulse to somehow force a poppet to briefly open the orifice and allow gas to enter the vacuum region.<sup>8</sup>

### 1.1.2 Laser spectroscopy

Laser spectroscopy is used to study a molecule's physical properties such as its rotation, vibration and electronic configurations, as well as its clustering with other molecules. A light source can be used to measure the relative energies between a molecule's quantum states as well to prepare a molecule in a desired excited state. The laser light sources used in this thesis are collimated, high-intensity, coherent and narrow-band and can generally resolve the rotational structure of two or three atom molecules.

By intersecting laser light with molecular or atomic beams and scanning the laser light's wavelength, the molecules in the beam can be promoted from lower energy states to higher states when the energy gap between the states matches the energy of the laser. Once the molecules have absorbed a photon or multiple photons and are in an excited state, the molecules can undergo a number of processes. The processes that are studied in this thesis are fluorescence that causes emission of a second photon of equal or lesser energy than the one it absorbed, loss of an electron from its electronic structure creating an ion or the breaking of a chemical bond leading to dissociation.

### 1.1.3 Trapping and guiding fields

If a molecule possesses a magnetic dipole moment then it will experience a force inside a magnetic field gradient. Inside a magnetic field potential, such as a magnetic trapping field, the force experienced by an atom or molecule is given by

$$F = g_J \mu_B m_J \Delta B, \quad (1.1.4)$$

in which  $F$  is the force experienced in a given field gradient,  $\Delta B$ , by an atom or molecule with a given Zeeman-sub state,  $m_J$ , Lande  $g$ -factor  $g_J$  and Bohr magneton  $\mu_B$ . The magnetic moment of a molecule is caused by contributions from the electronic and spin angular momenta in the molecule.

When in an electric field potential, such as an ion optics stack, the force given to a charged particle is given by

$$F = qE, \quad (1.1.5)$$

in which  $F$  is the force experienced in a given field,  $E$ , by a particle with an electric charge,  $q$ . Both magnetic and electric fields are used throughout this thesis to provide molecular traps and ion optics to direct ions from experimental regions to detectors.

## 1.2 Relevant prior work

Following on from the successful field of cold and ultracold atoms, the field of cold and ultracold molecules has had some notable successes: quantum-state control of ultracold chemical reactions

of KRb;<sup>9</sup> the first quantum simulation of many-body dynamics in spin lattices of KRb;<sup>8</sup> the lowest upper limit of the dipole moment of the electron;<sup>10,11</sup> molecule laser cooling;<sup>12,13</sup> magneto-optical trapping<sup>14</sup> and opto-electric cooling.<sup>15</sup>

Some experiments involved the indirect formation of ultracold molecules via the coherent association of ultracold atoms.<sup>16,17</sup> Such techniques are currently limited to combinations of atoms that can be laser cooled. Techniques that cool molecules directly strive to diversify the range of species that can be cooled to expand the field into more chemically relevant domains. The molecular-synchrotron experiments<sup>18</sup> of Heiner *et al.* and the more recent laser-cooling<sup>14</sup> and opto-electric-cooling<sup>15</sup> experiments have reached sample temperatures on the order of 0.5 mK. However, the sub-milliKelvin barrier into the ultracold regime has only recently been marginally breached. Further cooling techniques are required to cool molecules directly towards and below 1  $\mu$ K. A promising method is to use a refrigerant gas that can be cooled to ultracold temperatures and subsequently sympathetically reduce the temperature of molecules via elastic collisions.<sup>19</sup>

The key experimental step in sympathetic cooling is the trapping of the cold molecules such that they can be merged with the ultracold refrigerant gas. Parazzoli *et al.* attempted to sympathetically cool ND<sub>3</sub> with Rb. In this experiment, the Stark decelerated ND<sub>3</sub> was trapped electrostatically and the Rb was trapped magnetically.<sup>20</sup> Both atoms and molecules were not in their absolute ground states and sympathetic cooling was not possible due to fast inelastic processes that lead to trap loss. Apart from some exemptions that have been identified by theory, NH–Mg,<sup>21</sup> NH–Li<sup>22</sup> and CaH–Li/Mg,<sup>23,24</sup> trapped molecules should be in their absolute ground state, such that trap-ejecting inelastic collisions are energetically forbidden.

Trapping of ground-state ND<sub>3</sub> at 1 mK has been demonstrated in AC electrostatic traps,<sup>25</sup> but the translational energy due to molecule micromotion precludes sympathetic cooling.<sup>19</sup> This would not be an issue for optical-dipole traps and optical lattices, but such traps are shallow and have small volumes. Dipole traps, formed from standing waves of microwaves in a Fabry–Perot cavity, potentially have depths over 100 mK<sup>26</sup> and are a more promising starting point for sympathetic cooling. The photostop method is capable of loading traps by producing the cold molecules directly inside the trap. This has been demonstrated with atomic bromine<sup>27</sup> in a permanent magnetic trap.<sup>28</sup> Following on from the work on the production of cold NO via photostop,<sup>29</sup> this thesis demonstrates that cold SH radicals can be magnetically trapped following the photodissociation of H<sub>2</sub>S in a molecular-beam and that triplet atomic oxygen can be trapped following the photodissociation of NO<sub>2</sub>.

## Chapter 2

# Magnetic trapping of SH radicals

Trapped, neutral molecules and radicals are not easily produced or detected. Unlike ions, molecules have a comparatively weak interaction with a field. Thus to trap a neutral, polar molecule it must have sufficiently low kinetic energy to be held by the low potential-energy barrier of the trap. Translationally slow molecules can satisfy this condition but are also challenging to produce. Photostop has previously shown<sup>30-33</sup> its ability to produce these translationally cold and slow molecules. Here a discussion of the static trapping of photostopped SH radicals is presented. This chapter details the design of the photostop experiment and discusses the successful trapping<sup>34</sup> and simulation of the SH radicals.

### 2.1 The photostop technique

Photostop requires only one laser for generation of trapped molecules, the dissociation laser, and another for their detection, in this case by resonance-enhanced multiphoton ionisation time-of-flight mass spectrometry (REMPI-TOF-MS or just REMPI), as well as a molecular beam source.<sup>7</sup> The technique should be classed separately to a threshold dissociation<sup>35</sup> of a stationary cold molecule as it has different requirements and challenges. The technique requires that the molecular beam velocity,  $v_{\text{beam}}$ , and the recoil velocity of the desired photofragment sum to zero so that photofragments are created at rest as in fig. (2.1). This leads to the photostop condition,

$$v_{\text{beam}} = \sqrt{\frac{2m_{\text{acc}}(h\nu - D_0 - E_{\text{int}})}{m_{\text{stop}}m_{\text{pre}}}}, \quad (2.1.1)$$

in which  $m_{\text{acc}}$ ,  $m_{\text{stop}}$  and  $m_{\text{pre}}$  are the masses of the photoaccelerated, photostopped and precursor molecules, respectively,  $h\nu$  is the photon energy of the dissociation light,  $D_0$  is the threshold dissociation energy and  $E_{\text{int}}$  is the sum of the internal energies of both photofragments including any rotational, vibrational or electronic energy. In this case,  $E_{\text{int}}$  is effectively zero as the hydrogen atom is produced in its ground state and the only SH species of interest is the rovibrational ground state.

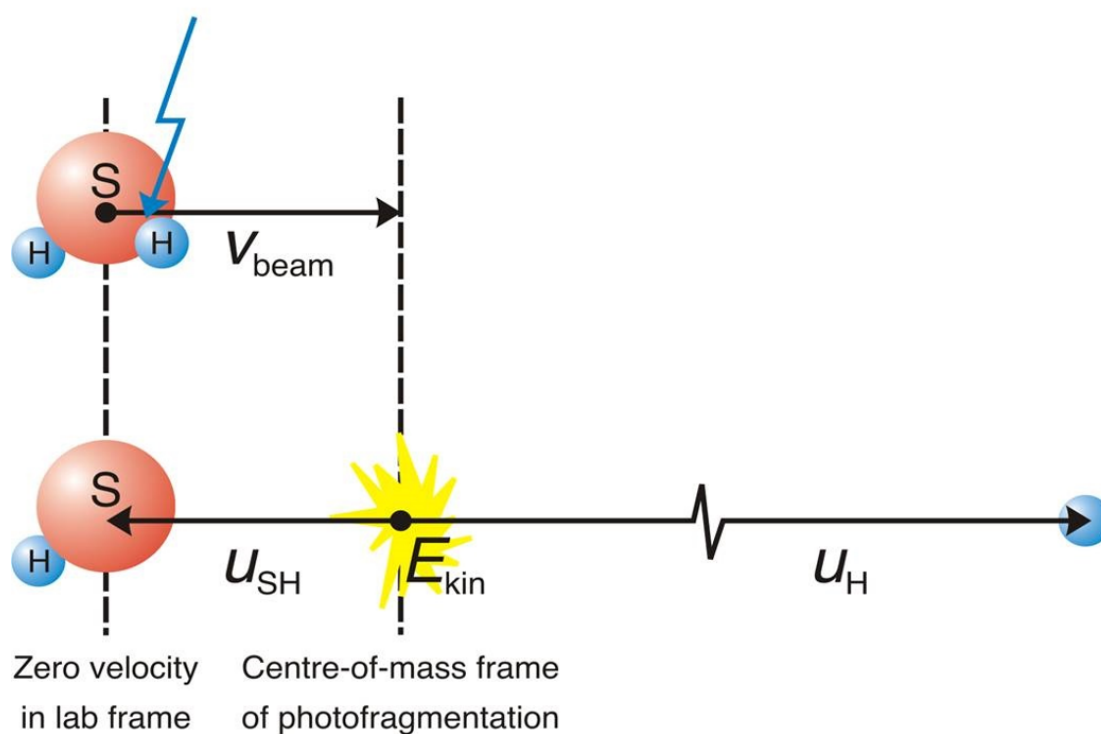


Figure 2.1: Schematic of photostop of SH from  $\text{H}_2\text{S}$ .

Photostop is applicable to any precursor molecule with a dissociative absorption spectrum accessible via available laser sources and a photostop condition for the desired fragment, according to eqn. (2.1.1), that is achievable in a molecular beam source. Ideally, the state distribution of the photofragments should be biased towards the desired quantum state of the photostopped fragment.

## 2.2 Introduction

Photostop is an elegantly simple and relatively cheap technique. It can be performed in a small space with little access requirements and so it is suitable for the combination with linear decelerators, buffer gas cooled molecular beams and a range of traps including magnetic, electric and Fabry-Perot microwave dipole traps.<sup>36</sup> Photostop removes all of the kinetic energy of some molecules in a beam in an instant and does not require a trap to be opened and closed to accept new cold molecules, this potentially allows for density accumulation although this is yet to be observed. Because photostop relies on a high density molecular beam source to enter the trapping region it is also susceptible to collisional trap losses and often problematic signal to noise ratios from a supersonic molecular beam and its effusive tail. Photostop allows access to cold molecular and atomic species that lack obvious laser cooling routes.

Photostop has, at the time of writing, been used to produce stopped Br, O, NO, SH and SD to the author's knowledge.<sup>30,32,33</sup> Theoretical studies have also been conducted on ICl and ICN as precursors.<sup>37</sup> However only Br atoms have previously been produced in a static magnetic trap

and had their trapped lifetime measured.<sup>32</sup>

SH radicals have now been shown to persist in the detection volume of a magnetic trap for up to 80 ms at an estimated maximum density of  $2.4 \times 10^5 \text{ cm}^{-3}$ . The  $1/e$  lifetime of the trapped radicals was measured to be  $40 \pm 10$  ms, without a magnetic trap the SH radicals could not be detected 5 ms after their creation, confirming the role of the trap.

## 2.3 Experimental

A detailed description of the design and development of the experimental apparatus used in this chapter is given in the thesis<sup>33</sup> of N. Warner. This chapter follows on from some of the work presented in that thesis.

### Molecular beam source

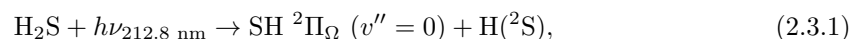
The gas mixture was supersonically expanded into vacuum by a pulsed solenoid valve (Parker, General valve Series 9, 0.5 mm orifice, 160  $\mu\text{s}$  opening driver current duration.) The supersonic expansion was skimmed (Beam Dynamics, Model 40.5, 2 mm orifice) to form a molecular beam with a 4 Bar backing gas pressure. The solenoid valve sat 115 mm from the magnetic trap centre and fired at a 5 Hz repetition rate. A typical beam pulse had a 125  $\mu\text{s}$  full-width half-maximum at the intersection with the dissociation laser. The solenoid valve was mounted inside the high-vacuum chamber. The beam could be adjusted whilst under vacuum through alteration of the sealing spring tension in the valve, as well as, to some extent, the distance from the valve to the experiment.

The skimmed molecular beam passed through a 3 mm hole on a cryostat before entering the detection region of the experiment as in fig. (2.8). The 3 mm hole was present to limit background gas inside the detection region and to have little to no impact on the molecular beam profile itself due to simple geometry. Although the experiment does not have a velocity-map-imaging setup, the beam speed was found by measuring the temporal profile using REMPI in the trapping region and then using an amplified fast ionisation gauge (FIG) at a known distance after the trap. The photostop condition from equation. (2.1.1) was met for  $v_{\text{beam}} = 575 \text{ m/s}$  which was achieved through an  $\text{H}_2\text{S}$  to Kr mixing ratio of 3:1.

### Molecular dynamics and photostop losses

The  $\text{H}_2\text{S}$  molecules came from a thermal room temperature source; upon pulsed supersonic expansion in a Kr carrier gas the rotational, vibrational and translational temperatures dropped significantly at the expense of a large laboratory frame velocity.<sup>7</sup>

The molecules in the beam were then dissociated according to



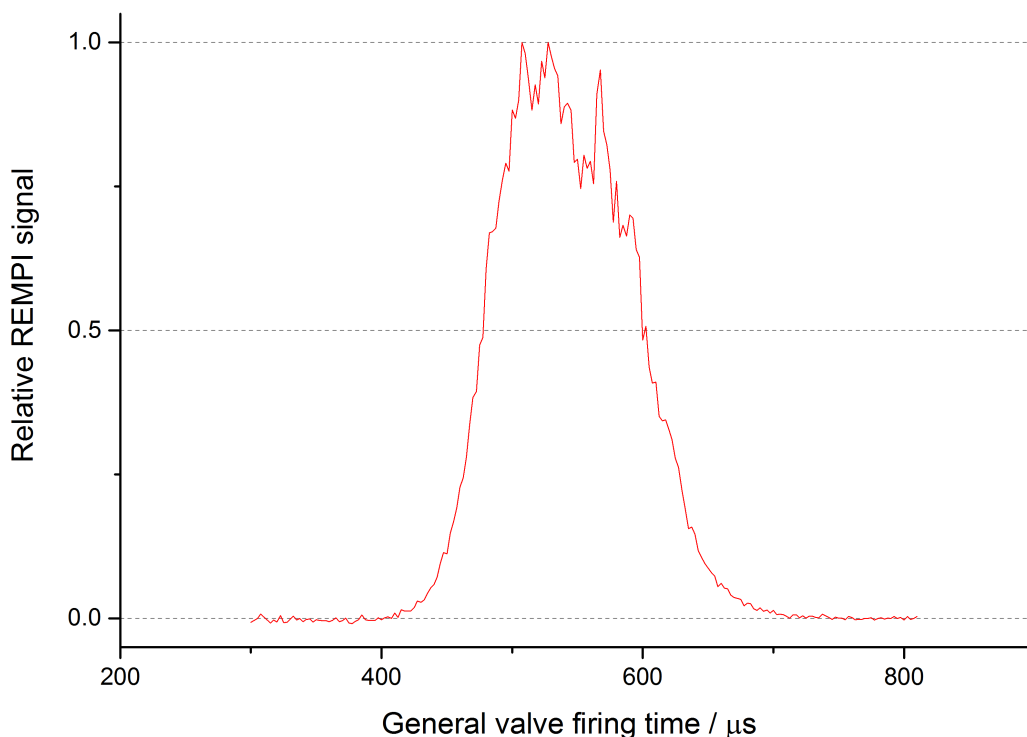


Figure 2.2: Typical molecular beam pulse taken inside the trap volume using REMPI-TOF-MS of SH with the dissociation laser firing 100 ns before the probe, solenoid valve with 4 Bar 75 % H<sub>2</sub>S, 25 % Kr backing gas composition.

inside the magnetic trap, the dissociation results in a non-statistical rotational product distribution peaking at  $J_{\text{peak}} = 3/2$  according to Weiner *et al.*<sup>38</sup> The low mass of the H atom co-product meant that there was only a small amount of torque applied to the rotation of SH from the release of the bond angle of H<sub>2</sub>S. Weiner *et al.* also found an absence of any  $\Lambda$ -doubling parity preference in the SH radical product. The equality in product-state parity suggests that the dissociation proceeds via a non-direct method and has an excited state lifetime able to support a few molecular vibrations and rotations thus scrambling any dissociation preference on  $\Lambda$ -doubling parity. It was also observed externally that the product rotational distributions were relatively independent of dissociation wavelength and vibrational temperature of H<sub>2</sub>S. The dissociation occurred through predissociation in  $10^{-12}$  to  $10^{-15}$  seconds via the perpendicular transition from the  $^1A_1$  ground to the  $^1B_1$  excited state, followed by predissociation through the  $^1A_2$  state leading to SH( $^2\Pi_{\Omega}$ ) and H( $^2S$ ) photofragments.<sup>38</sup>

These molecular dynamics make H<sub>2</sub>S suitable for photostop. The combination of a dense beam of H<sub>2</sub>S from the supersonic expansion at the correct velocity for photostop and a peak in rotational distribution of SH at the lowest energy state meant that more ground-state cold and slow SH was created.

There are still significant losses involved in photostopping a molecule. 60 % of the SH fragments



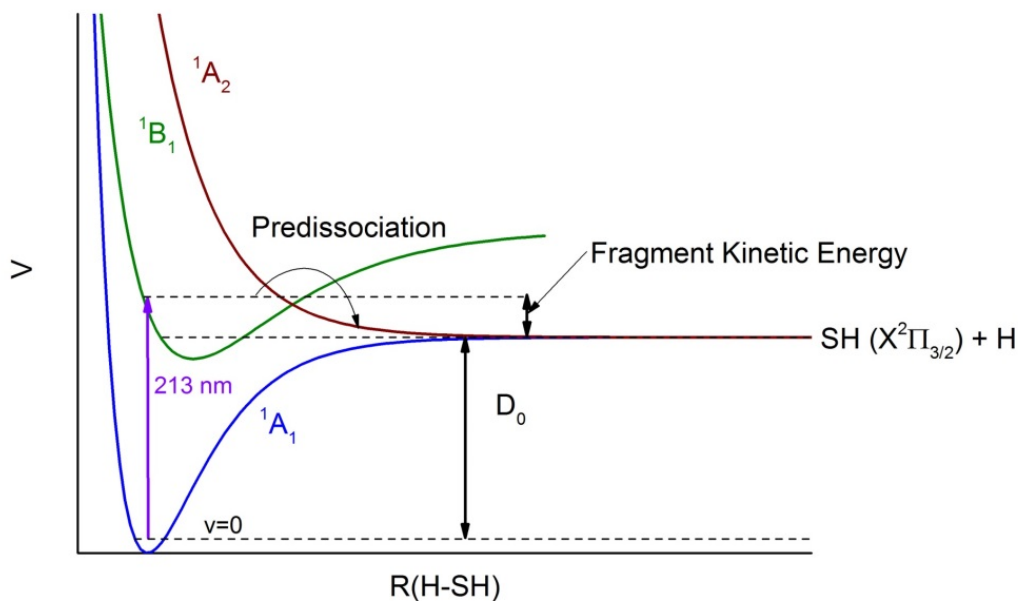


Figure 2.3: Annotated potential energy surfaces showing the accepted dissociation route for the  $\text{H}_2\text{S}$  molecule into the SH ground state.

are produced in the trappable spin-orbit ground state ( $^2\Pi_{3/2}$ ), almost all (>95 %) in the vibrational ground state ( $v = 0$ ) and about 8 % in the lowest  $J = 3/2$  rotational state. Also, only the  $m_J = 3/2$  and  $1/2$  Zeeman low-field-seeking sub-states are effectively trapped by the static magnetic trap, by equation. (1.1.4), in which the force  $F$  experienced by the trapped species, is proportional to a combination of the Lande  $g$ -factor, the Bohr magneton, the Zeeman substate and the magnetic field gradient. This results in further losses from radicals in the high-field-seeking Zeeman states.

The other large loss that results from photostop is that only a fraction of the dissociated molecules will exist on the right part of the Newton sphere to be photostopped and not photoaccelerated or diverted. The linear polarisation of the dissociation laser was arranged perpendicular to the molecular beam. Since this polarisation defines a direction in the laboratory frame, it can also define a directional preference in photodissociation if the process is anisotropic. The relationship between the lasers electric field vector and the dissociation products recoil velocity vector can be described by,

$$\frac{d\sigma}{d\Omega}(\theta) = \frac{\sigma}{4\pi}(1 + P_2\beta(\cos(\theta))), \quad (2.3.2)$$

in which  $P_2$  is the second-order Legendre polynomial,  $\theta$  the angle between electric field and recoil vectors,  $\frac{d\sigma}{d\Omega}$  the solid angle dependent photodissociation differential cross-section and  $\sigma$  the dissociation cross-section across the full solid angle.  $\beta$  is the anisotropy parameter which in this case has a value approaching  $-1$  that gives a torus shaped recoil velocity angular distribution that contains the molecular beam velocity vector. The proportion of molecules that will be photostopped and

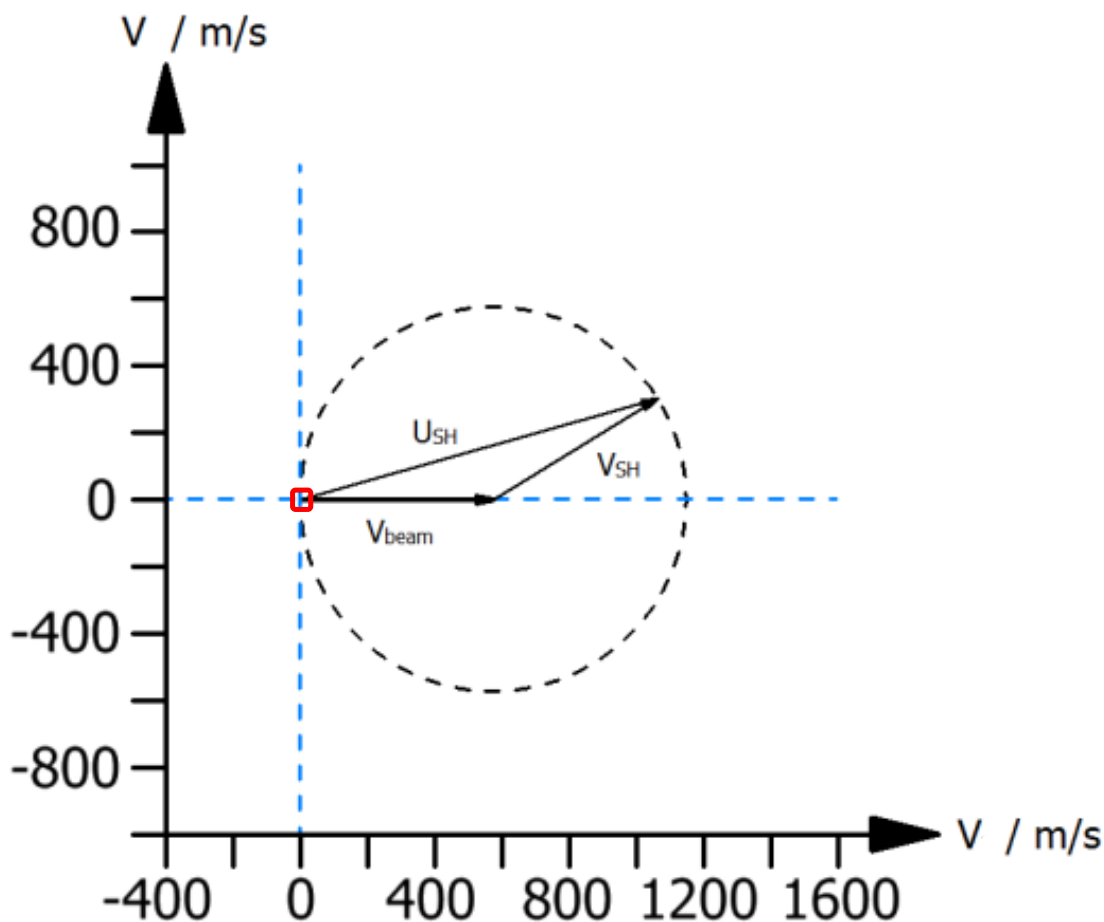


Figure 2.4: Newton sphere of SH after dissociation by a 212.8 nm laser. When  $v_{\text{SH}} = -v_{\text{beam}}$  the SH molecules that are dissociated at the correct angle are created with near-zero velocity in the laboratory frame inside a magnetic trap and so are cold and trapped. There is a small range of non-zero velocities that the trap will accept up to 13 m/s indicated by a red square that is not to scale.

retained in the trap is proportional to the squared reciprocal of the beam speed that is cancelled and also scales with the velocity distribution of the source, a narrower distribution reduces losses.

### Laser systems

Photostop of SH required two laser systems. The dissociation laser used was the 5<sup>th</sup> harmonic of the 1064 nm Nd:YAG solid-state laser (Continuum, Surelite I-10, 10 Hz repetition rate) at 212.8 nm. The 212.8 nm light was created by doubling inside a non-centrosymmetric crystal to give 532 nm, doubling that to give 266 nm and then using the 1<sup>st</sup> and 4<sup>th</sup> harmonics to make the 5<sup>th</sup> in another BBO crystal by sum-frequency-mixing. The fundamental lasers beam profile was pseudo-Gaussian and this pseudo-Gaussian profile was to some extent maintained by the three doubling crystals although the quality of the profile decreased with each non-linear process. The 212.8 nm light was separated from the remaining 266 nm and directed by four dichroic mirrors and a prism as shown

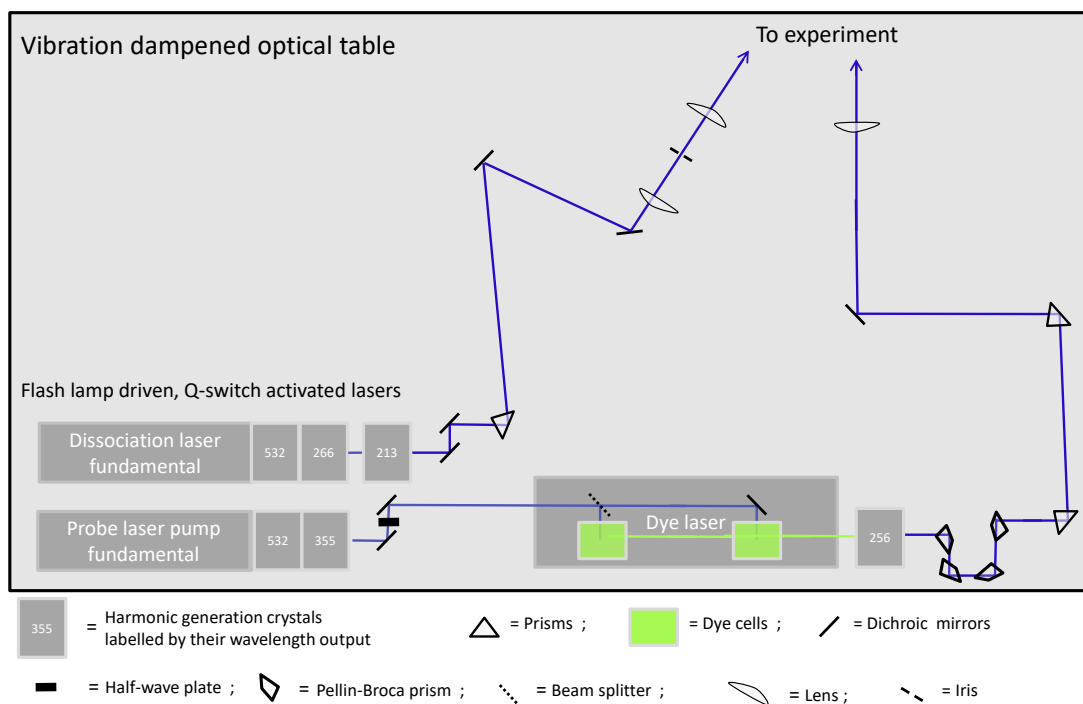


Figure 2.5: Birds-eye schematic view (not to scale) of the optical setup for the SH photostop experiment, the key is shown in figure. The Dye laser components have been simplified. The focusing lens for the probe laser had a focal length of 500 mm.

in fig. (2.5). A 2:1 telescope (two  $\text{CaF}_2$  lenses  $f = 200$  and  $100$  mm) then narrowed and collimated the beam such that a maximum amount of photons were allowed to interact with the  $\text{H}_2\text{S}$  without damaging the  $\text{CaF}_2$  windows on the experiment that made the vacuum seal. The dissociation laser profile inside the magnetic trap had a vertical  $e^{-2}$  radius of 1.2 mm and a horizontal of 1.7 mm.

The probe laser was at 255.75 nm with a 5 ns pulse width, the spectroscopic details will be discussed later. It was created by doubling the output of a 355 nm pumped and internally amplified dye laser (Sirah Cobra-Stretch, 0.2 g/L Coumarin-307 (503) in methanol.) The pump laser was a frequency tripled Nd:YAG solid-state laser (Continuum, Surelite i-10, 10 Hz repetition rate) that was wavelength separated by two dichroic mirrors. The probe laser was separated and steered by a series of two prisms and four Pellin-Broca prisms after the doubling crystal and finally focused into the trap volume as a high photon flux was needed for the multiphoton ionisation process, the focal point of the laser had a diameter of approximately 0.2 mm (not measured).

The light intensities of both the dissociation and probe lasers had their power monitored on a shot-to-shot basis by pyroelectric gauges (Sensor-und Lasertechnik, PEM 21) to be 1.5 mJ/pulse and 1 mJ/pulse respectively after the experiment, thus the actual power in the experiment was slightly greater than that detected due to losses in the final  $\text{CaF}_2$  windows. The power of the

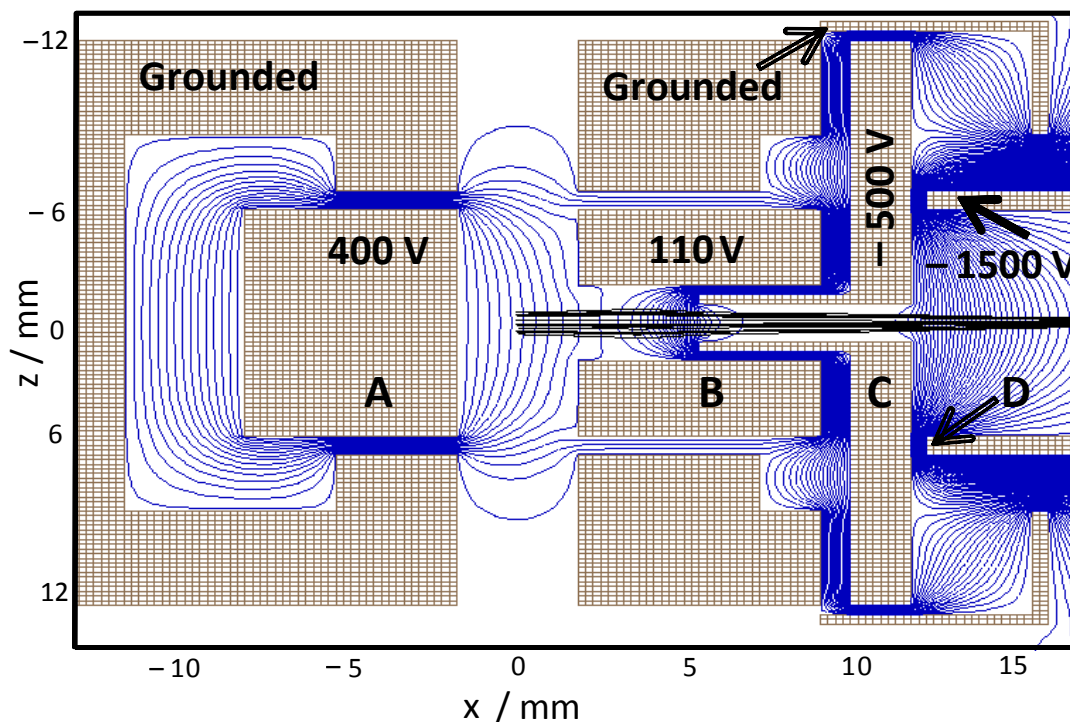


Figure 2.6: SIMION 8.0 simulation showing a cut through of the cylindrically symmetric (in the  $x$  plane of the figure) electrodes for ion extraction from the trap. (A) Ring magnet with copper insert, (B) opposing ring magnet, (C) extractor, (D) time-of-flight tube. Blue lines show the electrostatic potential contours and black lines show simulated SH ion trajectories from within the probe volume.

dissociation laser was deliberately dropped, through a non-optimal Q-switch delay. This avoided damage to the  $\text{CaF}_2$  telescope and windows as well as preventing the saturation of the  $\text{H}_2\text{S}$  dissociation.

### Trapping and detection scheme

The magnetic trap, as shown in fig. (2.7), was formed by two NdFeB ring magnets (OD 12 mm, spacing 4 mm, height 7 mm, bore 4 mm) in anti-Helmholtz configuration with a residual magnetisation of 1.46 T, the trapping force occurred according to equation (1.1.4). The resulting trap had a volume of  $0.1 \text{ cm}^3$  and a depth of 0.41 T.  $\text{SH}(^2\Pi_{3/2}, v = 0, J = 3/2)$  radicals in their  $m_J = +3/2$  low-field-seeking Zeeman sub-state possess the largest Zeeman shift which in this trap gave a depth of 330 mK and a capture velocity of 13 m/s. The magnets also formed part of the electrode setup for the REMPI-TOF-MS detection scheme as detailed in fig. (2.6). When a magnetic field was not required, the magnets were replaced with copper-metal blocks of identical shape to form the ion optics and ensure the same experimental geometry.

Some SH radicals were first photostopped by the dissociation laser and then after a delay

between zero and 80 ms the probe laser was used to ionise them through a resonant Rydberg state detailed in 2.3.2. Once the ions had been created they were accelerated by the ion optics into the micro channel plate (MCP) (Hamamatsu, F12334-11) array after a time-of-flight tube. After 3.5  $\mu\text{s}$  the SH ions were detected by the MCP which was biased between  $-1200$  and  $-1600$  V depending on signal intensity. The more traditional mass spectroscopic setup shown in fig. (2.6) was used to collect the ions and gave a probing volume of  $1.5 \times 10^{-3} \text{ cm}^3$ . This accounted for approximately 2 % of the trap volume and 9 % of the photodissociation volume.

The “hoover” mode was also tested and in some circumstances showed greater ion collection efficiency. The hoover mode worked with just the extraction plate (C) and time-of-flight tube (D) charged. This gave a much more gradual electric potential in the trapping region, the probe volume was increased along the probe laser axis at the expense of good mass resolution. In the end the lack of mass resolution proved too problematic as  $\text{SH}^+$  signal had to be distinguished from a small but relevant amount of  $\text{S}^+$  signal and the hoover mode could not do this.

The MCP signal was digitised by an oscilloscope (Lecroy, Waverunner 650Zi) at 5 GS/s and then transmitted by an Ethernet connection to the main computer for analysis and recording using a custom suite of Labview programs. The MCP signal was analysed over a time interval of 500 ns and contained the SH mass peak and 400 ns of noise for baseline subtraction. The MCP signal was sampled every 200 ps to give good resolution of single ion events. The laser powers for each shot were also recorded; these were detected by pyroelectric detectors and digitised by a card (National instruments, 200 MS/s) in the main computer. As an experimental cycle could take up to 80 ms it was run at 5 Hz so that there was always enough time for serial data transfer and processing before the next experiment started. It was possible to run the cycle at 10 Hz but only 95 % of the data was recorded at long delay times due to the limited data transfer speeds, thus it was decided to work at 5 Hz to avoid this problem. The experiment was temporally controlled by a single pulse-generator (Quantum Composers, 9000 series) that was programmed through a Labview interface.

### 2.3.1 Pumping and beam speed stability improvements

The experimental apparatus was evacuated to ultra-high vacuum (UHV) by two turbo molecular pumps (the small turbo has a pumping speed of 250 l/s and the large a pumping speed of 1260 l/s), which were backed by a single rotary vane pump, and a modified two-stage cryostat (Leybold-Heraeus, RPK1200) acting as a pump. The cryopump operated by cooling a copper cryostat inner stage to an unmeasured but estimated 20 K and an outer radiation shield to 75 K. The magnetic trap sat on the cryostat inner stage with laser and molecular beam access making the magnetic trap itself a cryopump. Many surfaces of the radiation shield were coated in activated charcoal to maximise the capacity of the outer stage thus reducing background gas in the trapping region. There was a significant amount of background gas entering the trap from the unskimmed molecular beam residue that was not pumped quickly enough. The background gas was pumped

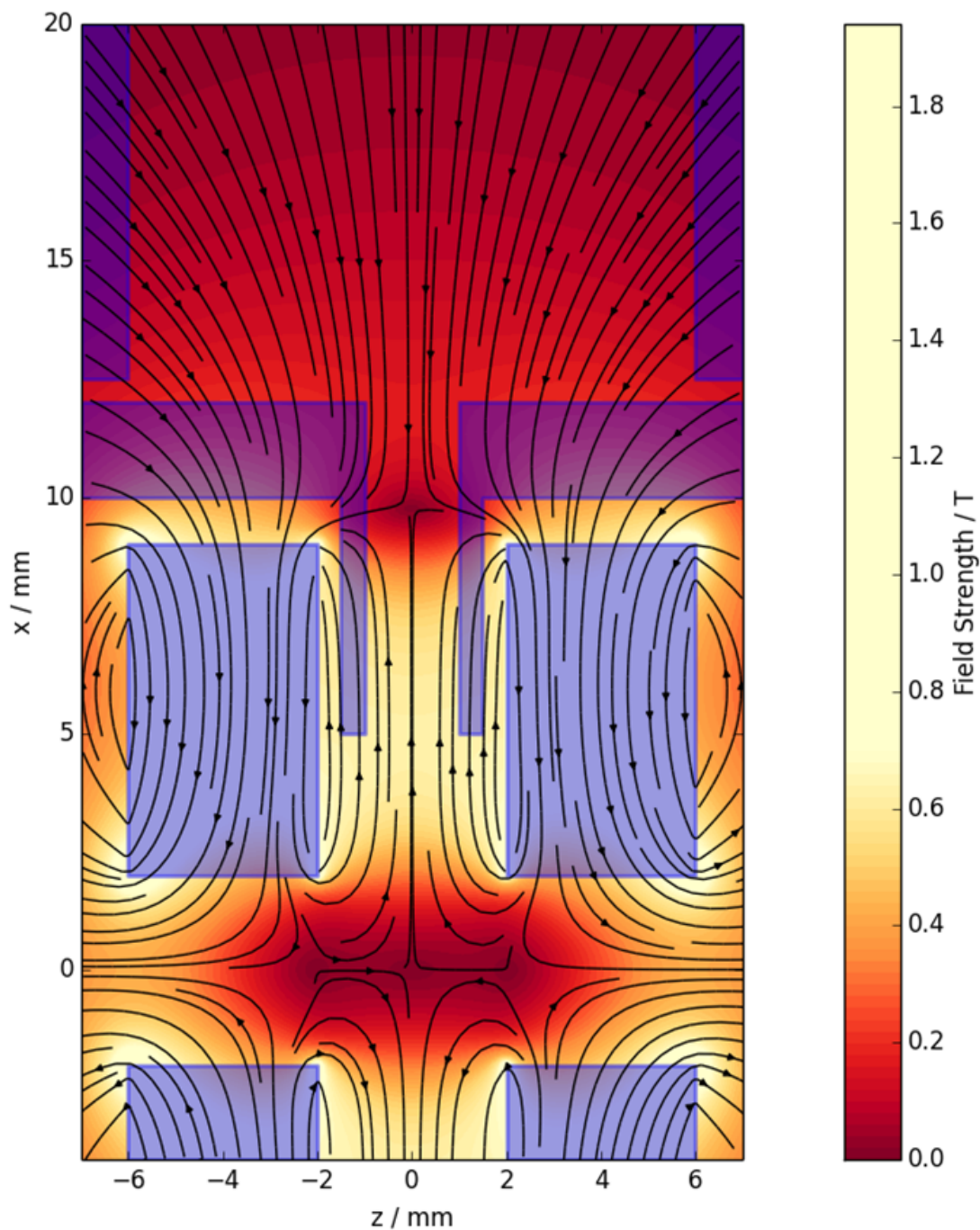


Figure 2.7: 2D cut through of the permanent magnetic trap formed by two NdFeB ring magnets in anti-Helmholtz configuration. The cylindrical symmetry axis is the  $x$  (vertical) axis in the figure. The field strength is indicated by the colour gradient. The direction of the B-field is given by the black arrows. Note that both magnets are identical but the bottom magnet is cut by the figure. The ion extraction and TOF tubes are indicated in the top of the figure.

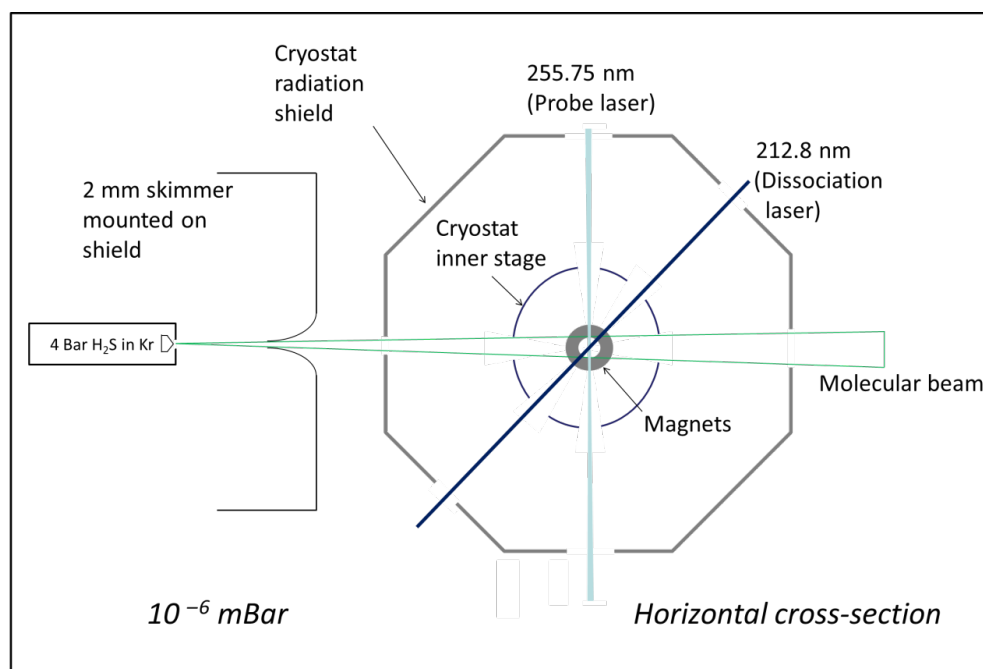


Figure 2.8: Schematic drawing (not to scale) of the SH photostop experimental apparatus, ion extraction occurred out of the plane of the page.

away with a longer  $1/e$  lifetime than the trapped molecules and so this gas had to be kept away from the trapping region to prevent trap loss collisions. It should be noted that coating with activated charcoal on outside surfaces of the radiation shield would result in a higher temperature as the shield more effectively absorbs blackbody radiation thus increasing the cryopumps temperature whilst raising its capacity. The chamber base pressure, with the cryopump at its lowest temperature, was measured by a Bayard-Alpert gauge to be  $10^{-9}$  mbar and  $10^{-6}$  mbar under experimental conditions.

The cryopump was also included in the design of this experiment to limit trap losses, the cryopump operated as a radiation shield in an onion like experiment design. This significantly reduced the amount of blackbody radiation that penetrated into the trapping volume including in the microwave region which could cause problematic changes in SH rotational state. The radiation that did get to the trapping volume was in general of lower energy and much lower intensity and so fewer transitions of the trapped molecules to un-trapped states could be excited and thus the trap lifetime was extended if it was not limited by background gas collisions.<sup>39</sup>

The experiment was further improved by directing the molecular beam's unwanted gas load away from the trap volume; this was done by the introduction of a shield partially separating the "source chamber" from the cryostat in the detection chamber. The skimmer (Beam Dynamics, Model 40.5, 2 mm orifice) was mounted on this shield; this reduced the intensity of the molecular beam in the trap but had a greater effect on the background gas. The "source chamber" was also pumped separately by one of the turbo molecular pumps. Baffles coated in activated charcoal were

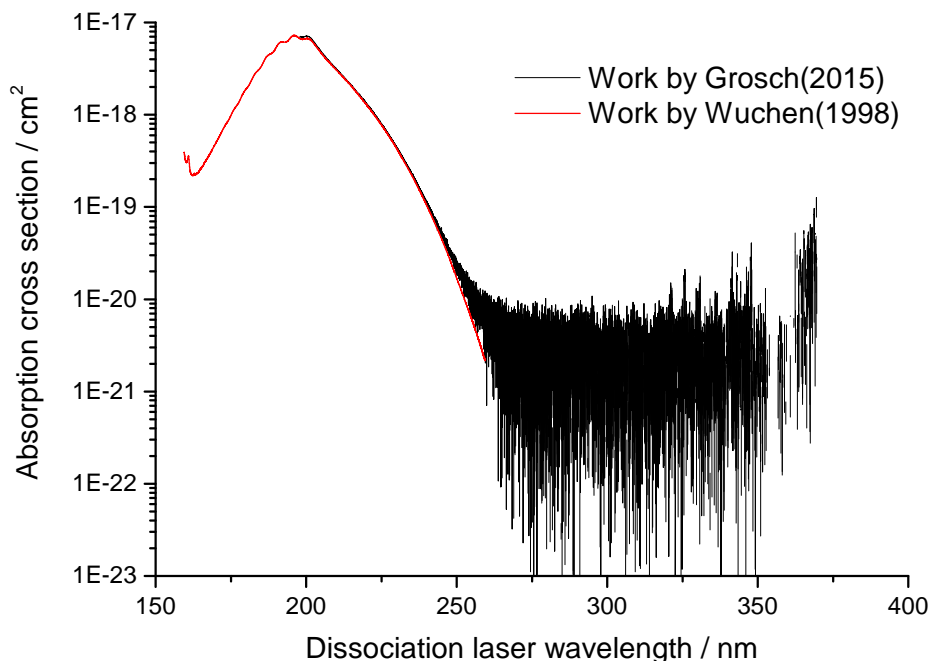


Figure 2.9: Absorption spectra of  $\text{H}_2\text{S}$  showing the absorption cross sections leading to dissociation at the probe and dissociation wavelengths, taken from the MPI-Mainz spectral.

also introduced on the cryo shields laser ports and any other access ports to the magnetic trap region were sealed where possible to reduce the chance of background gas making its way to the trap volume.

### 2.3.2 Alternative REMPI detection schemes

Previous work in the group<sup>33</sup> had been carried out on the detection process for the SH radical. Both laser-induced fluorescence (LIF) and cavity-enhanced laser-induced fluorescence (CELIF)<sup>40</sup> proved to have insufficient limits of detection to cover the seven orders of magnitude in sensitivity needed for this experiment and so are not discussed in this chapter.

REMPI-TOF-MS proved to have better sensitivity to the photostopped SH radicals. The main drawback of REMPI-TOF-MS was that the probe laser for a (2+1) process must be a high energy focused UV beam that was within the dissociation energy limit for the  $\text{H}_2\text{S}$  molecule. This meant that even without firing the dissociation laser, the probe laser could dissociate and ionise  $\text{H}_2\text{S}$  molecules on its own thus giving a one-colour signal. As can be seen from fig. (2.9), the absorption cross section at the dissociation wavelength was  $2.51 \times 10^{-18} \text{ cm}^2$ , although the cross section was over 200 (900)<sup>41</sup> times smaller at  $78201 \text{ cm}^{-1}$  (271.9 nm) the  $\text{H}_2\text{S}$  was still frequently dissociated by either probe laser wavelength.

The one-colour signal persisted into long time delays between lasers, due to background gas,



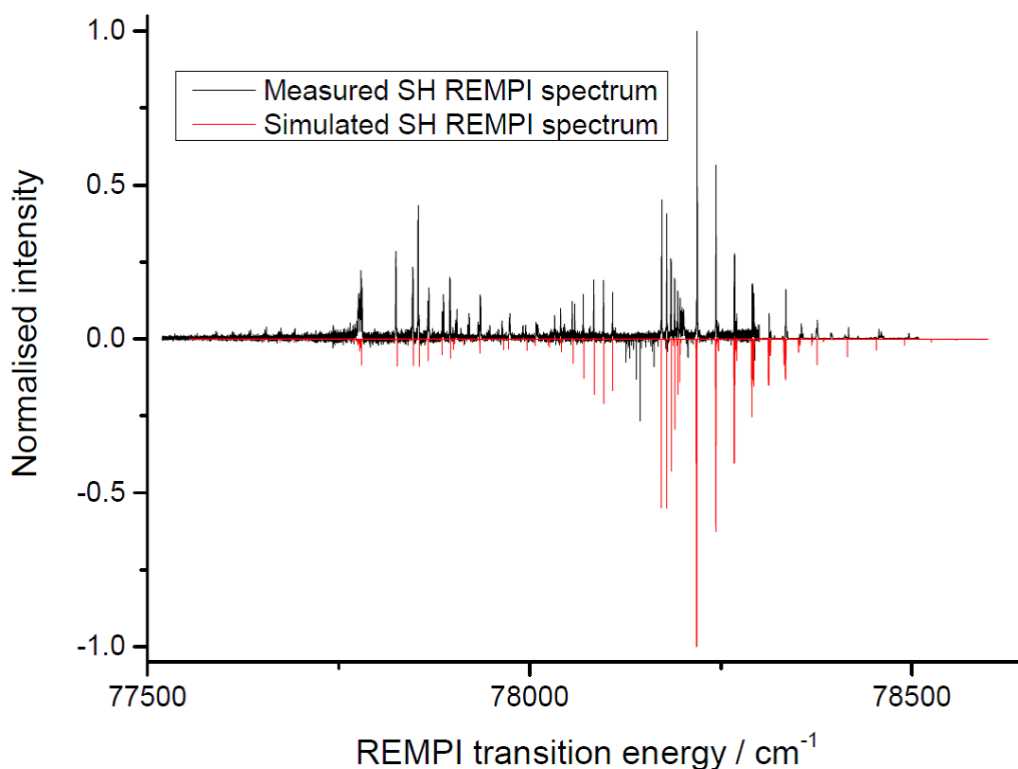


Figure 2.10: (2+1) REMPI excitation spectrum for the  $[a \ ^1\Delta] \ 3d\pi \ ^2\Phi \leftarrow\leftarrow X \ ^2\Pi_{3/2} \ (v = 0)$  transition in an SH radical. The spectrum is concurrent with the spectrum by Milan *et al.*<sup>42</sup> and has been successfully simulated using PGOPHER. Any negative signal is electronic noise. Note that the SH radicals are not in thermal equilibrium such that the peak intensities of the simulation do not match the experiment.

meaning that the true photostop signal was often small compared to the background. A  $78201 \text{ cm}^{-1}$  (2+1) REMPI scheme for the  $[a \ ^1\Delta] \ 3d\pi \ ^2\Phi \leftarrow\leftarrow X \ ^2\Pi_{3/2} \ (v = 0)$  Rydberg transition<sup>42</sup> is shown in fig. (2.10), this scheme was spectroscopically understood but relatively close in energy to the most efficient dissociation wavelength giving a significant background signal. Photostopped molecules were detected using the most intense  $S_1 \ (J = 3/2)$  line at  $78201 \text{ cm}^{-1}$ .

A second (2+1) REMPI scheme at  $271.9 \text{ nm}$  for the  $[a \ ^1\Delta] \ 4p\pi \ ^2\Phi \leftarrow\leftarrow X \ ^2\Pi_{3/2} \ (v = 0)$  Rydberg transition<sup>43</sup> is shown in fig. (2.11) and is consistent with that measured by Tutcher *et al.*<sup>44</sup>

Using this longer dissociation wavelength did not reduce the one-colour background signal. Furthermore the spectrum of this transition proved impractical to assign due to the presence of perturbations by dissociative  $\Pi$  and  $\Sigma^-$  Rydberg states.<sup>45,46</sup> Without a confident assignment of the peaks in the literature or through the use of the PGOPHER<sup>47</sup> program it was not possible to know for certain which peaks probed were of trappable molecular ground states, without lengthy *ab initio* calculations. The cost and working lifetime of the laser dye needed for this wavelength

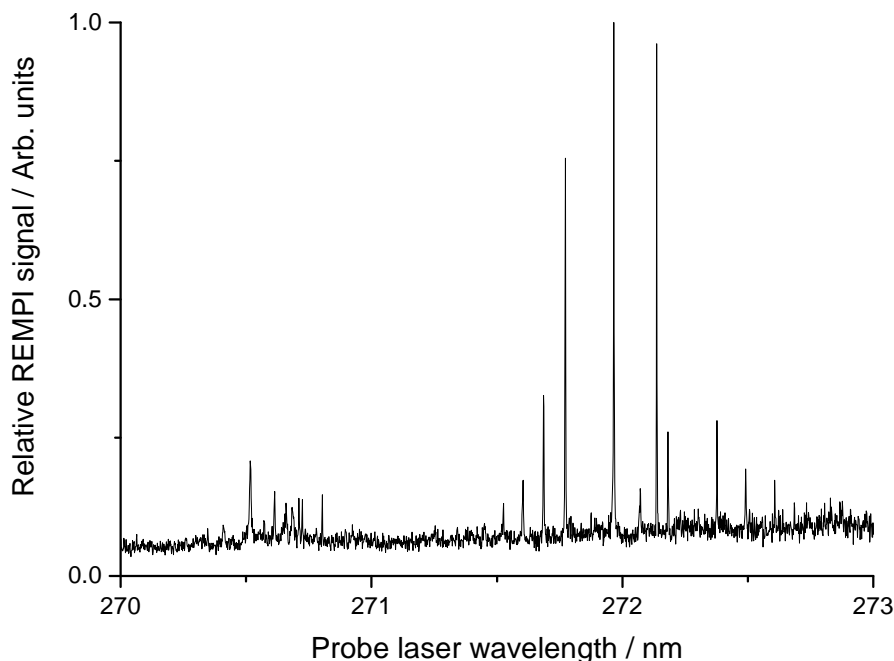


Figure 2.11: (2+1) REMPI excitation spectrum for the  $[a \ ^1\Delta] 4p\pi \ ^2\Phi \leftarrow\leftarrow X \ ^2\Pi_{3/2} (v = 0)$  transition in an SH radical. The spectrum is significantly perturbed by energetically accessible dissociative states; assignment of the peaks was not possible in PGOPHER for this reason. The most intense peak was used for ‘photostopped’ molecules detection however it was not known if this state was trappable. The spectrum was concurrent with a spectrum taken by C. M. Westerns group. A peak at 270.66 nm is attributable to S signal and was strong enough to leak into the SH mass window.

was also not ideal. These three factors meant that this scheme was undesirable compared to the  $78201 \text{ cm}^{-1}$  scheme.

The  $78201 \text{ cm}^{-1}$  scheme was used for the detection of the SH radicals in the trap and a rigorous shot-to-shot background subtraction was used to isolate out the small two-colour cold molecule signal. The experiment was run at 5 Hz but the dissociation laser was only fired every other shot, thus every other shot taken was a one-colour background experiment, by taking the background in alternating shots, the effect of long-term laser-power or molecular-beam change was eliminated.

### 2.3.3 Ion counting algorithms

Events that arrive randomly but at a constant rate can be described by a Poisson distribution; this statistical model is especially useful when the probability of measuring no events in any given experiment is significant. In these experiments, event counting of single SH ions was used.

The simplest way to detect an event is to measure the noise height distribution and the signal

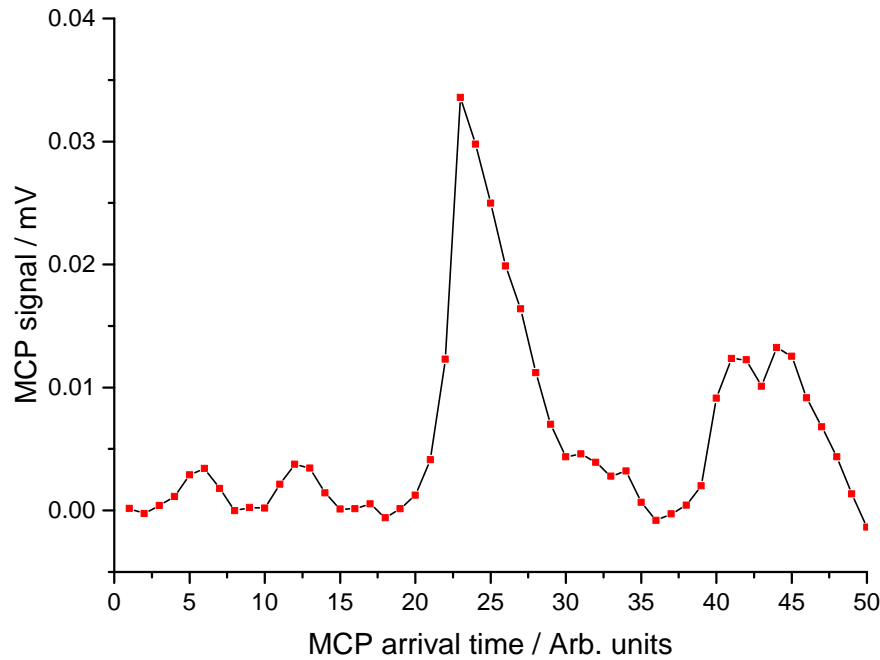


Figure 2.12: Archetypical event-counting data illustrating the experiment specific difficulties in event counting ion signal from the MCP in the photostop experiment.

height distribution and set a counting threshold in between the two distributions that can thus discriminate between signal and noise. This cannot count events that arrive close together in time and so have no distinct baseline between them to reset the counter. Fig. (2.12) shows an archetypical problem specific to the photostop experiment and detector. In the arrival times 40-50 are two events that arrive too close together for a simple threshold to detect. However with the addition of a simple three-point minima-detect algorithm that only activates above the signal threshold this can be correctly determined to be two events.

When some ions hit the MCP they created particularly large signal heights which were followed by a short tail that sat above the normal noise baseline, this was in accordance with the MCP array’s characteristics. This tail could sit approximately at the same voltage as a weaker ion event and so could be confused as another event which it was likely not. To solve this problem, 1000 experiments were manually analysed and determined to contain 475 ion events that followed a Poisson distribution. The algorithms thresholds were then adjusted and carefully checked against the data using a Python 2.7<sup>48</sup> script until the correct count was found. The threshold was then set and the Python script was “translated” into a Labview code and included in the experiments data analysis so that events were correctly counted.

A simple threshold program without minima detection was found to under count by approximately 10 %. As well as this, if a simple single-threshold algorithm was used then the distribution

of detected events per shot would not be a Poisson curve. Instead the algorithm would consistently over-count instances of measuring one event and under-count instances of two or more; this was clear evidence of missing events arriving close together in time causing two events to be counted as one. It was also noted that because the detection window was only 25 ns wide, and that the events could take 5 ns to occur on the MCP it was unrealistic to expect the detection algorithm to reliably measure more than four events in the same experiment consistently. Therefore the Poisson distribution,

$$P(C) = \frac{R^C \times e^{-R}}{C!}, \quad (2.3.3)$$

in which  $P(C)$  is the normalised probability of a given number of counts,  $C$ , occurring in a shot at a constant arrival rate,  $R$ , was used to write another feature in the Labview program. This feature would alert during an experiment if the arrival rate was high enough that some shots were likely to contain five events and thus not be counted reliably.

## 2.4 Simulation

The simulation work in this thesis could not have been completed without the work of Lewis Picard, he wrote most of the functions and programs that make up the photostop simulation program. Indeed the best source of detail about these programs is his masters level report from 2017 or the programs themselves. I will explain here briefly how the simulation works before showing results later on and in other chapters.

Photostop is, in principle, amenable to a simple molecular dynamics simulation in an external field potential. If the photodissociation proceeds through a known process as in equation (2.3.2) and from a known molecular beam profile, an array can be made that describes the photofragments' velocities and positions after photodissociation. This array, as long as the magnetic trapping potential,  $H$ , and its gradient is known, can be propagated through time and space using the velocity Verlet algorithm,

$$\nu(t + \frac{\Delta t}{2}) = \nu(t) + \frac{a(t)\Delta t}{2} \quad (2.4.1)$$

$$x(t + \Delta t) = x(t) + \nu(t + \frac{\Delta t}{2})\Delta t \quad (2.4.2)$$

$$a(t + \Delta t) = -\frac{\delta H(x)}{\delta x} \quad (2.4.3)$$

$$\nu(t + \Delta t) = \nu(t + \frac{\Delta t}{2}) + \frac{a(t + \Delta t)\Delta t}{2}. \quad (2.4.4)$$

In which  $\nu$  is a molecular velocity,  $x$  a molecular position and  $a$  is a molecular acceleration, all of which are computed in three, spatial, Cartesian dimensions.  $\Delta$  is the unit-less step-size of the algorithm, if  $\Delta$  is too great then the photofragments will not interact with significant field potential features, if it is too small the simulation will take too long.

A magnetic field potential,  $H$ , can almost always be described numerically by another array and programs exist that can produce such arrays. In the case of two opposing ring magnets, the field and field gradient can also be described analytically by equations detailed in the work of Babic *et al.*<sup>49</sup>

The biggest difficulty in simulating a photostop trapping experiment is the processing time required to propagate  $10^7$  or more particles through a field potential. A significant shortcut can be taken that makes the program more practical. The initial array of up to  $10^7$  photofragments can be generated in seconds. This array can then be filtered and only the particles that stand a chance of being confined by a trapping field are propagated through time by velocity Verlet algorithm. The particles with an initial velocity significantly above the trap capture velocity are considered to have left the trap at a time after photodissociation easily determined by their initial velocity and position. Often this reduces the computation time needed by several orders of magnitude. A simulation that previously took approximately 3 weeks was completed in 15 minutes.

The simulation can show position and velocity distributions of the trapped particles by reading out after any given velocity Verlet time step. The relative number of particles from photodissociation that remain in the trap volume or probe laser volume at a given time after photostop can also be found and compared with experiment to reinforce experimental data with reliable simulation. Molecular dynamics movies can be produced that show the propagation of the trapped particles through the trap to better understand how the particles behave.

## 2.5 Results and discussion

### 2.5.1 Data analysis and error sources

The relative REMPI signal,  $S_{\text{REMPI}}$ , was found by first maximising the signal at zero dissociation-to-probe-laser delay, this signal was then normalised against laser powers by,

$$S_{\text{REMPI}} = \frac{S_{\text{MCP}}}{P_{\text{probe}}^q \times P_{\text{dissociation}}^r}, \quad (2.5.1)$$

in which  $q$  and  $r$  are the laser power,  $P_{\text{probe/dissociation}}$ , dependencies of the signal,  $S_{\text{MCP}}$ , to each laser. Typically  $r$  was close to 1 and  $q$  was 2.2. These could be approximately predicted by the number of photons expected in the rate determining step of the REMPI scheme. They were measured by keeping one laser at constant power, varying the other and adjusting for one-colour background signal. It was shown that the REMPI signal was not saturated with respect to either of the laser powers. The area integration error in  $S_{\text{REMPI}}$  was determined by propagating the standard error in  $S_{\text{MCP}}$ .

As the delay between the probe and dissociation lasers was increased, the signal strength dropped and was determined in the same way and assigned a value relative to the maximum signal. As the signal range was so great, the MCP detection voltage was changed by several hundred volts

across the experiment, the laser powers were increased and a switch was made from area integration to event counting to measure smaller signals. Whenever any experimental detection parameters were changed, a measurement was taken with both sets of parameters at the same laser delay to allow calibration as the detection setup changed. In this way the low signal strength at long laser delays could be compared to the maximum signal even if the detection parameters were very different. As a significant one-colour background signal was present, the experiment was run with a shot-to-shot background subtraction in which the dissociation laser was blocked. This meant that,

$$S_{\text{REMPI}}^{\text{backsub}} = S_{\text{total}} - S_{\text{background}}, \quad (2.5.2)$$

in which  $S_{\text{REMPI}}^{\text{backsub}}$  was the background subtracted signal proportional to SH density,  $S_{\text{total}}$  is the one- and two-colour signal together when both lasers were fired and  $S_{\text{background}}$  is the one-colour signal isolated by just firing the probing laser.

The error in the background subtracted REMPI signal during event counting at low signal intensity was found by a combination of the Poisson error in the event counting signal and the stability in the laser power by,

$$\delta S_{\text{REMPI}}^{\text{backsub}} = S_{\text{REMPI}}^{\text{backsub}} \sqrt{\left(\frac{1}{\sqrt{N_{\text{signal}}}}\right)^2 + \left(\frac{\sqrt{N_{\text{background}}}}{N_{\text{signal}}}\right)^2 + (f_{\text{laser}})^2}, \quad (2.5.3)$$

in which  $N_{\text{signal}}$  and  $N_{\text{background}}$  are the number of signal and background events counted at a given laser delay,  $f_{\text{laser}}$  is the typically negligible fractional error of the laser power and  $S_{\text{REMPI}}^{\text{backsub}}$  is the background subtracted SH REMPI signal. The variation in the molecular beam profile was another potential error source but was shown by measurements at the start and end of a long day of measurement to be small in comparison to Poisson errors. Any variation in the molecular beam was kept consistent as much as possible by maintaining the same distance to the trap from the nozzle, the same spring tension, the same backing gas composition and pressure and the same solenoid opening current.

The experiment was repeated for twenty days of measurement to obtain enough data for necessary statistical certainty with a rest day in-between each day's measurement, this was necessary to unload the cryopump to keep its pumping efficiency high. Each measurement below  $10^{-6}$  relative signal strength required at least 30000 laser-shots and some as many as 60000. To ensure measurements were comparable day-to-day, the measurements were always started at maximum signal strength and calibrated down to the lowest strength measured. This meant far more data than was needed was recorded at short delay times; this data was thus averaged to reduce clutter on any plot. Laser powers, MCP integral averages, event counting totals and the arrival times of each event counted were recorded. This allowed time-of-flight distributions to be produced as in fig. (2.14).

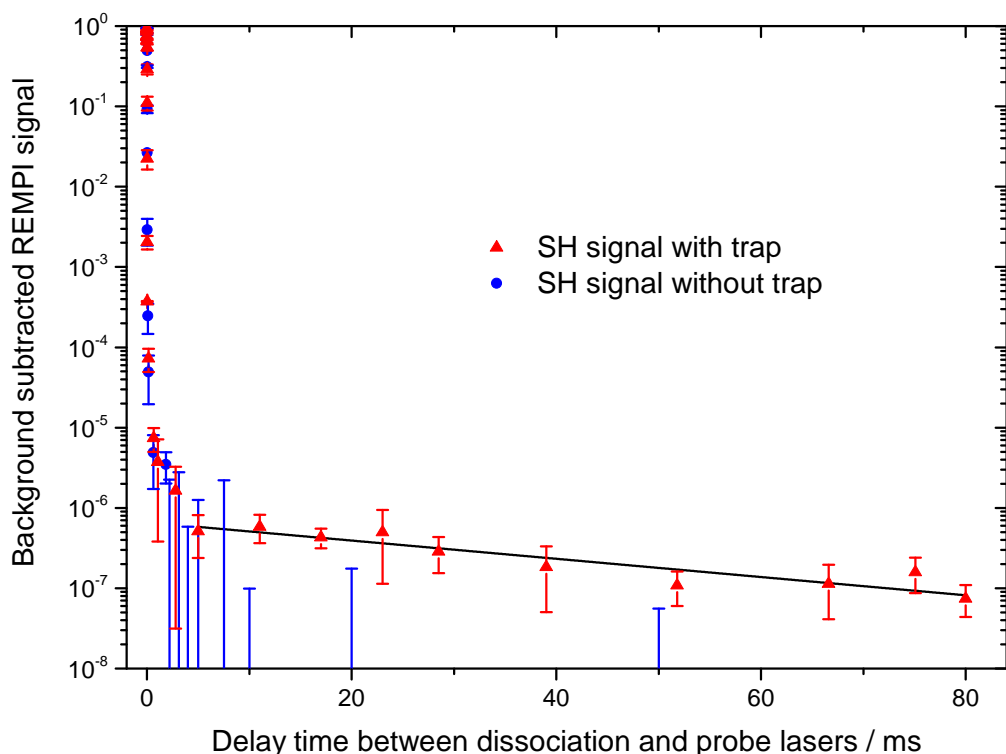


Figure 2.13: Background-subtracted signal as a function of delay between dissociation and probe lasers, error bars are one standard error. Red triangle points: with a trapping magnetic field potential. Black line: linear regression of trapping data with a delay greater than 5 ms showing a  $1/e$  lifetime of  $40 \pm 10$  ms. Blue circle points: without a trapping magnetic field potential. Some blue error bars are without associated points, this was due to the photostopped SH signal becoming immeasurably small compared to the background.

### 2.5.2 SH trapping results

SH radicals were shown to be produced by photostop and are shown in fig. (2.13) by the red data points that have had one-colour background signal subtracted from the two-colour experiment. The blue data points display data taken without a magnetic trap and clearly show a lack of SH radicals 5 ms after photostop.

Fig. (2.13) shows that SH radicals were produced in a trappable state and trapped by a static magnetic trap. The trapped radicals' maximum temperature was 330 mK however the bandwidth of the probe laser was too broad for the Doppler measurements needed to measure the velocities of the trapped radicals. A radio-frequency knife-edge measurement<sup>50</sup> could potentially be used to give an idea of the velocity distribution of the trapped radicals. Fitting a Maxwell-Boltzmann distribution with less than 1 % molecules above 330 mK gives a SH radical temperature of 40 mK which is a reasonable estimate. Further evidence of trapping can be seen in fig. (2.14) which shows the difference in SH time-of-flight distributions between having a magnetic trap and not.

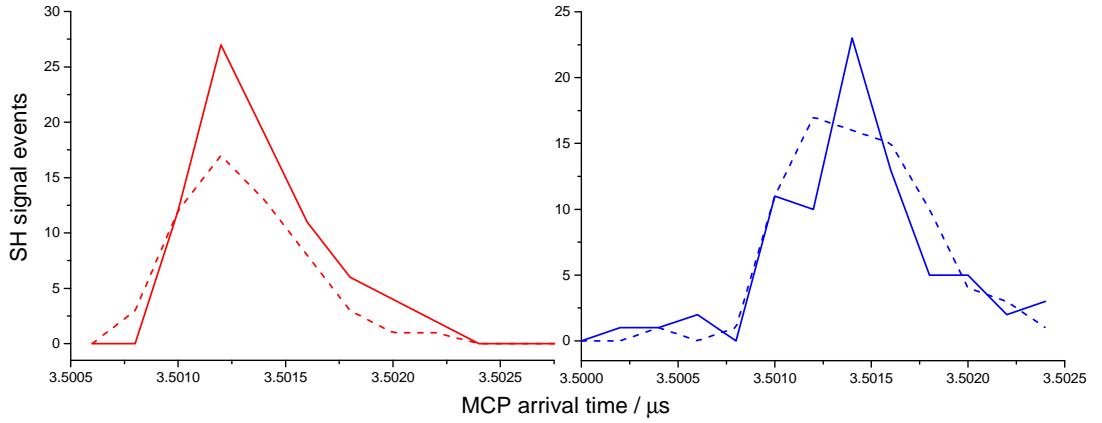


Figure 2.14: Time-of-flight distributions of detected SH ions (histogram bin width 2 ns). Total signal,  $S_{\text{total}}$ , recorded with both dissociation and probe lasers (solid lines) and background signal,  $S_{\text{background}}$ , recorded with probe laser only (dashed lines). The difference yields the background-subtracted SH signal,  $S_{\text{REMPI}}^{\text{backsub}}$ , as plotted in fig. (2.13). Measurements with the magnetic trap at 11 ms delay (red lines) and without a trapping field at 10 ms delay (blue lines).

This shows clearly that the presence of a magnetic trap increased the signal relative to the background measurement. The trapping lifetime of the SH radicals was measured to be  $40 \pm 10$  ms. Initial simulations showed small discrepancies to the measured curve but broadly the simulations concurred with the data and crucially the simulated data predicted almost the same number of trapped molecules produced at zero delay time.

Fig. (2.15) shows a simulation of  $2.5 \times 10^8$  SH radicals, along with a fitted dampened harmonic oscillator trace and some of the experimental data from fig. (2.13). The simulation code used was that described in the experimental section with measured experimental parameters including: molecular beam profiles and estimated velocity distributions, laser wavelengths and polarisations, magnetic trap characteristics and background gas concentrations. Good agreement between simulation and experiment was observed in general. Additionally the simulations revealed the possibility that the photostopped radicals exhibit a group 'breathing' inside the trap with a lifetime shorter than that of the trap lifetime and a period of 0.19 ms. This 'breathing' motion of the trapped radicals was caused by photostopped radicals reaching the edge of the trap and then turning back to the centre periodically and had a limited lifetime due to the trap shape and dissociation volume being non-symmetric. This 'breathing' motion could be reasonably fitted by a dampened harmonic oscillation and thus the whole simulation profile could be fitted by,

$$N(t) = N_0 e^{-\frac{t}{\tau_d}} + a e^{-\gamma t} \cos(\omega t - \phi), \quad (2.5.4)$$

in which  $N$  and  $N_0$  are the number of radicals at time  $t$  and time  $t = 0$ , respectively,  $\tau_d$  is the trap decay time,  $\omega$  the breathing frequency,  $\gamma$  the damping frequency,  $a$  the breathing amplitude and  $\phi$  the phase offset. All of the parameters were floated to fit the simulation.



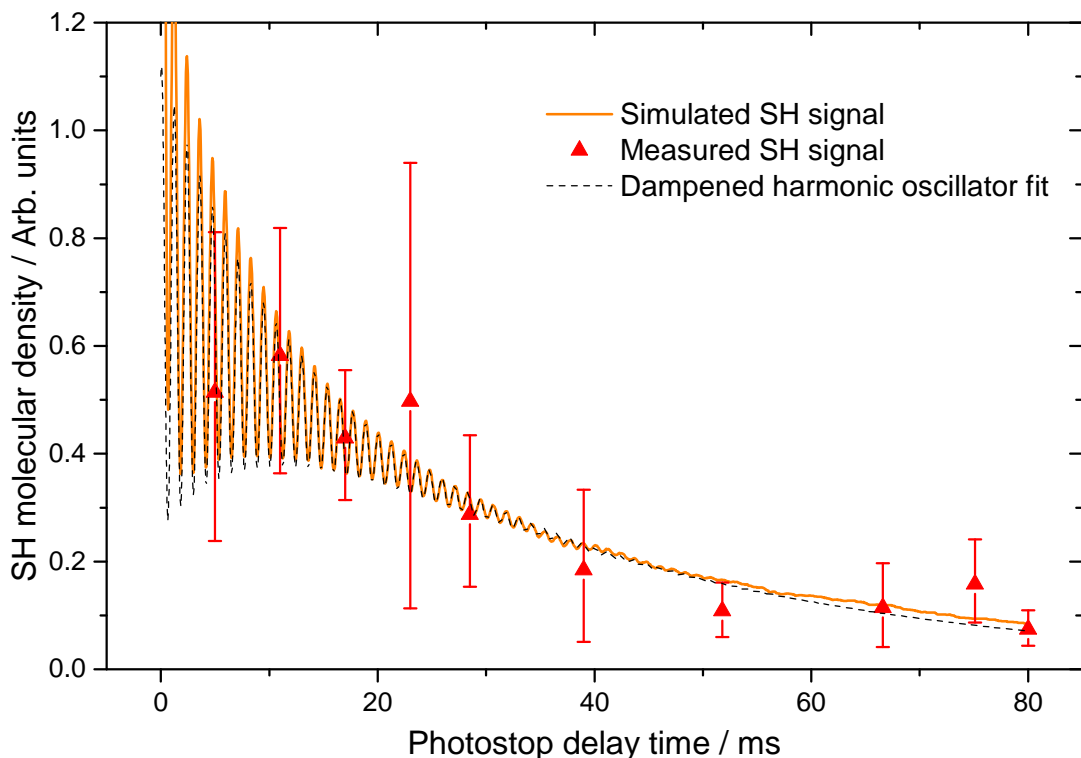


Figure 2.15: Comparison of trapped SH measured data and velocity Verlet simulation of  $2.5 \times 10^8$  SH radicals, along with a fitted dampened harmonic oscillator trace. Although the measurement technically agrees with the trap 'breathing', the size of the error bars on the measurement make confirmation of the radical oscillations in the trap impossible.

During the course of this experiment the trap breathing was not known, however even with prior knowledge, the breathing would not have been possible to confidently detect due to its maximum amplitude being similar to the error on the density measurements.

## 2.6 Conclusions

Photostop has produced neutral radicals that remain in the region in which they were trapped in for at least 80 ms and potentially longer. An estimate of  $\text{H}_2\text{S}$  number density at the moment of photodissociation of  $10^{14} \text{ cm}^{-3}$  based on the dynamics of supersonic expansions was made.<sup>7</sup> Given the dissociation laser peak intensity of  $7.5 \text{ MW/cm}^2$  across the molecular beam, the  $\text{H}_2\text{S}$  absorption cross section of  $2.4 \times 10^{-18} \text{ cm}^2$  at 212.8 nm and unity dissociation yield we estimate the total SH density to be  $2 \times 10^{12} \text{ cm}^{-3}$ . 5 % of the SH radicals are produced in the correct spectroscopic state,<sup>51</sup> making the maximum measured signal equivalent to  $9 \times 10^{10} \text{ cm}^{-3}$ . The decay curve in fig. (2.13) shows that 0.63 ppm of the SH radicals were created in the correct conditions for trapping. However as the ratio of the probe volume to the volume occupied by the trapped molecules changes from 0.09 to 0.021 as the experiment progresses, the true ratio

is 2.7 ppm. This ratio changes as the photostopped radicals are created in the dissociation laser volume but expand to fill the larger magnetic trap volume, this leads to a trapping density estimate of  $2.4 \times 10^5 \text{ cm}^{-3}$ . This density is quoted without an error as it is an estimate based on molecular beam dynamics, this estimation method is highly sensitive to parameters such as the Mach factor which are not well known with a reliable confidence interval and so giving an error would be misleading.

Although the estimated trap density achieved here is low, this does not preclude sympathetic cooling in a vast excess of refrigerant atoms and combining photostop with a microwave trap could result in no foreseeable additional losses. The modest molecular-beam source used could be improved, yielding up to a factor of ten increase in the number of trapped radicals. Additionally, a magnetic trap with a smaller volume and greater potential gradient would increase the trapped SH density. The modest trapping lifetime could be increased by improved differential pumping and by using a shorter and higher-density molecular beam pulse to minimise the amount of background gas in the trap. The possibility of using photostop to load cold molecules into a dipole trap, formed from standing waves of microwaves in a Fabry-Perot cavity<sup>52</sup> is of particular interest and although not investigated here could be a possible future use of the photostop technique as it can be performed with only optical-access to the trap.

Supporting data for the work presented in this chapter are available under open access through Durham University Collections at <https://doi.org/10.15128/r2ft848q61p>.

# Chapter 3

## SH and SD CELIF

This work was conducted with the help of Laura Blackburn during her masters year project.

### 3.1 SH photostop CELIF experiments

Cavity-enhanced laser-induced-fluorescence (CELIF) has previously shown competitive sensitivity at densities as low as  $(1.1 \pm 0.1) \times 10^5 \text{ cm}^{-3}$ .<sup>40</sup> In this experiment, it was used to attempt to measure SH concentrations from photostop of H<sub>2</sub>S to confirm density estimates made in chapter 2 of this work as well as in Eardley *et al*<sup>34</sup> using the REMPI measurement technique.

#### 3.1.1 Experimental

The experimental conditions were kept as close as possible to chapter 2, with the necessary exceptions of changing the detection system from REMPI to CELIF.

##### CELIF methodology

The standard CELIF methodology has been explained<sup>40</sup> in previous work, a brief explanation will be given here. The laser-induced-fluorescence (LIF) signal during unsaturated conditions can be described by

$$S^{\text{LIF}} = I^{\text{LIF}} \alpha \Gamma g, \quad (3.1.1)$$

where  $I^{\text{LIF}}$  is the light intensity interacting with the molecule,  $\alpha$  is the molecular absorption coefficient which is equal to the cross-section,  $\sigma$ , multiplied by the density,  $\rho$ ;  $\Gamma$  is the fluorescence quantum yield and  $g$  is an instrument dependent detection factor. Under the condition of near total reflectivity mirrors, the CELIF signal can then be described by

$$S^{\text{CELIF}} = \frac{S^{\text{LIF}}}{I^{\text{CRD}}} = \frac{2\alpha \Gamma g}{T}, \quad (3.1.2)$$

where  $I^{\text{CRD}}$  is the time integrated cavity-ringdown (CRD) signal and  $T$  is the cavity-mirror transmission. The  $g/T$  factor is instrument dependent and so must be calibrated using a known con-

centration measurement. (Note that the relation  $R = 1 - T$  is not true, as non-trivial losses in the mirrors and at their surfaces are not considered.) Ideally this would be done using a concentration determined concordantly using cavity-ringdown spectroscopy; this was not possible under the molecular density conditions used here or in SD measurements as the densities were below the limit of detection of the CRD measurement. Thus by taking the ratio

$$\frac{S_{\text{SD/SH}}^{\text{CELIF}}}{S_{\text{N}_2}^{\text{CELIF}}} = \frac{\Gamma_{\text{SD}} \sigma_{\text{SD/SH}} \rho_{\text{SD/SH}} g}{\Gamma_{\text{N}_2} \sigma_{\text{N}_2} \rho_{\text{N}_2} g'}, \quad (3.1.3)$$

the instrument dependent factors can be taken account of with a simple Rayleigh scattering measurement of pure nitrogen gas. By setting the laser polarisation angle to the magic angle and using the same detection setup,  $g$  and  $g'$  equate and vanish. So, as the  $\Gamma_{\text{N}_2}$  factor is 1, eqn. (3.1.3) can be rewritten as

$$\alpha_{\text{SD/SH}} = \frac{\alpha_{\text{N}_2}}{\Gamma_{\text{SD/SH}} S_{\text{N}_2}^{\text{CELIF}}} S_{\text{SD/SH}}^{\text{CELIF}}, \quad (3.1.4)$$

thus the absorption coefficient of the SD/SH radicals can be determined with a known or calculated bandwidth averaged cross-section,  $\sigma_{\text{SD/SH}}$ , and fluorescence quantum yield,  $\Gamma_{\text{SD/SH}}$ , and so can the SD or SH density,  $\rho_{\text{SD/SH}}$ . The CELIF measurements must be taken under conditions of a linear relationship between  $S^{\text{LIF}}$  and  $S^{\text{CRD}}$ .

Even without a source of SH or SD, a small  $S^{\text{CELIF}}$  will be present, this is dealt with by background subtraction using

$$S_{\text{SD/SH}}^{\text{CELIF}} = S_{\text{total}}^{\text{CELIF}} - S_{\text{background}}^{\text{CELIF}}, \quad (3.1.5)$$

where  $S_{\text{total}}^{\text{CELIF}}$  is the total CELIF signal and  $S_{\text{background}}^{\text{CELIF}}$  the background signal not attributable to SD/SH fluorescence. This method was used to determine the absolute molecular-density of the SD in the work of Mizouri *et al.*<sup>40</sup>

The more simple CRD technique was also used to measure  $\sigma_{\text{N}_2}$ , given a known pure  $\text{N}_2$  pressure determined by a Peizo-electric pressure gauge. This can be determined by measuring the gradient

$$\frac{\delta(1/\tau)}{\delta\rho_{\text{N}_2}} = \sigma_{\text{N}_2} c, \quad (3.1.6)$$

in which  $\tau$  is the ringdown time for the cavity and  $c$  the speed of light, this will give  $\sigma_{\text{N}_2}$ .

### Laser systems and cavity optics

The dissociation laser for this experiment was, almost, as described in chapter 2 to ensure the same number of photodissociation events occurred. The only change that had to be made to allow for better signal to noise ratio was to move the entrance port of the dissociation laser and put more irises around the beam profile, this had a negligible impact on the number of photodissociation events.

The CELIF laser was a 323.17 nm beam with a 5 ns pulse width used to detect SH on the  $\text{P}_1(1.5)$  line of the (0,0)-band of the  $\text{A}^2\Sigma^+ \leftarrow \text{X}^2\Pi_{3/2}$  transition. It was formed by doubling the

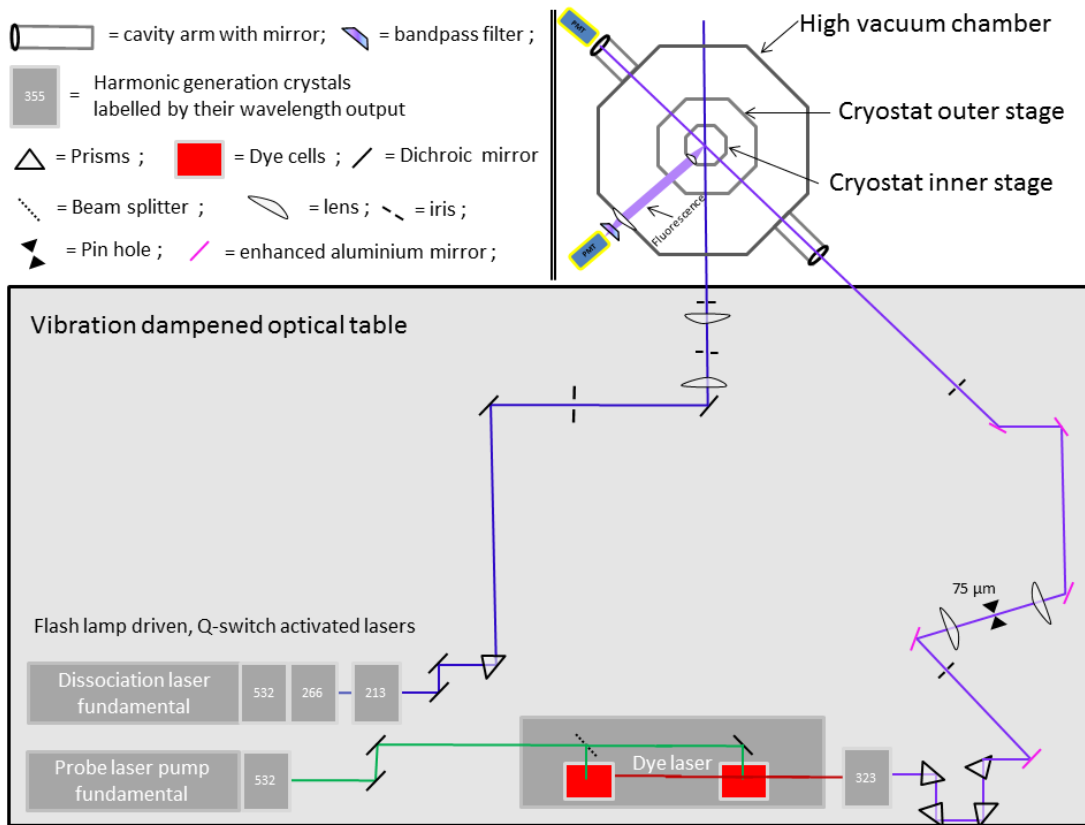


Figure 3.1: Birds-eye schematic view of optical setup for the SH photostop experiment with CELIF, key is shown in figure. The Dye laser components have been simplified as has the experiment chamber and schematic is not strictly to scale.

output of a 532 nm pumped and internally amplified dye laser (Sirah Cobra-Stretch, 0.3 g/L DCM in methanol) and typically had a pulse power of 0.1 mJ. The pump laser was a frequency-doubled solid-state laser (Continuum, Surelite i-10, 10 Hz) that was wavelength separated by four dichroic mirrors.

The 323.17 nm beam was passed through a 2:1 reducing telescope of  $\text{CaF}_2$  lenses ( $f = 200$  and  $100$  mm) with a  $75 \mu\text{m}$  pinhole at its centre. This gave a pseudo-Gaussian laser beam profile with a  $e^{-2}$  radius of 0.29 mm in the vertical and 0.27 mm in the horizontal plane. A  $f = 350$  mm lens was used 15 mm from the first cavity mirror as a mode matching lens for the  $L = 1102 \pm 0.8$  mm cavity made between two  $R = 0.9980 \pm 0.0007$  mirrors with a 1 m radius of curvature (Layertec 105139). The cavity was intentionally made as a non-magic cavity to reduce mode-beating effects. The cavity ringdown signal was optimised to reduce mode-beating according to the method established by Lee *et al.*<sup>53</sup> and by optimisation of the  $\text{TEM}_{00}$  mode of the cavity using the fast-Fourier-transform of the cavity-ringdown signal.

### Vacuum system and fluorescence collection

The vacuum system and H<sub>2</sub>S source were broadly similar to that described in Chapter 2, with the addition of an optical cavity and lens system for collection of SH fluorescence photons as shown in fig. (3.1). N<sub>2</sub> Rayleigh scattering measurements were also required to calibrate any SH CELIF measurements, these were made with just the CELIF laser and a chamber full of dry N<sub>2</sub> gas between 1 Bar and 1 mBar.

The fluorescence-collection system was made from two lenses positioned to maximise the collection solid-angle and thus fluorescence-collection yield. A variety of lenses and lens positions were trialled to give the best signal to noise ratio. The fluorescence light at 323 nm was filtered by a 320/40 nm BrightLine single-band bandpass filter (Semrock) to exclude as much background light as possible. Spatial filters of various sizes were also trialled but did not show evidence of an improved signal to noise ratio.

The principle background light source originated from the fluorescence of the MgF<sub>2</sub> windows after interaction with the 212.8 nm laser light. Compared to this, the fluorescence from the cavity mirrors was negligible. The fluorescence mechanism and spectrum of these MgF<sub>2</sub> windows under similar light sources has previously been investigated.<sup>54</sup> The fluorescence was found to give a short lifetime emission at low wavelength <230 nm which could be easily filtered and a longer lived and spectroscopically broader emission which peaked at 320 nm which was not possible to filter chromatically or spatially. A delay between dissociation and CELIF lasers of 200 ns was used to wait until after the majority of the MgF<sub>2</sub> window fluorescence to make the CELIF measurement.

### Photon event detection

As discussed in Chapter 2, event counting can often be achieved by simply finding a threshold at a level in between the noise and signal height distributions. This was not a trivial task, as can be seen in fig. (3.2), as the noise and signal distributions were not completely separated and so regardless of where a threshold was put, signal events would be missed and electronic noise counted. A threshold of 0.52 mV was chosen as a compromise between excluding noise and measuring maximum signal. This threshold was set using N<sub>2</sub> Rayleigh scattering measurements and then used in SH experiments.

### 3.1.2 Results and discussion

Successful Rayleigh scattering measurements of N<sub>2</sub> were made and a Rayleigh scattering cross-section,  $\sigma_{\text{N}_2}$ , of  $4 \pm 1 \times 10^{-26}$  cm<sup>2</sup> at 323.17 nm, in agreement with literature,<sup>33</sup> was measured.

As was discussed in the experimental section, the background light coming from fluorescence of the MgF<sub>2</sub> mirrors was a significant problem. It was not possible to reduce this background source to a degree that allowed SH CELIF to be measured. The relatively old ringdown-mirrors that, even when optimised, could not produce ringdown times above 2  $\mu$ s, compared poorly to the

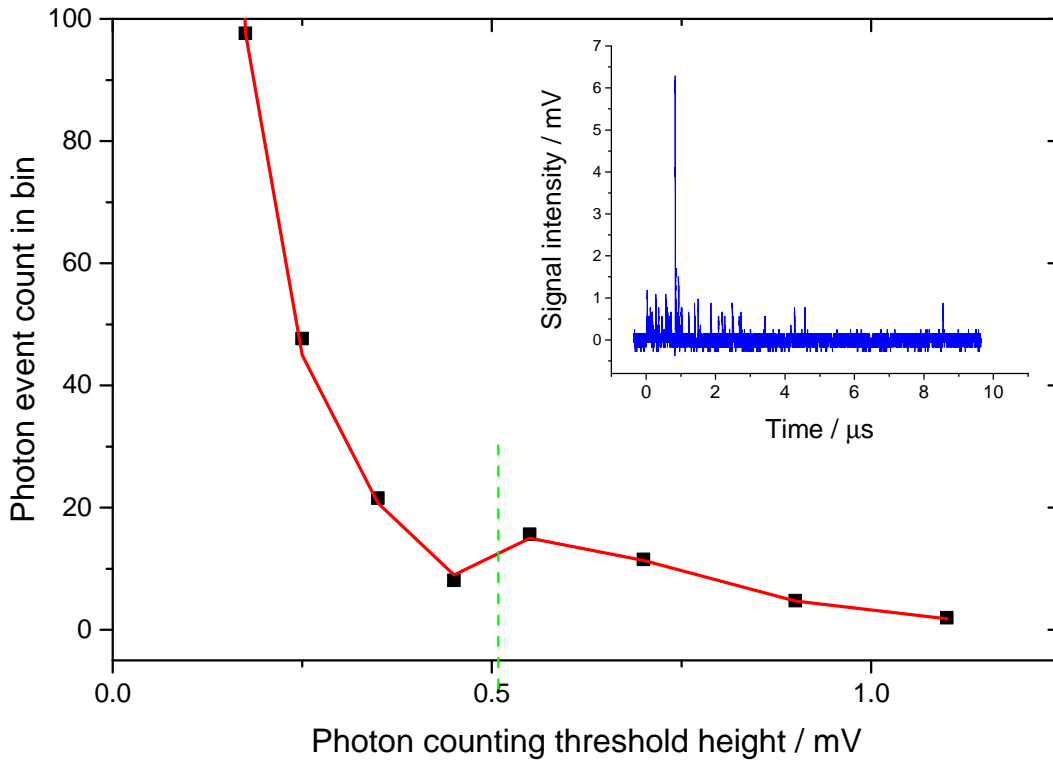


Figure 3.2:  $N_2$  Rayleigh scattering photon event counts in bins (0.2 mV width) from 0 to 1.1 mV (black data points) with a fit to data taking account of electronic noise height profile and Rayleigh scattering height profile (red curve), green dashed line is the chosen threshold for event counting based on this data. Inset is a typical  $N_2$  Rayleigh scattering trace from a CELIF experiment.

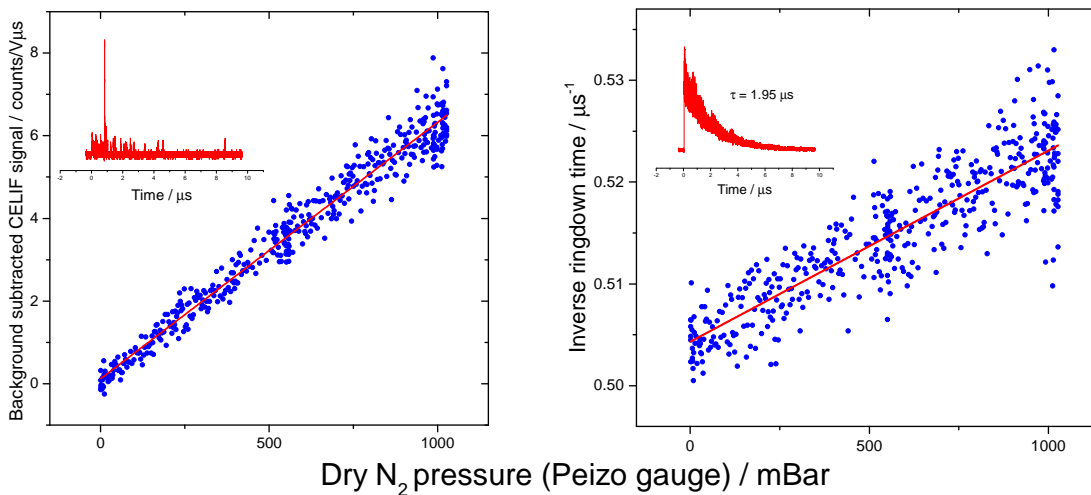


Figure 3.3: Left: linearity of  $N_2$  Rayleigh scattering CELIF signal with  $N_2$  pressure, inset: typical Rayleigh scattering trace. Right: linearity of  $N_2$  Rayleigh scattering against  $1/CRD$  signal with  $N_2$  pressure, used to give  $\sigma_{N_2}$ , inset: typical cavity ringdown trace with ringdown time. Both plots feature a linear fit (red line.)

performance obtained by N. Warner<sup>33</sup> and contributed to the poorer sensitivity. It was possible to reduce the background to a degree similar to that found by N. Warner by using significantly longer delay times between lasers. This delay between dissociation and CELIF lasers gave time for SH radicals to leave the probe volume however and likely reduced any CELIF signal attributable to SH. This combined with the low ringdown times prevented successful detection of SH radicals and by extension an absolute density-measurement of trapped SH radicals in chapter 2.

### 3.1.3 Conclusions

The purpose of this experiment was to give an absolute density calibration to a relative measurement. A better signal to noise ratio is required for this experiment to produce the anticipated data. The most promising avenues for making these improvements are as follows.

Higher reflectivity cavity mirrors which would improve CELIF sensitivity by increasing the ringdown-time. A narrower bandwidth CELIF probe laser which would allow a greater number of photons from the probe to be absorbed by SH radicals. A lower dark count PMT which would have a minor role in reducing background on the fluorescence detection. Finally the removal of line-of-sight between MgF<sub>2</sub> mirrors and fluorescence collection optics most likely achieved through mounting dichroic 212.8 nm mirrors in vacuum and introducing more sophisticated light baffles. This would reduce the most problematic background source from the MgF<sub>2</sub> windows.

## 3.2 SD Stark deceleration CELIF

Experimental work in this section was performed in Vancouver by O. Nourbakhsh and was analysed in Durham, it is presented in this thesis as the author was heavily involved in that analysis.

Cavity-enhanced laser-induced-fluorescence (CELIF) was used to measure SD radicals at a density of  $(1.9 \pm 0.5) \times 10^9 \text{ cm}^{-3}$  after velocity bunching by a Stark decelerator to 440 m/s.<sup>55</sup> The improvement of the technique's time resolution was investigated to measure molecular densities that change significantly on a sub-microsecond timescale. Simulations have shown its capability to give improved spatial resolution of molecules in static trapping field potentials. These improvements potentially allow CELIF to be used in measurements of absolute collision cross-sections of decelerated molecules and to rigorously determine decelerator efficiency's.

### 3.2.1 Introduction

The accurate determination of molecular densities from Stark and Zeeman decelerators is of particular interest for single quantum-state-resolved reaction-dynamics studies.<sup>56</sup> As is a rigorous understanding of absolute decelerator-efficiencies with regard to changes in terminal molecular-velocities and phase angles.<sup>57</sup>



Determinations of molecular density based on expected source and decelerator efficiencies, measured collision rates or by rigorous calibration of laser-induced-fluorescence (LIF) detection setups are challenging and often imprecise. Kirste *et al.* undertook lengthy measurements<sup>58</sup> to obtain absolute OH radical densities as low as  $200 \text{ cm}^{-3}$  with a 30 % error. Stuhl *et al.* used measured collision rates<sup>50</sup> to infer trapped OH radical densities of  $5 \times 10^{10} \text{ cm}^{-3}$  but no supporting absorption imaging measurements were made and these measurements are inconsistent with broadly comparable experiments.<sup>59</sup> The use of the CELIF technique for this purpose is potentially insightful and generic.

### 3.2.2 Experimental

The experimental setup was broadly similar to that described<sup>55</sup> in Nourbaksh *et al.* and will be described here briefly with focus on the change in the detection setup from LIF to CELIF.

The Stark decelerator was built based on the work<sup>60</sup> of Meijer *et al.* and consisted of 180 alternating electrode pairs that switch a DC voltage of  $\pm 12 \text{ kV}$ . The decelerator was loaded with SD radicals produced by glow discharge of a supersonic molecular-beam of  $\text{D}_2\text{S}$  in krypton carrier gas. The SD radicals were bunched by the decelerator to  $440 \text{ m/s}$  and detected by CELIF on the  $P_1(1.5)$  line of the (0,0)-band of the  $A^2\Sigma^+ \leftarrow X^2\Pi_{3/2}$  transition at  $323.17 \text{ nm}$ . The probe light was produced by frequency-doubling a Nd:YAG pumped dye laser (Radiant, NarrowScan with DCM dye; Spectra Physics, Quanta Ray Pro-230-10, nanosecond pulsed). The probe light had an  $e^{-2}$  diameter of  $4.2 \text{ mm}$  and typical pulse power of  $0.3 \text{ mJ}$ .

The light was coupled into an optical cavity of length  $90 \text{ cm}$  and  $0.2 \text{ mm}$  beam waist between two curved cavity mirrors (Layertec 105139,  $R > 99.8 \%$ , radius of curvature of  $100 \text{ cm}$ ) and the light exiting the cavity was detected by a photodiode (Thorlabs PDA36A). Good coupling into the  $\text{TEM}_{00}$  of the cavity was achieved using a spatial filter, coupling lens, telescope and pinhole setup as suggested by S. Greaves. The light was linearly polarised at the magic angle, to the fluorescence detector (Hamamatsu PMT, H11526-010NF) to eliminate fluorescence angular dependence. The fluorescence light was imaged onto the detector by a dual-lens collection telescope without spatial or chromatic filtering. Similarly to SH measurements discussed earlier in the chapter, nitrogen Rayleigh scattering measurements were made to provide a density calibration, the method was broadly the same as in the previous section.

#### Time dependent CELIF methodology

Previous CELIF measurements have assumed that the molecular density remained constant for the measurement time. The CELIF measurement time is often of the order of several  $\mu\text{s}$  and so situations exist that do not satisfy this assumption. This has lead CELIF to be developed to accommodate time varying densities. Following the work<sup>61</sup> of Nakano *et al.*, the  $I^{\text{CRD}}$  is described

as a functional of the time-dependent density by

$$I^{\text{CRD}}[\rho(t)] = I_0 \exp\left(\frac{-t}{\tau_0}\right) \exp\left(-c\sigma\rho(t)\right), \quad (3.2.1)$$

where  $I_0$  is the initial CRD intensity,  $\sigma$  is the absorption cross section,  $c$  is the speed of light,  $\tau_0$  is the empty-cavity ringdown time and  $\rho(t)$  is the time-dependent molecular-density. The  $S^{\text{LIF}}$  can be written as

$$S^{\text{LIF}}[\rho(t)] = \frac{g\Gamma\sigma\rho(t)}{T} I_0 \exp\left(\frac{-t}{\tau_0}\right) \exp\left(-c\sigma\rho(t)\right), \quad (3.2.2)$$

in which, as is shown by eqn. (3.1.1),  $S^{\text{LIF}}$  is dependent on the molecular density and the light interacting with that density which, according to eqn. (3.2.1), is also dependent on the molecular density. Eqns. (3.2.1) and (3.2.2) can then be used to give

$$S^{\text{CELIF}}[\rho(t)] = \frac{g\Gamma\sigma\rho(t)}{T}, \quad (3.2.3)$$

which, according to eqn. (3.1.3), can be calibrated with a nitrogen Rayleigh scattering measurement or a CRD measurement. In this way eqn. (3.2.3) can be calibrated by

$$\rho(t) = \frac{\alpha_{\text{N}_2}}{\Gamma\sigma S_{\text{N}_2}^{\text{CELIF}}} S^{\text{CELIF}}. \quad (3.2.4)$$

Thus a time-varying density can be reproduced from a CELIF measurement. If  $\rho(t)$  is a simple function then the density can be found analytically, providing that a good starting point for the function can be estimated and electronic noise in the signal is not too great.

Alternatively,  $S^{\text{CELIF}}$  can be reported multiple times throughout the measurement giving greater time resolution in  $\rho$  without explicitly finding an analytical description. Whereas a normal CELIF measurement will return the average density during the measurement time, if the data is split into time segments then a changing density,  $\rho(t)$ , during the measurement time can be tracked.

### 3.2.3 Results and discussion

The nitrogen Rayleigh scattering measurements were made at pressures of 0.227 - 96000 Pa. Fig. (3.4) shows a plot of  $S_{\text{N}_2}^{\text{CELIF}}$  against nitrogen density, the plot has an inverse gradient of  $(7.0 \pm 0.4) \times 10^{13} \text{ V } \mu\text{s}/\text{cm}^3$ . This gradient is used in combination with eqn. (3.1.4),  $\sigma_{\text{SD}}$ ,  $\sigma_{\text{N}_2}$  and  $\Gamma_{\text{SD}}$  to find  $\rho_{\text{SD}}$  from  $S_{\text{SD}}^{\text{CELIF}}$ . As reported<sup>40</sup> in Mizouri *et al.*  $\Gamma_{\text{SD}} = 0.20 \pm 0.01$  and  $\sigma_{\text{N}_2}(323.17 \text{ nm}) = (4.1 \pm 0.2) \times 10^{-26} \text{ cm}^2$ . The bandwidth averaged cross-section,  $\sigma_{\text{SD}}$ , was determined here to be  $(2.1 \pm 0.1) \times 10^{-16} \text{ cm}^2$  given the laser bandwidth,  $\Delta\nu = 21 \pm 2 \text{ GHz}$ . The probing volumes for the fluorescence and Rayleigh scattering detection setups were not identical. This was due to the finite size of the decelerated molecular packet. The fluorescence field of view was  $2.43 \pm 0.005$  times smaller and so this factor was taken account of in the calibration.

The calibrated  $S_{\text{SD}}^{\text{CELIF}}$  measurement gave a peak SD density in the Stark decelerated packet of  $(1.9 \pm 0.5) \times 10^9 \text{ cm}^{-3}$ . The time-of-flight profile of the packet is shown in fig. (3.5), presented with

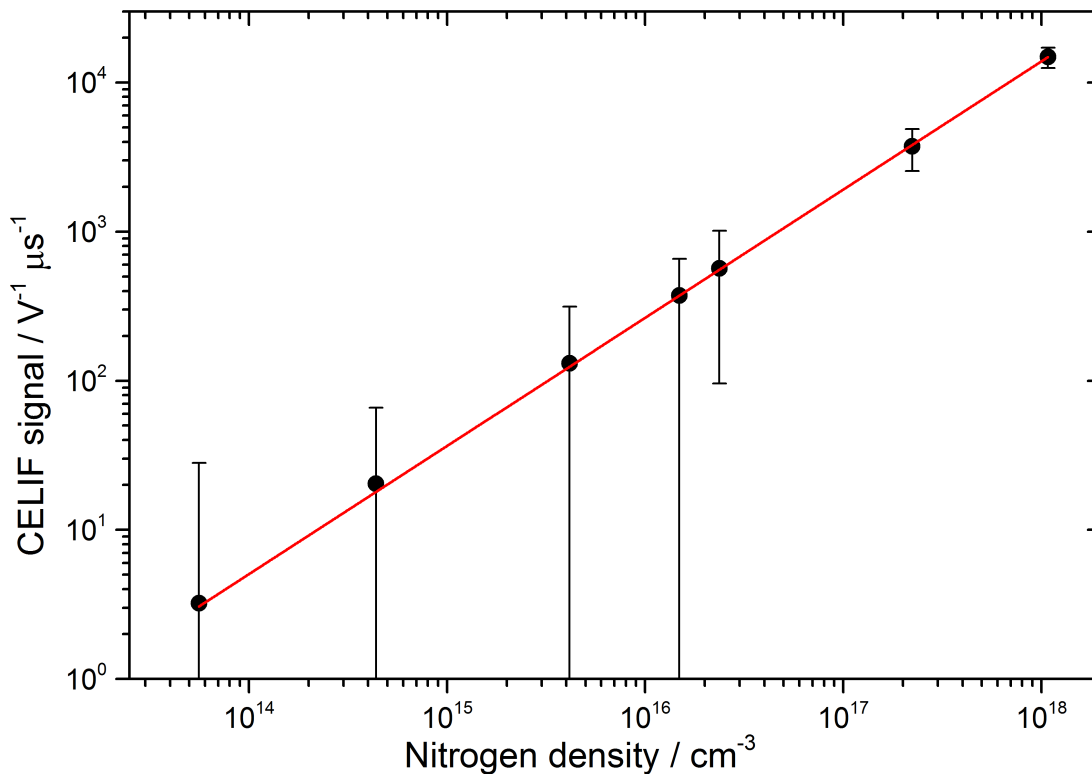


Figure 3.4: Calibration curve for  $\rho_{\text{N}_2}/S_{\text{N}_2}^{\text{CELIF}}$  factor used to put an absolute scale onto CELIF measurements of SD. The line is a linear  $\chi^2$  fit of the data points and the error bars are one standard Poisson error.

it is a series of single pass LIF (spLIF) measurements taken under identical SD source conditions. A  $S_{\text{SD}}^{\text{CELIF}}$  data point gives the average density across the measurement time. The  $S_{\text{SD}}^{\text{CELIF}}$  profile in fig. (3.5) is moved by a constant positive time offset to account for this.

Typical LIF and CRD profiles for Rayleigh scattering and SD fluorescence measurements are given in fig. (3.6), they show that the SD fluorescence signal is in the event counting regime. The errors in the density measurement in fig. (3.5) were dominated by Poisson shot noise in the LIF signal.

### Using time dependent CELIF

It was hoped that one of the time-varying CELIF methods introduced earlier would be used to solve the problem in fig. (3.5) that the CELIF did not perfectly map the spLIF.

As the LIF profiles were in the event counting regime and the CRD profiles contained significant electronic noise, the analytical approach to finding  $\rho(t)$  was not possible. When in the event counting regime  $S^{\text{LIF}}$  has a slow and inconsistent response to  $\rho(t)$  making the analytical time-varying CELIF analysis unrealistic. The signal was in fact too weak even for reporting  $S^{\text{CELIF}}$  more than once for each laser shot and so time-dependent CELIF was not used for this experiment. Additionally, in attempting to conduct this analysis, serious violations of the principle of linearity

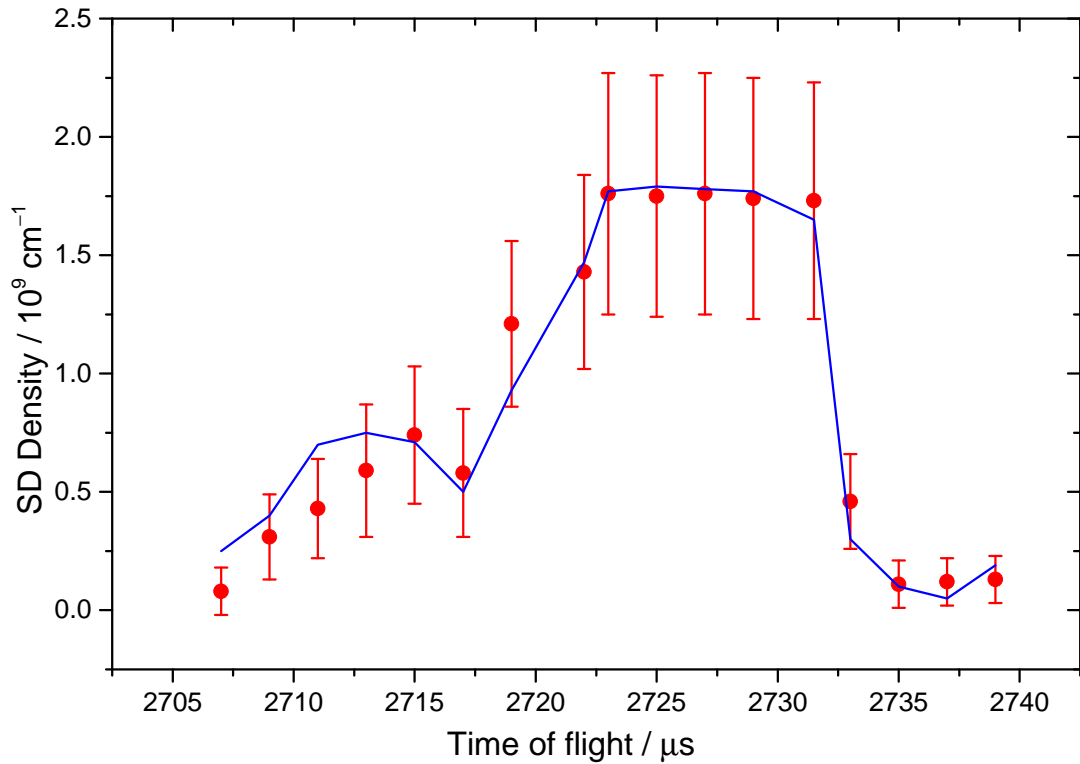


Figure 3.5: Shows the standard time independent CELIF analysis time-of-flight trace (red points) against the single pass LIF trace (blue line), error bars are one standard Poisson error for the CELIF points.

between  $S^{\text{LIF}}$  and  $S^{\text{CRD}}$  were found and investigated. This will be discussed later.

### Flaws and inconsistencies in the Vancouver data set

This experiment was undermined by a breakdown in one of the techniques necessary linearities. A comparison of spLIF to CELIF in fig. (3.5) shows linearity between CELIF and SD density, the calibration curve in fig. (3.4) shows the expected linearity and although the data is not available a linear relationship was reported to be seen between  $S^{\text{LIF}}$  and  $S^{\text{CRD}}$ . Observation of fig. (3.6) undermines the linearity between  $S^{\text{LIF}}$  and  $S^{\text{CRD}}$  within the traces. The arrival rate of LIF events appears independent of the corresponding CRD signal intensity.

Fig. (3.7), conclusively shows a breakdown in linearity, initially it was suspected that the laser intensity was too high and the LIF signal became saturated quickly thus giving the sharp rise to a maximum that persisted until the very end of the trace. Essentially most of the CRD photons were not required as the absorption transition was saturated. Similar measurements made in Durham for Mizouri *et al.*<sup>40</sup> instead show the expected trend with LIF signal only slightly lagging behind CRD signal due to the 190 ns fluorescence lifetime of the SD excited state.

This hypothesis was tested by performing a similar analysis on the nitrogen Rayleigh scattering data from Vancouver. As the process of Rayleigh scattering has an immeasurably small lifetime

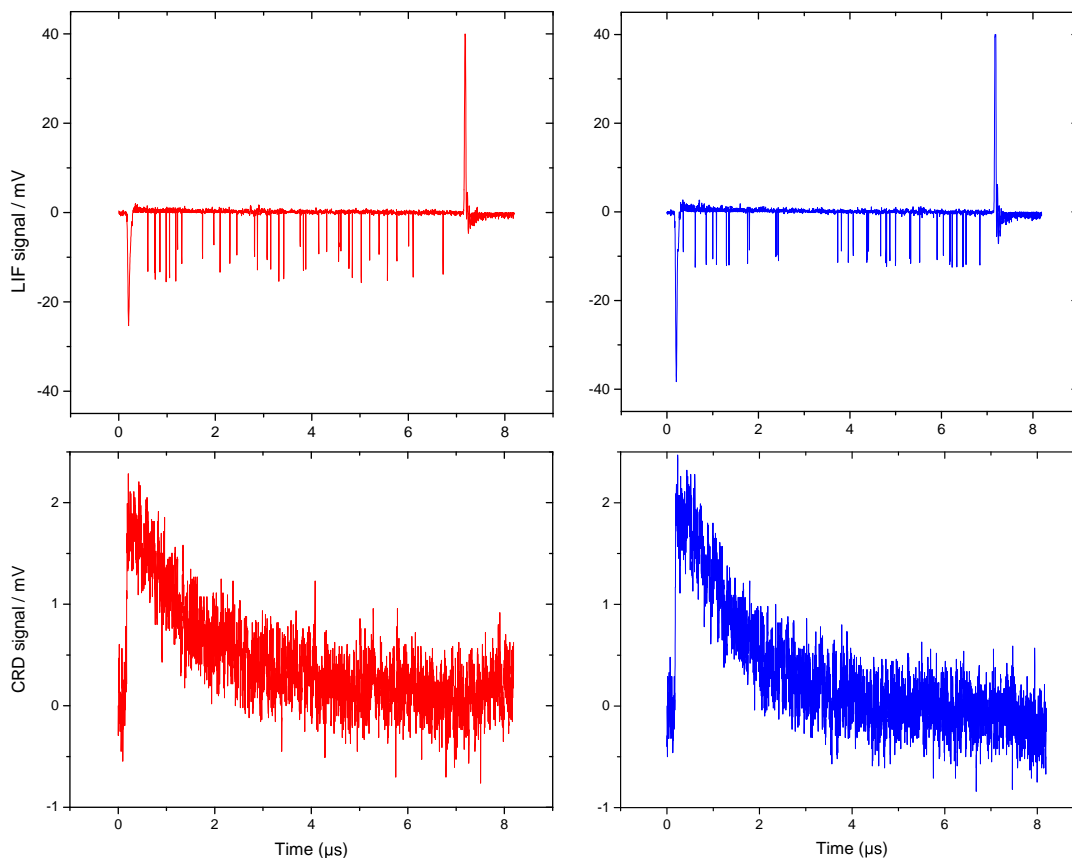


Figure 3.6: Typical traces from CELIF measurement of SD, red traces are from measurements of SD radicals and blue traces are from measurements of  $N_2$  molecules. Top traces are laser induced fluorescence traces and bottom are cavity ringdown traces. Both LIF traces are in the event counting regime,  $> |\pm 20|$  mV peaks correspond to turning the PMT gate on and off.

and there were over  $10^{18}$  nitrogen molecules present, it would seem impossible to run out of ground state nitrogen molecules and saturate the transition. As a result of this, nitrogen Rayleigh scattering measurements should show linearity. The nitrogen Rayleigh scattering data showed a lack of expected linearity similar to the SD CELIF data. Thus the experiment was not fully understood at this time and would have to be repeated before publication.

### 3.2.4 Conclusions

The SD CELIF measurements do appear to map reasonably onto comparable spLIF measurements and the absolute density of the SD radicals determined does appear to agree with Stark deceleration simulation work done in Vancouver. However without repeating the calibration and SD CELIF measurements to fully understand the features discussed above the experiment can progress no further.

One potential explanation could be a molecular contaminant with a long fluorescence lifetime or a fault in the PMT's used for fluorescence detection. Unlike the data taken in Durham, the

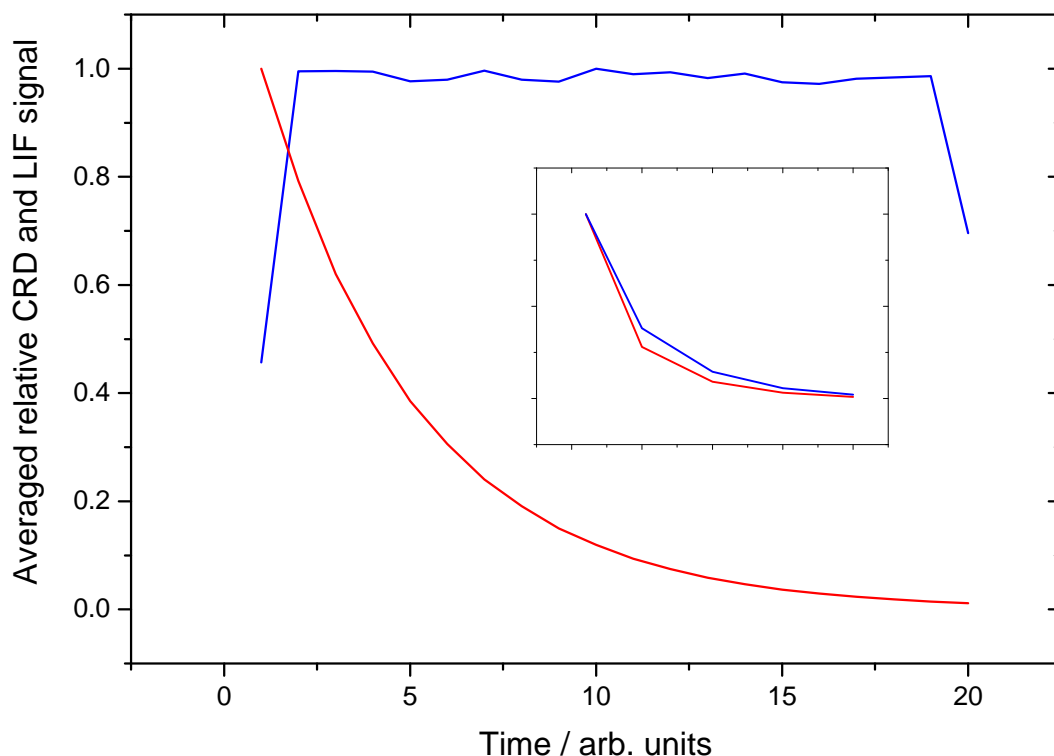


Figure 3.7: Average binned LIF (blue) and CRD (red) traces from 27000 CELIF measurements taken in Vancouver 2015, inset average of 8000 similar traces taken in Durham 2013 for Mizouri *et al.*

Vancouver data set was taken with high voltage gated PMTs. It is possible that these PMTs had a non-negligible charging time during which their amplification factor grew exponentially to its maximum. So that when convoluted with the exponentially decreasing LIF signal a flat line signal was measured, this would be a surprising coincidence. At the time of writing this hypothesis had not been further investigated.

### 3.3 Simulations of CELIF in trapping fields

As an aside to this work, CELIF was also developed to be used to measure absolute densities inside trapping field potentials.

A simulation has been made that adjusts molecular absorption cross-sections due to the influence of electric and magnetic trapping fields as well as laser bandwidths. Input functions are needed to describe: trapping fields, molecular positions, probing volumes and Zeeman or Stark energy shifts. Thus the program can be adapted to a specific experimental setup. The outputs show the molecules that have been simulated in the field that they were simulated in. The convergence of the adjusted cross-section is also shown as a check that the program has converged.

The simulation is non-dynamic and evaluates the problem using two Monte-Carlo decision steps.

The first step generates a sample molecular spatial distribution given an input molecular position function and determines the probability that each molecule will interact with any photon given its location in a CELIF probe volume. This ensures that the correct ensemble of molecules is analysed by the second step. This step could be replaced with an array of known molecular positions inside a probing volume.

The second Monte Carlo step then takes those molecules and computes the chance that they will interact with a resonant photon from the probing laser. This probability considers the molecules absorption energy at its position in the field as well as the bandwidth of the laser. This detection probability is then used such that

$$\sigma_{\text{corrected}} = \frac{\sigma}{p_{\text{detect}} \Delta\nu}, \quad (3.3.5)$$

where  $\sigma_{\text{corrected}}$  is the bandwidth and field corrected cross-section,  $\sigma$  is the uncorrected form,  $p_{\text{detect}}$  is the simulation determined detection probability and  $\Delta\nu$  is the lasers bandwidth. This program does not require a field gradient function or molecule propagation algorithms both of which are complicated and computationally time consuming. The program assumes that molecules propagating through a changing laser and electric or magnetic field can be represented by a large set of stationary molecules and that fluorescence cannot occur multiple times from the same molecule. It will output a corrected cross-section that can be used to correct for laser-bandwidths and field potentials in a CELIF experiment.

### 3.3.1 Sample simulation results

CELIF detection using a typical probe volume has been simulated for a 100 mK thermal distribution of SD radicals inside a 3 dimensional Gaussian magnetic trap 0.41 T deep in all dimensions. The simulation showed that molecules inside the probe volume had an  $81.9 \pm 0.1$  % chance of detection due to their Zeeman shifts and the lasers bandwidth. This gave  $\sigma_{\text{corrected}} = (2.3 \pm 0.1) \times 10^{-16} \text{ cm}^2$  with a laser bandwidth,  $\Delta\nu = 21 \pm 2 \text{ GHz}$ .

Fig. (3.8) shows the distribution of SD molecules in the trap that were detected. A Zeeman and bandwidth corrected CELIF measurement used in conjunction with a measurement or simulation of the trapped molecules spatial distribution will give absolute peak densities of trapped molecules if the average density of the trap is above the CELIF measurements limit-of-detection.

Supporting data for the work presented in this chapter are available under open access through Durham University Collections at <https://doi.org/10.15128/r2vm40xr576>.

Supporting data for the work presented in this chapter from Vancouver are available upon request from the author and with permission of the original supplier.

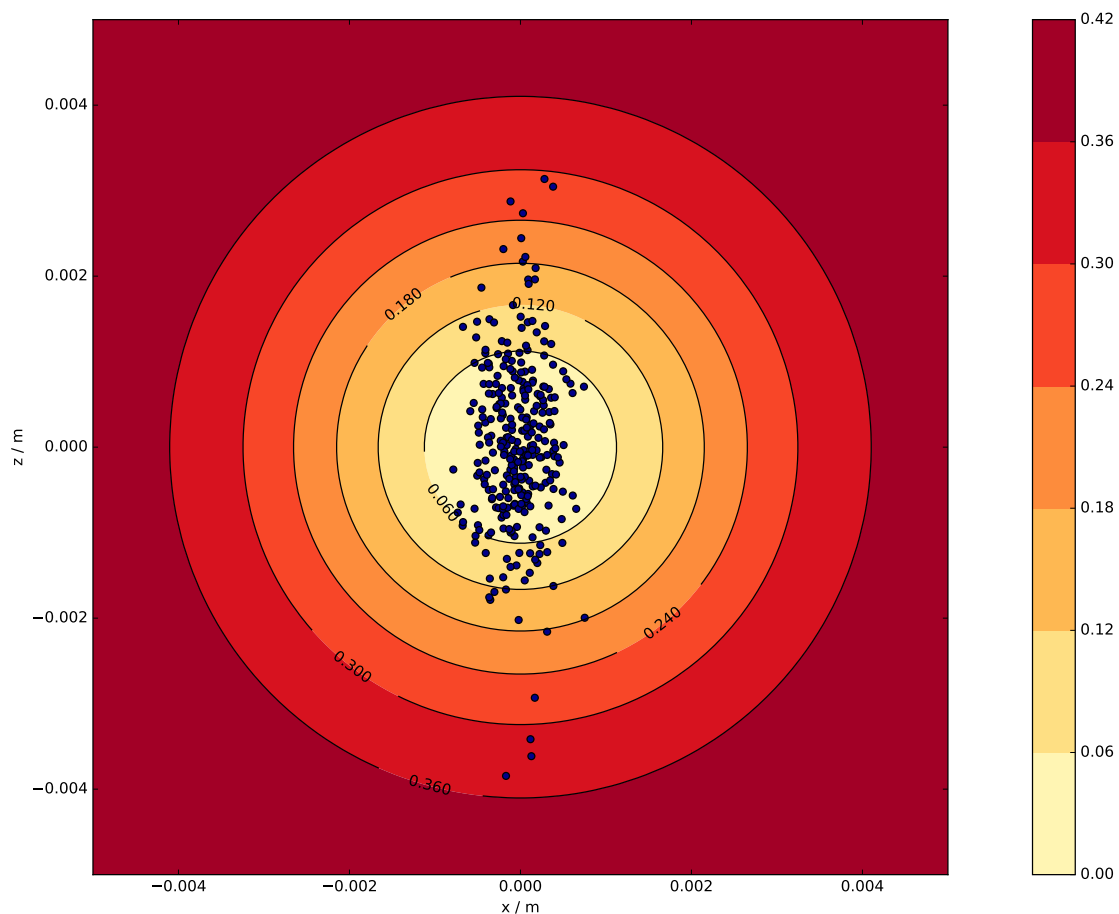


Figure 3.8: Simulated detection positions of SD radicals, blue circles, in a 3 dimensional Gaussian magnetic trap 0.41 T in depth. The colour bar axis shows magnetic trap depth in Tesla. Molecules are detected more frequently in the trap centre due to a smaller Zeeman shift as well as being there more frequently. the particles are detected along a line in the z axis as this is the probe laser axis.



## Chapter 4

# Atomic oxygen photostop

This work was conducted with help from Lewis Picard, Laura Blackburn and Ed Gardner during their respective masters year projects. This chapter is split into two sections, the first concerning imaging of photostop of atomic oxygen and the second concerning trapping in a different instrument.

### 4.1 Introduction

In recent decades, the field of cold and ultracold molecules has seen an explosion in the use of laser cooling of molecular species.<sup>62</sup> Many important, chemically relevant and potentially highly dipolar species are not easily amenable to laser cooling, or require additional preparation techniques to bring molecules into the cooling range of lasers. Work has been done to develop methods for producing cold and controlled sources of H, O, C and N atoms, as the building blocks for most organic molecules.<sup>13,35,63-66</sup> At the time of writing, O atoms were yet to be experimentally trapped but had been produced as a cold beam from a Zeeman decelerator and from bent magnetic guiding.<sup>64,65</sup>

Atomic oxygen has now been magnetically trapped after photostop of precursor NO<sub>2</sub> molecules with a trapping lifetime of  $82 \pm 3$  ms and a maximum density of  $3000 \pm 900$  cm<sup>-3</sup>. Although the maximum density achieved in this experiment was disappointing, there are several promising directions that could be taken for improvement in the future.

Photostop presents a method of producing cold trapped O atoms that can then potentially be sympathetically cooled or laser cooled by a mode locked UV frequency comb setup with a high repetition rate laser.<sup>63</sup> Cold or ultracold atomic oxygen could be used for low-energy collision studies<sup>67,68</sup> to test theory benchmarks,<sup>69</sup> to understand important combustion chemistry reactions<sup>70</sup> or potentially associated with Rb to produce RbO, a molecule with a high electric-dipole moment.

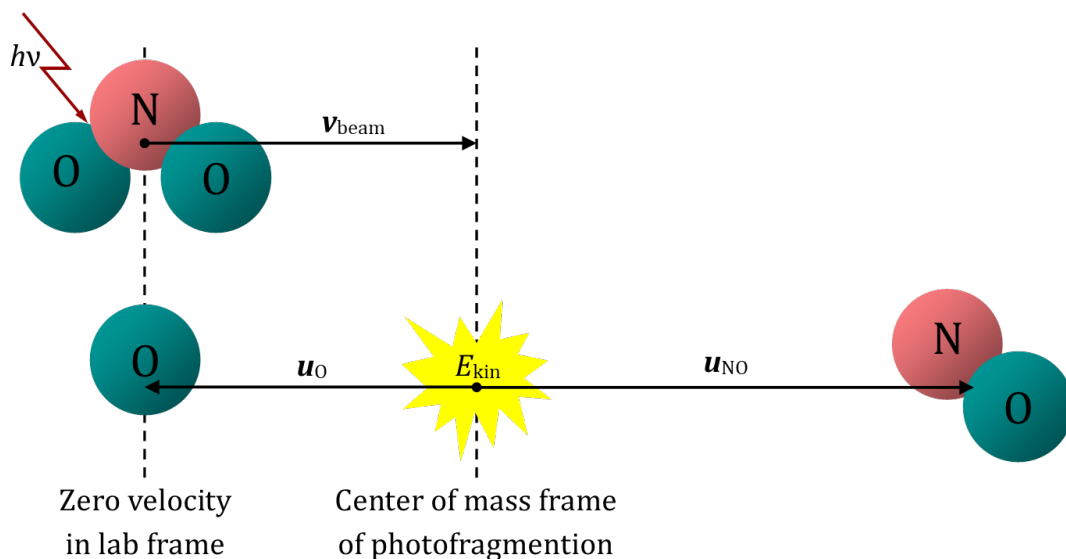
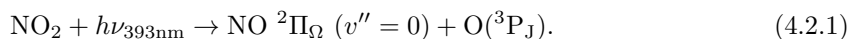


Figure 4.1: Schematic of photostop of atomic oxygen from  $\text{NO}_2$ .

## 4.2 Velocity map imaging of oxygen photostop

Velocity map imaging (VMI) is a ubiquitous technique for revealing, in exquisite detail, the nature of gas-phase chemical and photo-chemical reactions.<sup>71</sup> It has been described and reviewed previously and used in highly cited publications.<sup>72,73</sup> The technique relies on a specific electric potential-energy landscape in the experiments ionisation region that guides ions to a detector position that is specific to their velocity and not their position.

VMI was used here to gain insight into the state distribution and anisotropy<sup>74</sup> of the  $\text{NO}_2$  photodissociation to produce atomic oxygen by,



The  $J$  state distribution of the atomic oxygen<sup>75</sup> was largely wavelength independent and well known and so was not measured. The distribution of the NO co-fragment rotational states was studied as it contained information to determine the most efficient photostop conditions. The NO rotational distribution and anisotropy from photodissociation was studied both directly, by NO VMI, and by-proxy by VMI of the  $^3\text{P}_2$  oxygen co-fragment at a range of relevant photodissociation wavelengths.

Molecular beam speeds ranging from 500 to 364 m/s were measured and the appropriate range of photodissociation wavelengths to be used according to eqn. (2.1.1) were determined for the range of molecular beam speeds.

The properties of the molecular beam of trace  $\text{NO}_2$  in xenon or argon were also studied and a series of images showing successful photostop conditions for atomic oxygen at typical molecular beam speeds were taken. A calibration curve relating photodissociation wavelength to the ideal photostop molecular beam velocity was also produced.

### 4.2.1 Experimental

This experiment and the experiments described in chapter 5 were performed in a VMI capable instrument. Much of the experimental detail was unchanged between the two chapters and so will only be described here.

#### Vacuum systems and molecular beam source

This experiment was performed in a high vacuum chamber originally built to study the reactive scattering of hydrogen Rydberg atoms.<sup>76</sup>

The apparatus contained a source chamber that contained the molecular-beam source (Parker, General valve Series 9, 200  $\mu$ s opening time, 0.5 mm nozzle.) The molecular-beam gas sample was made by mixing 10-300 mBar of NO<sub>2</sub> with up to 4 Bar of xenon gas. This gave a backing pressure of 3.4 Bar for the supersonic expansion. The molecular beam operated at 10 Hz in sequence with the rest of the apparatus. The molecular beam was kept central by a series of mounting spikes. This chamber was connected to the photostop chamber by a skimmer (1 mm, Model 1, Beam Dynamics), that provided differential pumping and so reduced background gas in the ion-optics stack. The photostop chamber contained the ion-optics stack used for VMI measurements and also optical access for counter-propagating lasers through ports with built in alignment irises. The laser axis was perpendicular to both the ion optics and molecular beam axes that were also perpendicular to each other.

The ion-optics stack guided ions into the detection region of the chamber. This contained the MCP stack, phosphorous screen and charge-coupled device (CCD) camera array (Photek, VID240), that allowed position and time-sensitive charged-particle detection in combination with their power supply units (VID BPS3 and Ion Slicer BPS5). The detector gave an output to an oscilloscope (Lecroy, Waverunner, LT584 DSO, 1 GHz, 4 GS/s) that was used to measure ion time-of-flights and another output to the laboratory computer which recorded position-sensitive ion-detection for VMI in specialist Photek designed software. The chamber was evacuated by three turbo-molecular vacuum pumps, (Pfeiffer HiPace 2300 C 1900 l/s, Leybold Trivac D40B 25 m<sup>3</sup>/h and Leybold Turbovac 151C 145 l/s) that were in turn supported by a single side-channel backing pump (Pfeiffer, TCP 2000). The chamber had several large O-ring seals and so had a base pressure of approximately  $3 \times 10^{-7}$  mBar in the source region and  $4 \times 10^{-8}$  mBar in the photostop region, both pressures were measured by Bayer-Alpert ion gauges.

#### Molecular dynamics and photostop losses

Photostop occurred by photodissociating NO<sub>2</sub> molecules according to eqn. (4.2.1) such that O <sup>3</sup>P<sub>2</sub> atoms were created at rest by opposing the velocity of the NO<sub>2</sub> in the molecular beam according to eqn. (2.1.1). Unlike previous work on SH in chapter 2, the photodissociation produces approximately 55 % of O atoms in the desired <sup>3</sup>P<sub>2</sub> state and the rest in <sup>3</sup>P<sub>1</sub> and <sup>3</sup>P<sub>0</sub> states. This leads

to a large increase in the proportion of photostopped species from the photodissociation relative to SH. The width of the molecular beam velocity distribution and small energy spacing between NO co-fragment rotational energy levels allows photostop of O  $^3P_2$  from multiple co-fragment rotational states. The higher magnetic moment of O  $^3P_2$  atoms allows a 0.41 T deep magnetic trap to confine atoms moving up to 30 m/s.

Whereas SH photostop was relatively far in energy from the photodissociation threshold to exploit favourable absorption cross-sections, O  $^3P_2$  photostop can be done close to the threshold, this allows use of a slower moving molecular beam which also increases the number of photostopped atoms. These differences total to an estimated 50 times increase in density of O from photostop relative to SH if the O photostop is done with a beam of NO<sub>2</sub> in xenon.

The NO<sub>2</sub> photodissociation process is not simple. The most comprehensive study of the process was completed<sup>74</sup> by Matthews *et al.* (and references within) which is the best source for a more in depth discussion of the process. Given here is a brief summary of the relevant information.

The near-threshold photodissociation of NO<sub>2</sub> is most simply described as a process at a point between that of a statistically unbiased dissociation and a dynamical one. The anisotropy parameter varies significantly across only a few wavenumbers of dissociation energy as well as between different NO rotational states. Previous work<sup>74</sup> has outlined the important parameters that influence the anisotropy as being: the angle between the transition-dipole-moment and the recoil-vector, the lifetime of the dissociating state, the tipping angle caused by rotation of the fragments during dissociation and the available rotational energy of the dissociating species. A hypothesis<sup>74</sup> can broadly describe the dissociation process but does not come close to predicting the large fluctuations in anisotropy and rotational state distribution with small excess energy changes.

The dissociation occurs by rapid mixing to the X ( $^2A_1$ ) state, after initial A ( $^2B_2$ ) state excitation, in around 100 fs. The fragmentation itself then occurs on the ground state surface vibrational continuum in a few picoseconds.

In many ways the details of the photodissociation are not important for this experiment. Simply, one or a few wavelengths must be found that gives a relatively anisotropic dissociation and produces O  $^3P_2$  at a velocity close to that of the molecular beam. The exact rotational distribution of NO and anisotropy parameter of the photodissociation do not need to be known to successfully trap atomic oxygen.

### Laser systems

This experiment made use of a dissociation laser for photostop and a probe laser for resonance-enhanced multiphoton-ionisation (REMPI) as shown in fig. (4.2).

The dissociation light was from a dye laser (Lambda-Physik FL2002, with Sirah dye cell retrofitting, 0.1 g/l Exalite 389 and 0.1 g/l Exalite 398 in para-dioxane) pumped by the 355 nm third harmonic of a Nd:YAG solid-state laser (Continuum Powerlite, Precision II, 10 Hz) and

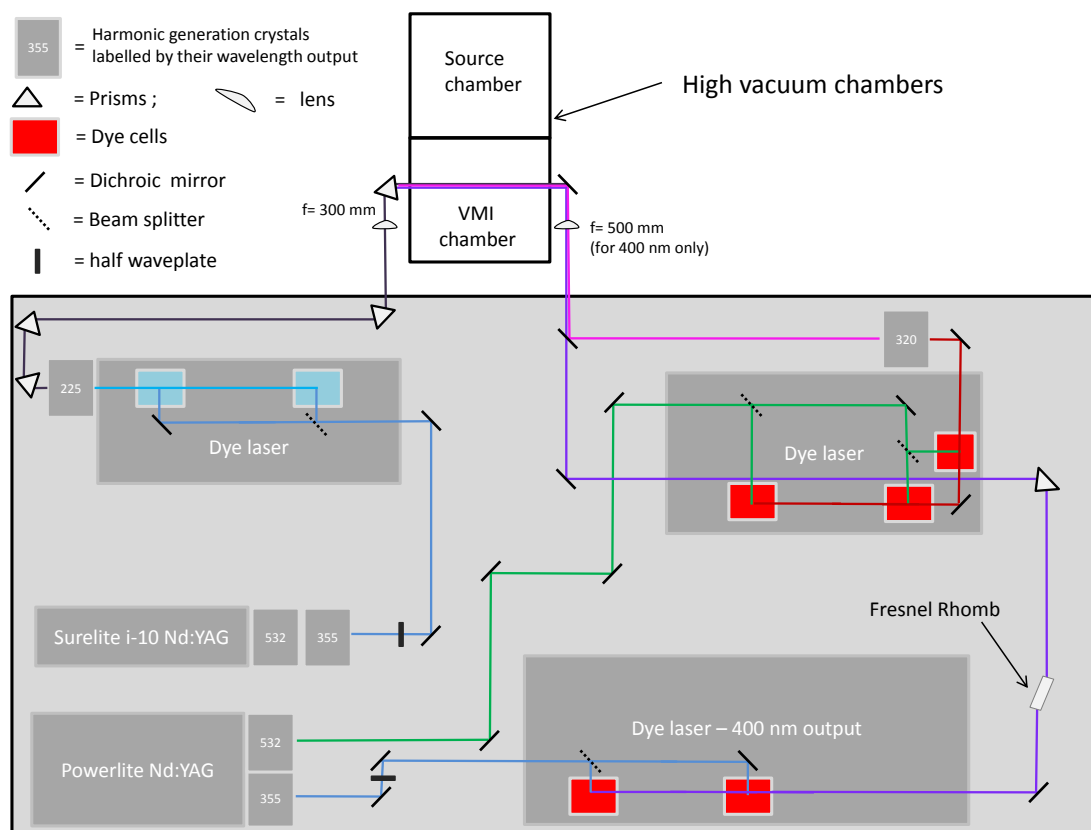


Figure 4.2: Birds-eye schematic view of optical setup for the O VMI photostop experiment, key is shown in figure. The Dye laser components have been simplified as has the experiment chamber and schematic is not strictly to scale. (Note that although the 323 nm laser was not used for this experiment but instead for the NO clusters work in chapter 5, it was present on the table at the time.)

produced 5 mJ/pulse of 390-400 nm light.

The light was directed into the experiment region of the vacuum chamber by dichroic mirrors and had its polarisation turned to be parallel to the molecular beam axis by a Fresnel-Rhomb polariser. As the photodissociation process occurred parallel to the polarisation plane of the dissociating light, due to typical  $\beta$  values of 1.5, this was necessary to counter-align the molecular beam and recoil-fragment velocity vectors. The light was focused onto the molecular beam axis by a  $f = 500$  mm lens set 400 mm from the molecular beam intersection.

The probe light was from a dye laser (Sirah Cobra-stretch, Coumarin 2 (450) 0.2 g/l in methanol) pumped by the 355 nm third harmonic of a Nd:YAG solid-state laser (Continuum Surelite, i10, 10 Hz) that produced 3 mJ/pulse of 450 nm light. This light was passed through a BBO crystal that doubled the wavelength to 225 nm light at 0.2 mJ/pulse. This light was separated from the fundamental by four Pellin-Broca prisms and then guided to counter-propagate against the dissociation laser by four more prisms (UV-fused silica). The light was focused onto the molecular beam axis by the shortest possible focal length lens ( $f = 300$  mm) to achieve the

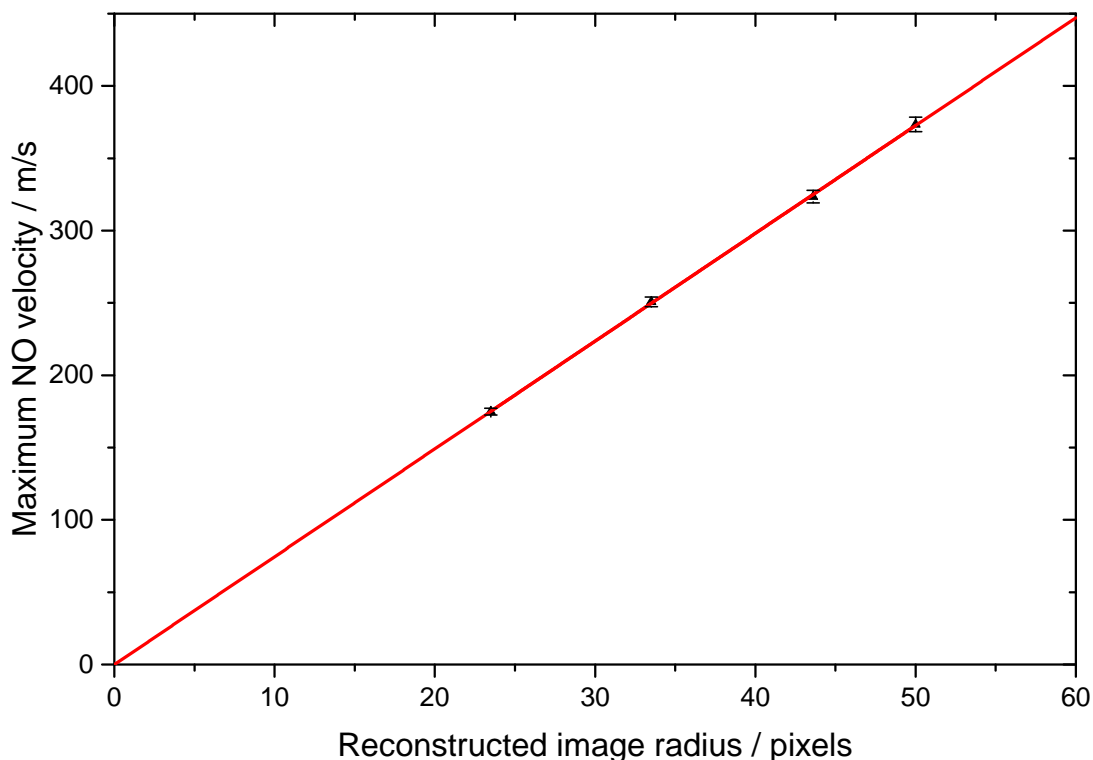


Figure 4.3: Pixel to velocity calibration curve giving a gradient of  $7.45 \pm 0.10$  m/s/pixel or  $1.99 \pm 0.02$  J<sup>1/2</sup>/pixel if  $\sqrt{E_{\text{kinetic}}}$  is plotted instead. Radii are the centre of a Gaussian fitted to the radius profile of reconstructed NO  $^2\Pi_{3/2}$   $\Omega = 1.5$  images (reconstructed using image program inverse Abel reconstruction) and velocities are found by converting from dissociation laser wavelengths measured with a wavemeter.

necessary photon flux for (2+1) REMPI. This particular lens focal length was previously used by other O (2+1) REMPI studies.

The lasers position in space was optimised by the irises on the vacuum chamber windows (MgF<sub>2</sub>) and then by the (2+1) O REMPI signal. The lasers were temporally overlapped by measurement using a fast response photo-diode detector (ET-2000, Electro-Optics Technology) and tape measure and adjustment by a pulse generator box that sequenced the timings of the entire experiment (BNC, 575 pulse/delay generator).

## 4.2.2 Results and discussion

### Pixel to velocity calibration

Although velocity map imaging (VMI) can be used to measure particle velocities, a particular ion optics setup must be carefully calibrated so that the relationship between pixel position, on the detector, and velocity is known.

By measuring the radius of photodissociation images taken at known dissociation wavelengths

and with literature knowledge of the threshold photodissociation energy and molecular internal energy levels, this calibration can be achieved as in fig. (4.3).

Calibration using four velocity-map-images (reconstructed using inverse Abel) of NO  $^2\Pi_{3/2}$   $\Omega = 1.5$ , where  $\Omega$  is the total angular momentum quantum number, from photodissociation of NO<sub>2</sub> at 394.4, 392.6, 390.3 and 388.4 nm found a pixel to velocity relationship of  $7.45 \pm 0.1$  m/s/pixel or  $1.99 \pm 0.02$  J<sup>1/2</sup>/pixel if  $\sqrt{E_{\text{kinetic}}}$  is considered instead. The sum of dissociation energy and NO fragment internal energy found from the calibration also agreed with literature within error. This relationship was used in all future VMI work in this thesis.

### Xenon molecular beam speed measurements

(1+1) REMPI of trace NO in a molecular beam of 6.5 % NO<sub>2</sub> in Xenon at 3.4 Bar backing pressure combined with VMI gave a measurement of the beams velocity profile as shown in fig. (4.4). It was assumed that the NO in the beam moved at the same velocity as other species in the beam.

The beam was found to be travelling at  $364 \pm 47$  m/s with a perpendicular velocity spread of 36 m/s. This was close to the expected velocity based on simple molecular beam thermodynamics calculations with an estimated valve temperature of 305 K. This velocity increased by tens of m/s on consecutive days of measurement as did the width of the velocity distribution. This could have been due to a gradually decreasing backing pressure through small leaks or a photo-chemical decay of the photosensitive NO<sub>2</sub>. This was taken into account for future trapping measurements in which gas mixes were used for only one days measurements to avoid any potential sample decay problems.

### NO<sub>2</sub> photodissociation spectrum

With a dissociation wavelength of 393.923 nm, a spectrum of  $^2\Pi_{1/2}$  NO was taken by scanning a second REMPI laser from 226.3 to 225 nm, as shown in fig. (4.5). The trace NO<sub>2</sub> in xenon molecular beam source contained a small amount of NO in the beam before photodissociation. The measured rotational state populations are a combination of the contribution from NO in the beam source and NO from the photodissociation of NO<sub>2</sub>. The peak positions were assigned from literature.

The highest quantum state measured was  $\Omega = 12.5$ , this state was energetically inaccessible from dissociation of ground state NO<sub>2</sub> but was produced from the dissociation of NO<sub>2</sub> with a small amount of internal energy. Because the  $\Omega = 13.5$  state did not appear it is reasonable to suggest that the NO<sub>2</sub> molecules have up to  $69 \text{ cm}^{-1}$  of internal energy before photodissociation. Some NO<sub>2</sub> molecules may have had internal energy above this mark but either do not dissociate to produce NO in states above  $\Omega = 12.5$  or do not do so frequently enough to be detected.

The  $\Omega = 7.5$  and  $\Omega = 8.5$  rotational states were the most highly populated, this was consistent with photostop measurements made later on but does not follow a normal statistical distribution. Previous work<sup>74</sup> by Matthews *et al.* (discussed earlier) showed that the photodissociation pro-

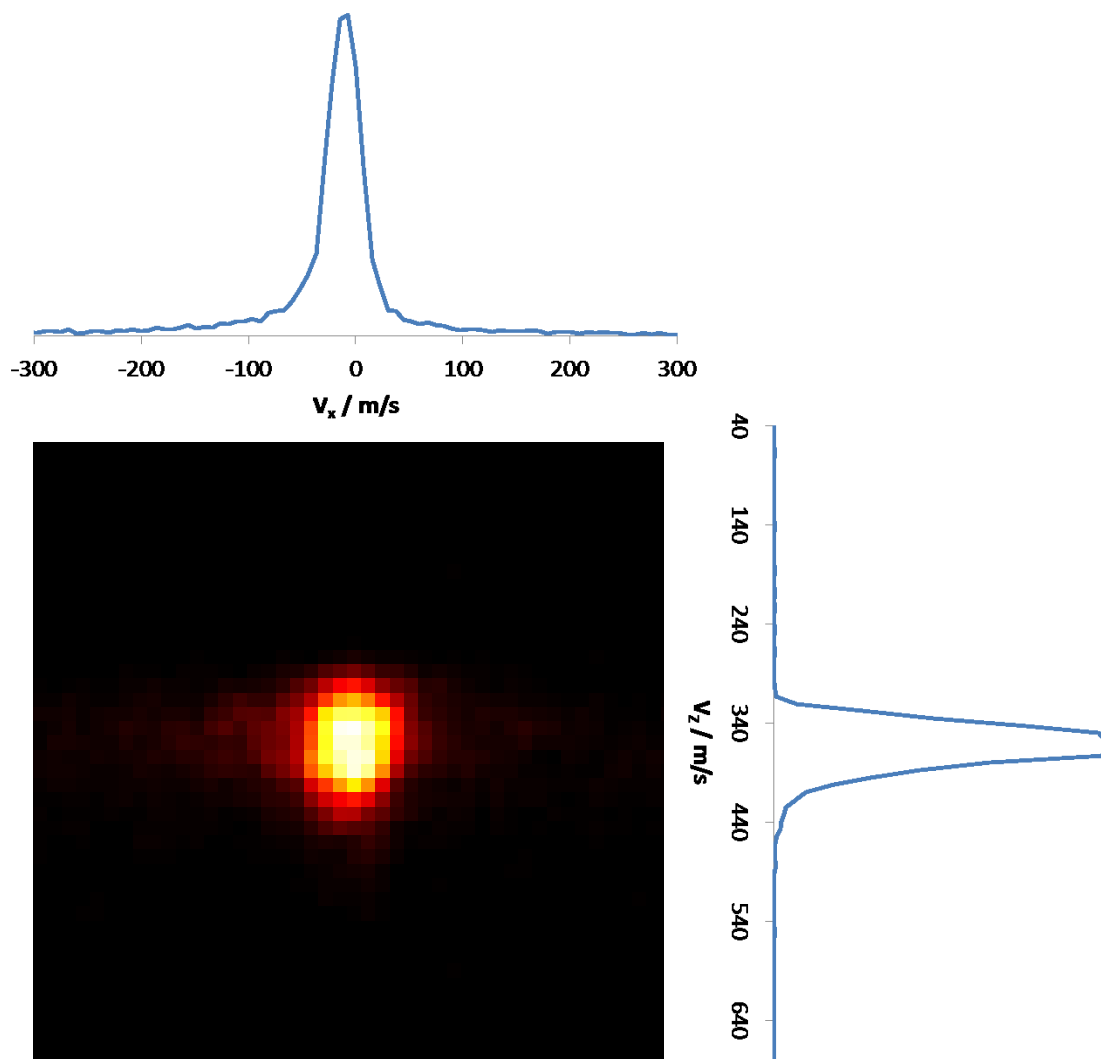


Figure 4.4: 6.5 %  $\text{NO}_2$  in Xenon at 3.4 Bar backing pressure molecular beam VMI image with corresponding intensity profiles. Image taken with single (1+1) REMPI laser at 226.142 nm to probe the NO impurities in the beam (that are in thermal velocity equilibrium with  $\text{NO}_2$  but easier to probe.) The beam is travelling at 364 m/s with a FWHM of 47 m/s in the molecular beam axis (z) and FWHM of 36 m/s in the probe laser axis (x), this is significantly slower and narrower than a comparable beam in argon carrier gas.



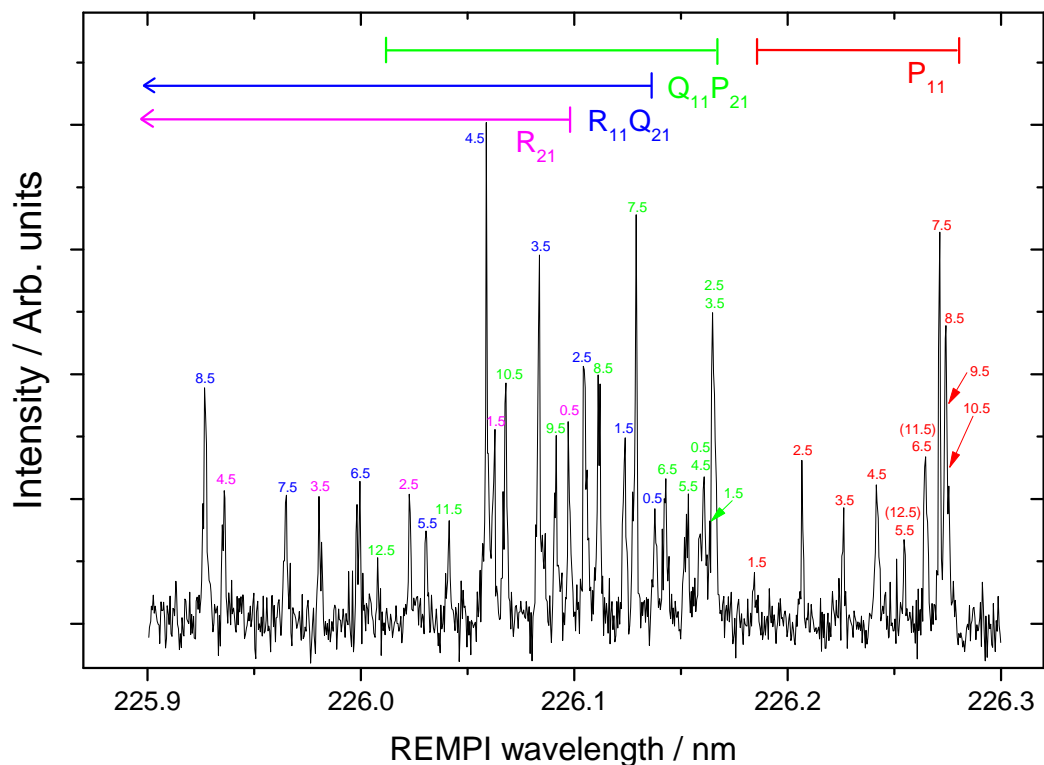


Figure 4.5:  $\text{NO } ^2\Pi_{1/2}$  photodissociation (1+1) REMPI spectrum from trace  $\text{NO}_2$  in a Xenon molecular beam using a fixed wavelength 393.923 nm photodissociation laser and scanned REMPI laser. Labels indicate the transition band and inter-nuclear axis projection quantum number. Peak intensity patterns are a non-trivial convolution of the photodissociation products and nascent NO impurities in the molecular beam.

cess produces non-statistical rotational distributions that are highly wavelength dependent. This spectrum may be significantly different at a nearby dissociation wavelength, for example 394 nm.

### $^3\text{P}_2$ oxygen photostop

The principle purpose of this experiment was to find ideal conditions for  $\text{O } ^3\text{P}_2$  photostop and to measure a sequence of velocity map images that showed the production of near stationary atoms.

A wavelength of 393.9234 nm gave a promising anisotropy parameter of  $\beta = 1.3$  and a radius profile in fig. (4.6) that peaked at 350 m/s recoil velocity. Although this was slightly lower than the measured 364 m/s molecular beam, a slightly higher backing pressure (4 Bar) was expected to slightly reduce the beam speed to approximately 350 m/s. This wavelength was used to demonstrate the photostop process for  $\text{O } ^3\text{P}_2$  as shown in fig. (4.7). The figure shows that as the time between photostop and ionisation increased, the faster moving atoms left the probing volume until only atoms moving below 30 m/s were remaining 1900 ns after photostop. This speed was measured by VMI and was also consistent with the expected remaining speeds based on the size of the probing volume and the speeds of the atoms.

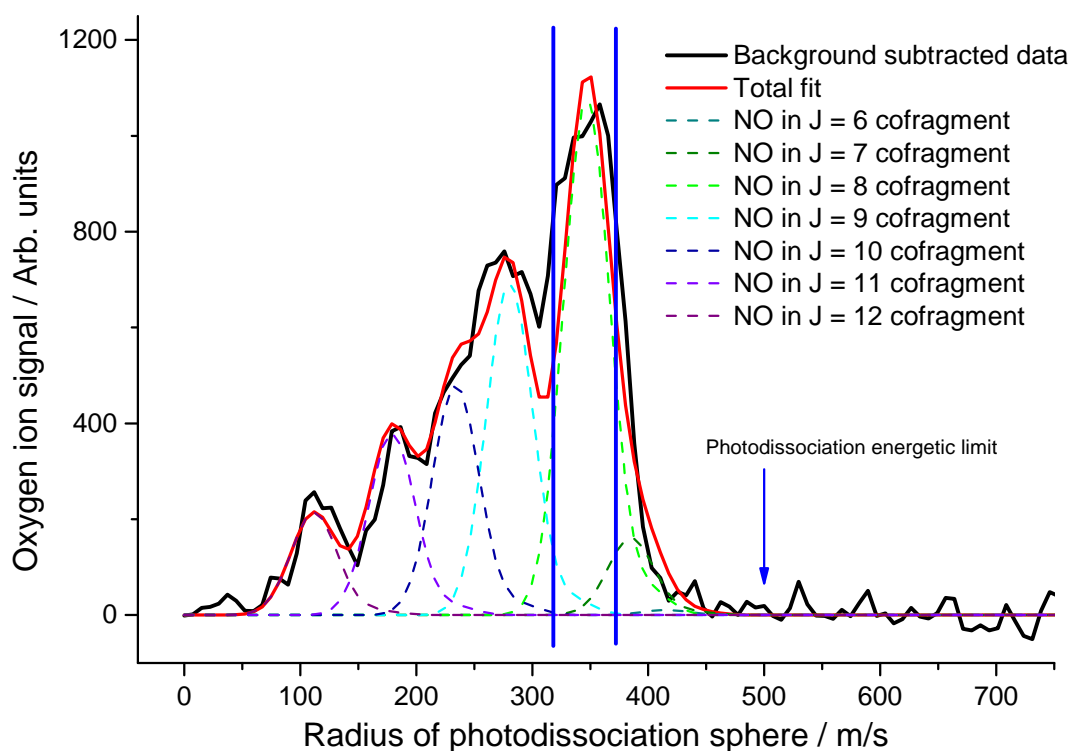


Figure 4.6:  $\text{O } ^3\text{P}_2$  photodissociation radius profile at 393.9234 nm. Blue lines represent the potential velocity range that could be confined by the magnetic trap described in chapter 2. The fit is made up of contributions from all energetically accessible NO photodissociation co-fragments with widths defined by the measured molecular beam velocity spread in Fig. (4.4). Note that the  $J = 12$  ( $\Omega = 12.5$ ) NO fragment was energetically forbidden unless from a photodissociation of an  $\text{NO}_2$  molecule with non-zero internal energy.

Fig. (4.8) shows a radius profile for another potential photostop wavelength, the distribution and anisotropy ( $\beta = 1.3$ ) were broadly similar to that measured at 393.92 nm but the ideal photostop wavelength was slightly higher at 364 m/s.

Fig. (4.9) shows velocity map images (reconstructed Inverse Abel transformations) of the NO co-fragments produced from photostop. The  $\Omega = 8.5$  and 7.5 images have the greatest anisotropy of  $\beta = 1.3$  and 1.4 respectively and are also the rotational states that will produce photostopped  $\text{O } ^3\text{P}_2$ .

### Photostop calibration curves

Photodissociation radius profiles were taken for seven different dissociation wavelengths. The maximum ion signal of these profiles was found and the velocity at which this occurred was taken to be the correct molecular beam velocity for photostop at the given wavelength. The results shown in fig. (4.10) show an approximately linear relationship between wavelength and ideal molecular beam velocity.

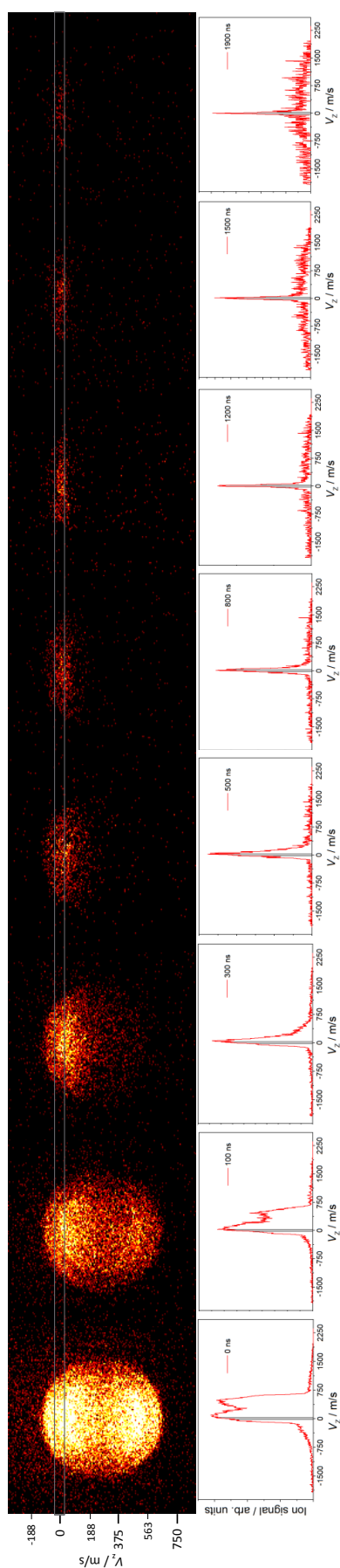


Figure 4.7: Above: Velocity map images (crushed spheres) of  $^3\text{P}_2$  oxygen atoms from dissociation of  $\text{NO}_2$  by a 393.702 nm laser with increasing delay between said dissociation laser and a 225.56 nm REMPI probe laser. Below: graphs of the intensity profiles of the corresponding above images along with laser time delay labels. Grey tram lines and shaded areas correspond to the atoms that have been sufficiently slowed for magnetic trapping. At 1900 ns, the remaining O  $^3\text{P}_2$  atoms in the probe volume move below approximately 30 m/s according to the probe geometry, this is consistent with the VMI velocity measurement. The number of laser shots is not consistent between VMI images and 'ion signal' magnitude should not be compared as it is not normalised.

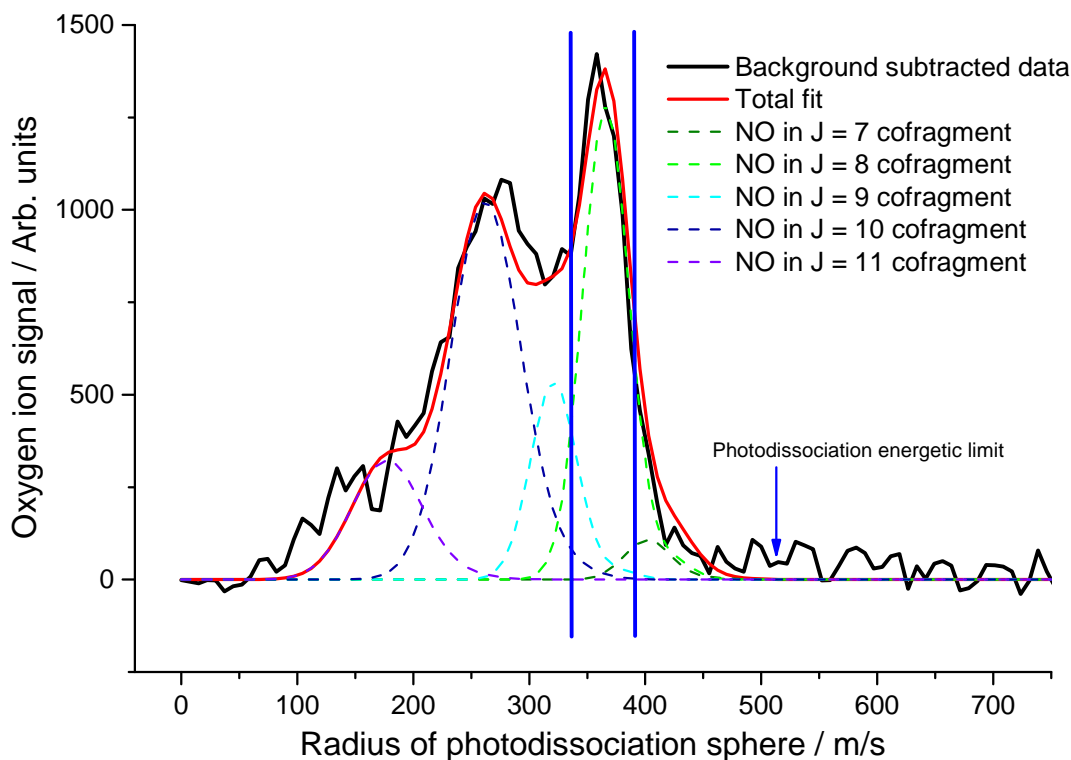


Figure 4.8:  $\text{O}^3\text{P}_2$  photodissociation radius profile at 393.702 nm. Blue lines represent the potential velocity range that could be confined by our magnetic trap. The fit is made up of fitted contributions from all energetically accessible NO photodissociation co-fragments with widths defined by the measured molecular beam velocity spread in Fig. (4.4).

This curve can be used to find the ideal photostop wavelength after a molecular beam velocity has been measured. Although a linear trend appears to be present, there is no robust physical reason for this, the most populated rotational state of the NO co-fragment varies with wavelength and so often the ideal wavelength is not found so trivially. A molecular beam usually has at least a 10 % FWHM velocity spread and so getting the dissociation wavelength to exactly match the beam speed is not crucial. A far more important property of a photodissociation is the anisotropy and so to maximise the number of photostopped atoms, a wavelength with a high anisotropy should be chosen even at the cost of a slightly mismatched velocity. The highest anisotropy parameter measured was  $\beta = 1.3$  at a dissociation wavelength of 393.9234 nm and 393.702 nm.

### 4.2.3 Conclusions

By using VMI technique, photostop of  $\text{NO}_2$  was shown to produce near stationary  $\text{O}^3\text{P}_2$  atoms in free space. The trace  $\text{NO}_2$  in xenon molecular beam speed and position distributions were studied and will inform both simulations and trapping experiments. Photostop was performed at a number of wavelengths relevant to the expected molecular beam velocities to produce an advisory calibration curve.

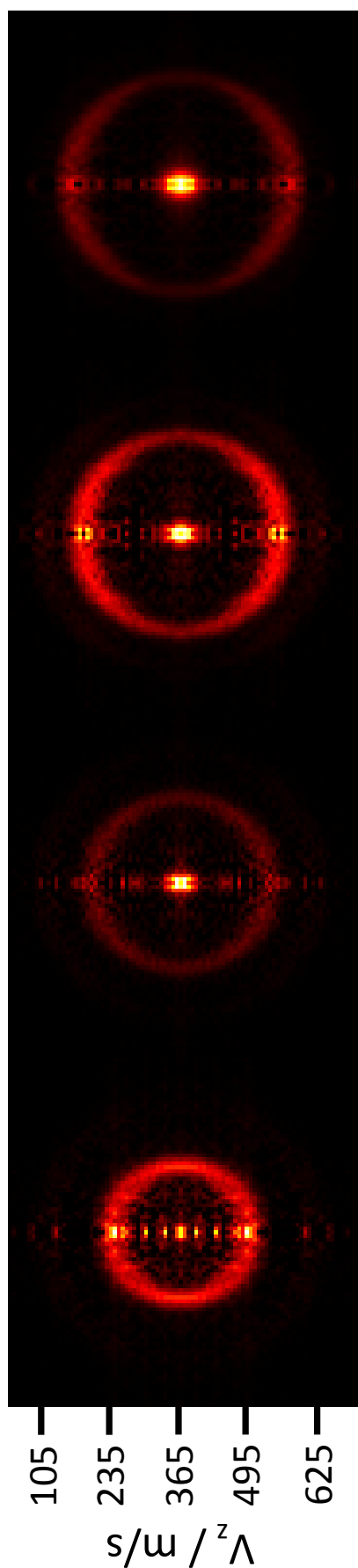


Figure 4.9: Velocity map images (reconstructed Inverse Abel transformations) of NO  $^2\Pi_{1/2} \Omega = 10.5$  to  $7.5$  (bottom to top) produced from photodissociation of trace NO<sub>2</sub> in a xenon molecular beam used to determine photodissociation anisotropy. Images are all taken with a 393.9324 nm dissociation wavelength. Images have an inner spot corresponding to NO impurities in the molecular beam, an intense ring corresponding to the quoted  $\Omega$  value and all but the  $\Omega = 7.5$  image have additional weaker rings from energetically close peaks corresponding to other NO  $^2\Pi_{1/2} \Omega = ?$  rings.

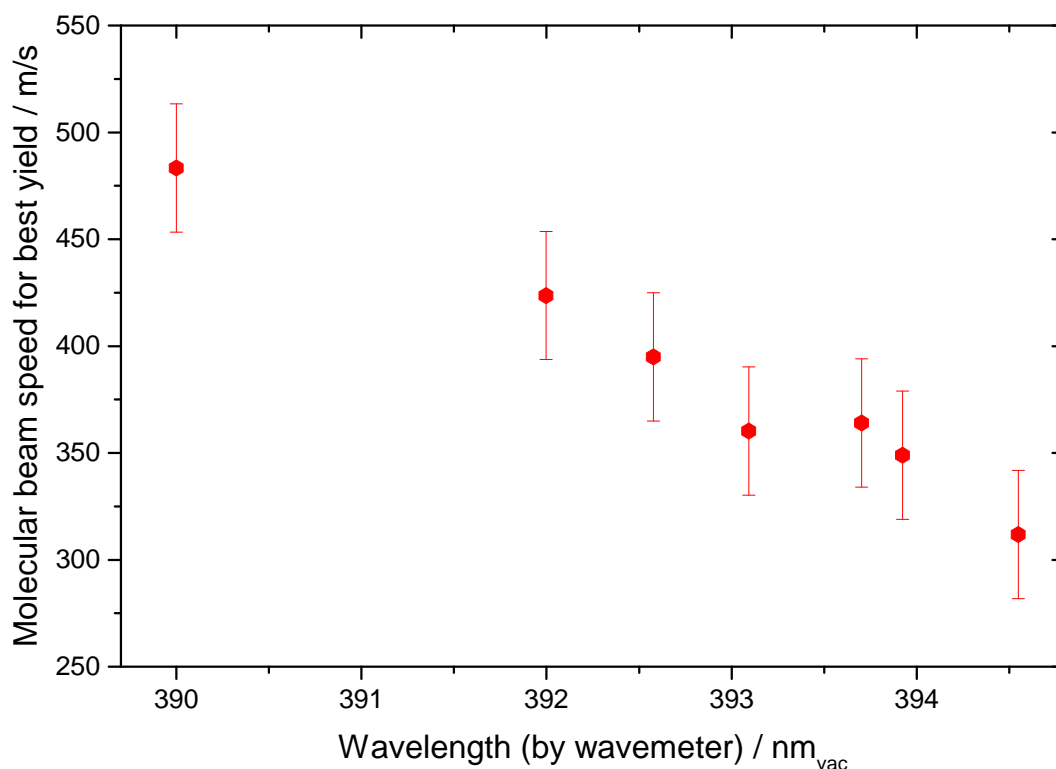


Figure 4.10: Calibration curve relating photodissociation wavelength of  $\text{NO}_2$  to the molecular beam speed required for the highest yield of photo-stopped  $\text{O } ^3\text{P}_2$ . The red bars represent the range of velocities that the magnetic trap will accept and are not error bars. Although a linear trend appears to be present, there is no rigorous physical reason for this and so extrapolation should be done cautiously.

The information learned from this experiment was used in the magnetic trapping experiment to produce and study trapped  $\text{O } ^3\text{P}_2$  atoms in a confining field.

### 4.3 Magnetically trapped oxygen atoms

A lot of the experimental descriptions for this section are identical to that described in the first half of this chapter. Thus the photodissociation dynamics, photostop losses and laser alignment procedures are only given in the early parts of chapter 4. Additionally, as this experiment was carried out in the same chamber as the SH trapping experiments in chapter 2, the description of the vacuum system and molecular beam source is almost identical and so will only be briefly discussed here. The magnetic trap and ion optics are identical to those in chapter 2 and so will be omitted from this section.

### 4.3.1 Experimental

An advantage of studying atomic oxygen is that an absolute measurement of the molecular density can be made using REMPI that was not possible with SH. Section B.1 in Appendix B contains a derivation of the method to find absolute densities from the oxygen REMPI measurements. The absolute atomic density of oxygen in the magnetic trap was determined using the method described by D. J. Bamford *et al.*<sup>77</sup> This was done with knowledge of the probe lasers spatial and temporal profile, the MCP detection efficiency, the laser power and the (2+1) REMPI processes' cross sections and excited state decay rates.

#### Vacuum systems and molecular beam

The vacuum pumps and their positions in this section were identical to that in chapter 2. With the cryostat running, the chambers base pressure was  $7 \times 10^{-10}$  mbar (Bayard-Alpert gauge) and  $10^{-6}$  mbar with the molecular beam firing at 5 Hz. The instrument contained a skimmed (2 mm, beam dynamics) supersonic molecular beam of 6 % NO<sub>2</sub> in 4 Bar of krypton or xenon that was produced by a solenoid valve (Parker, General Valve, Series 9) pulsed at 5 Hz. The valve sat inside the source arm of a single vacuum chamber. This arm was partially separated by a plate, with the skimmer mounted to it, which guided the majority of the unskimmed beam towards pumping surfaces, just as in chapter 2.

#### Laser systems

Similar to the VMI O photostop experiments detailed earlier in this chapter, two lasers were used at approximately 225 nm and 390-400 nm for REMPI and dissociation respectively. Initially both lasers were formed identically to in the O VMI experiment with the exception of using a Continuum Surelite i10 pump laser and Sirah Cobra-stretch dye laser to form the 390 - 400 nm light using the same laser dyes and pump wavelengths as before. The 225 nm laser was made in an identical fashion to the O VMI experiments and focused in the same way.

It was found that the 390-400 nm light generated was consistently below 1 mJ/pulse which was lower than expected, additionally the cost of the Exalite 389 and Exalite 398 dyes in dioxane was preventative and the dyes working lifetime was only two weeks. To create greater laser power at a lower cost and with greater stability, the 390-400 nm laser was made using a different method. The second harmonic of a Nd:YAG solid-state laser at 532 nm (Continuum Surelite, i10) was used to pump a dye laser (Sirah, Cobra-stretch, 0.2 g/litre DCM in ethanol) to produce 630 nm light. This light was sum-frequency-mixed (SFM) with the residual 1064 nm light from the pump laser fundamental in a KDP type-2 crystal. This created up to 3 mJ/pulse of 391 nm light with much greater dye lifetimes, the optical layout is shown in fig. (4.12). The light was telescoped to give a  $e^{-2}$  radius of 1 mm by 0.3 mm and had polarisation parallel to the molecular beam.

Similarly to previous photostop trapping experiments, the probe light was capable of photodis-

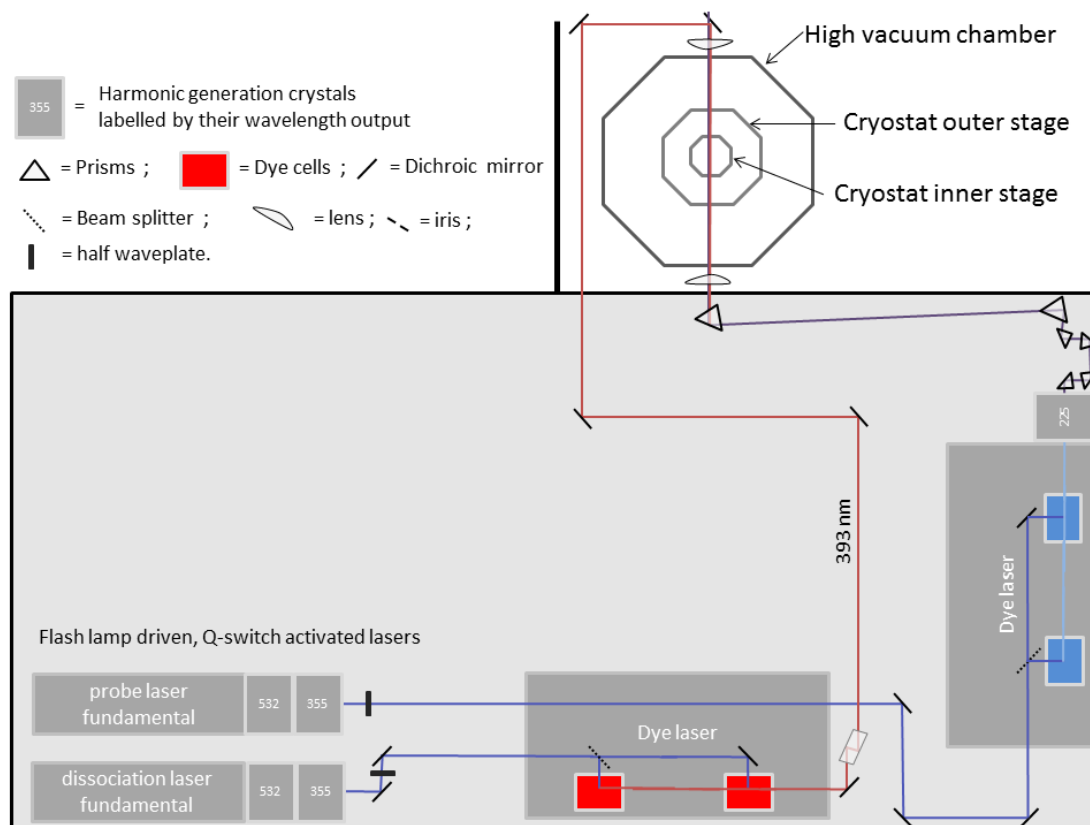


Figure 4.11: Birds-eye schematic view of the first optical setup for the O photostop and trapping experiment, key is shown in figure. The Dye laser components have been simplified as has the experiment chamber and schematic is not strictly to scale.

sociating  $\text{NO}_2$  at 225.65 nm. This created a significant background signal whereby 4 probe laser photons would dissociate  $\text{NO}_2$  and ionise the resulting O. This was accounted for by subtracting data from measurements taken with the dissociation laser blocked by

$$S_{\text{bgsub}} = S_{\text{tot}} - S_{\text{bg}}. \quad (4.3.1)$$

Whereas in chapter 2, a shot-to-shot background subtraction was used, in this section 1000 measurements with the dissociation laser on were taken followed by 1000 with the laser off. This small change was made to allow for any potential density accumulation between multiple photostop events to occur. The power of the probing laser was stable enough with time that this did not vary significantly from signal to background measurements and thus did not corrupt the background subtraction.

### Redesign of the cryopump

Initial attempts to observe magnetically trapped atomic oxygen saw a gradual decrease in ion arrival rate with time. This was measured and attributed to xenon ice forming on the cryostat that blocked passage of either the molecular beam or ions or both. By running the experiment for



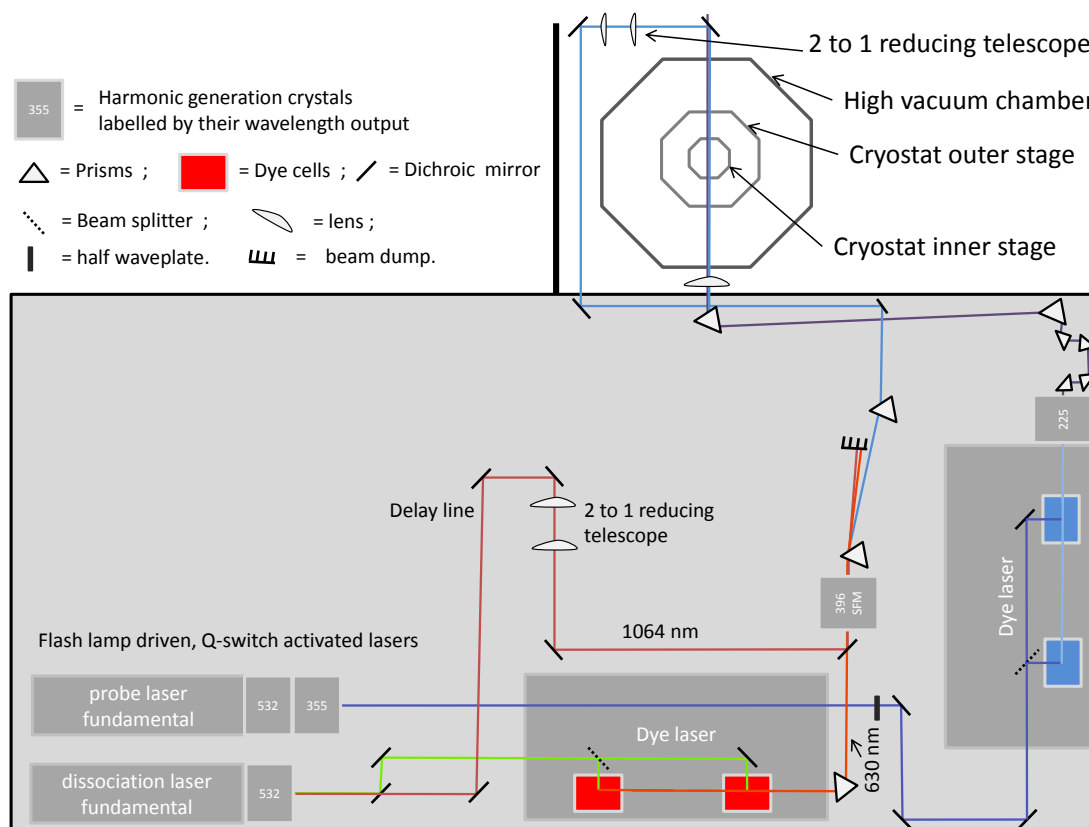


Figure 4.12: Birds-eye schematic view of the improved optical setup for the O photostop and trapping experiment with the SFM setup, key is shown in figure. The Dye laser components have been simplified as has the experiment chamber and schematic is not strictly to scale.

10000 shots and recording data in 1000 shot intervals, then unloading the cryostat by warming it and retaking data, it was clear that the xenon ice was causing the lowering of the ion arrival rate.

A new component was designed, as shown in fig. (4.13), to prevent the magnetic trap from being cooled by the cryostat head. This worked simply by replacing the copper stem with a solid piece of Macor ceramic glass, the piece conducted heat 400 times slower than the copper thus preventing the trap from being cooled effectively. This raised the temperature of the magnetic trap with the cryostat on from 30 K to 150 K.

Although the new part slowed the rate at which the ion arrival rate decreased, as seen in fig. (4.13), it did not solve the problem. Only by using krypton as the carrier gas was the problem reduced significantly at a cost of 65 % signal intensity from a larger newtons sphere during the photostop process.

### 4.3.2 Results and discussion

In the magnetic trap, the absolute number of O atoms inside the probe volume was followed at delay times from 12 to 79 ms after photodissociation as in fig. (4.14). The error after background

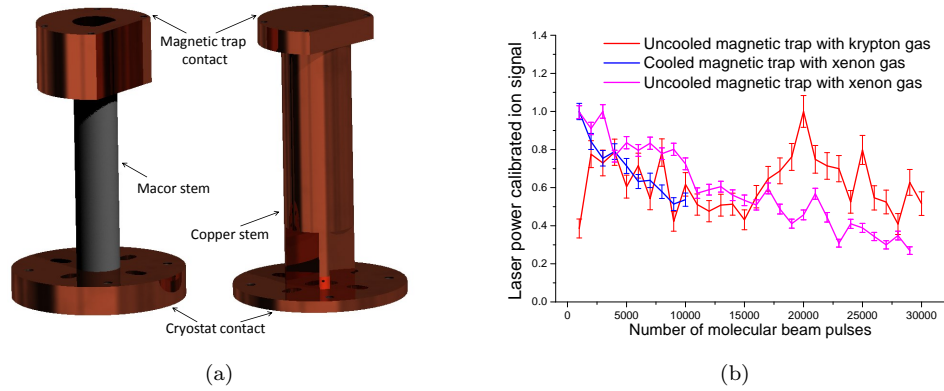


Figure 4.13: (a) Previous and new model for the magnetic trap mount onto the cryostat. The introduction of a non-conductive Macor stem prevents the Cryostat from effectively cooling the magnetic trap. (b) Testing of the new part showed that although xenon icing occurred at a slower rate the problem remained, only with a krypton beam was the problem minimised.

subtraction was found using Poisson statistics by

$$\delta S_{\text{REMPI}}^{\text{backsub}} = S_{\text{REMPI}}^{\text{backsub}} \sqrt{\left(\frac{1}{\sqrt{N_{\text{signal}}}}\right)^2 + \left(\frac{\sqrt{N_{\text{background}}}}{N_{\text{signal}}}\right)^2}, \quad (4.3.2)$$

in which  $N_{\text{signal}}$  and  $N_{\text{background}}$  are the number of events from atomic oxygen and any other background sources respectively.

The trapping measurements were made with a molecular beam containing krypton instead of xenon, this resulted in a 65 % drop in photostop efficiency from the greater beam speed. Krypton has a lower freezing point and so did not significantly freeze onto the surface of the magnetic trap housing thus allowing the long measurements needed to confirm magnetic trapping. This change in carrier gas from imaging to trapping experiments was accompanied with a decrease in photodissociation wavelength to compensate for the increasing beam speed,  $v_{\text{beam}}$ . Unfortunately this meant the highest  $\beta$  anisotropy parameters measured around 393 nm could not be used and likely resulted in a lower trapped atomic oxygen density.

By using a beam of  $\text{NO}_2$  in krypton, trapped atomic oxygen atoms were measured to have a trapped lifetime of  $82 \pm 3$  ms with a maximum density in the probing volume of  $3000 \pm 900 \text{ cm}^{-3}$ . The trap lifetime was found by putting a weighted least-squares best-fit line through the data with its given errors and these errors were propagated to give errors in the trap lifetime and maximum density.

Measurements were also made at zero photostop delay, with the dissociation laser arriving 1 ns before the probe laser. This was done to find the efficiency of the photostop process, what portion of dissociated molecules create trappable atomic oxygen, it was found that at zero delay,  $4.6 \pm 0.1 \times 10^6 \text{ cm}^{-3}$  atoms were produced. This gives a photostop efficiency of  $6.6 \times 10^{-4}$  which is 40 times higher than the efficiency predicted from the simulation used in chapter 2 with its parameters changed to match this experiment. This surprising contradiction between simulation

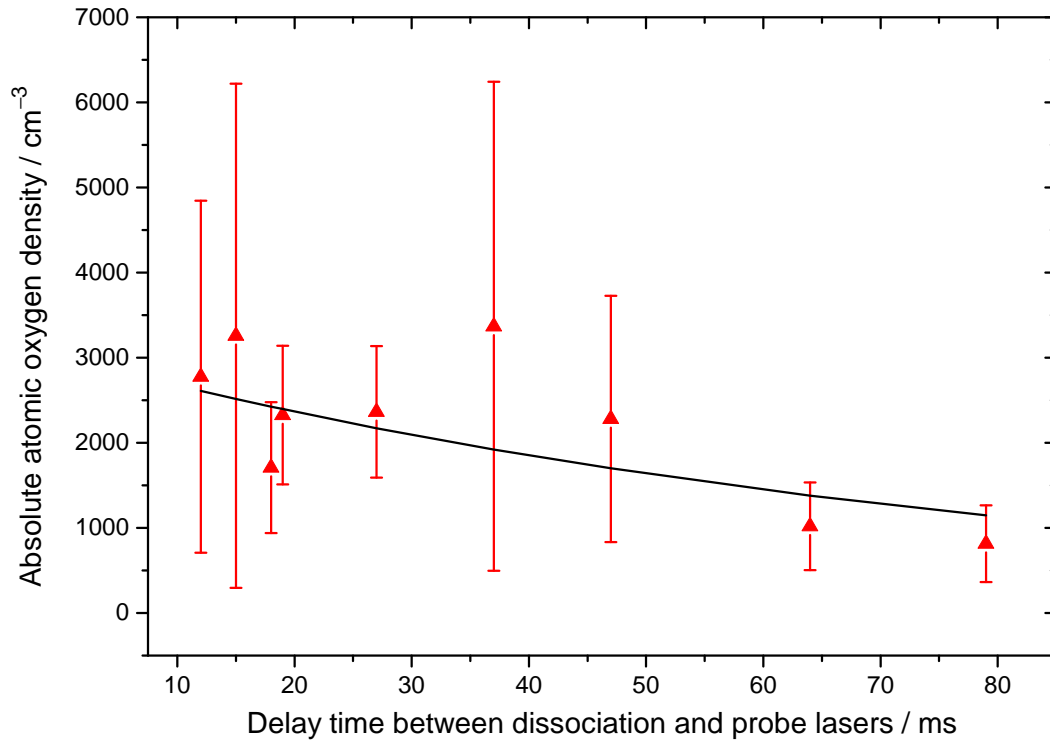


Figure 4.14: Red triangles: Background subtracted, magnetically trapped, atomic oxygen density as a function of delay between dissociation and probe lasers, error bars are one standard error. Black line: Weighted least-squares exponential fit with a  $1/e$  lifetime of  $82 \pm 3$  ms showing a maximum trapped density of  $3000 \pm 900$   $\text{cm}^{-3}$ .

and experiment could be caused by the density in the probing volume being significantly lower than that in the trapping volume at zero delay time. It could also be caused by saturation of the MCP detectors causing a lower reading at zero delay when the signal intensity is much higher than during trapping measurements. This was not unlikely as  $\text{O}^+$  impacted on only a small fraction of the detectors surface as the ion optics had a focusing effect on the ions to avoid collisions with the metal surface of the ion optics.

### 4.3.3 Conclusions

The trap lifetime measured here was more than double that of previous work on photostop of SH.<sup>34</sup> This was expected as atomic oxygen has a higher magnetic moment to mass ratio than SH, allowing higher velocities to be retained in a magnetic trap of the same depth. The lifetime was not as long as was hoped and so only a negligible fraction of the trapped atoms from a given photostop event would have survived to be present after the next event.

The density of trapped atomic oxygen measured here was lower than expected from simulation and comparison to previous photostop experiments. There were two reasons for this. The molecular beam had to be tuned to a lower intensity so as to reduce background one-colour signal from

photodissociation of  $\text{NO}_2$ , in the tail of the molecular beam, by the probe laser. This was done by increasing the spring tension sealing the valve such that, upon opening, a smaller hole would be created. Secondly to this, the  $\text{NO}_2$  in the molecular beam condensed onto the cryo-surfaces surrounding the trap, this both decreased the concentration of  $\text{NO}_2$  in the molecular beam and also blocked the beam from entering the trap to some extent. Although the icing was not as significant as with a xenon beam it still reduced the  $\text{NO}_2$  available for dissociation.

The density and trap lifetime achieved here could be improved by using a sharper and more intense molecular beam with a narrower velocity profile, for example the Nijmegen Pulsed Valve developed by B. Yan *et al.*<sup>78</sup> The use of a cryostat has distinct advantages in reducing background gas density, in future the magnetic trap should be mounted separately to the cryostat to eliminate the problem of condensation on the traps housing and allow the use of xenon instead of krypton which would result in an increased trap density of  $4600 \pm 1300 \text{ cm}^{-3}$ . A fully differentially pumped source chamber would also aid in reducing the background gas density, all these improvements should have a significant effect on the trap density and could be pursued in future work.

### Nijmegen pulsed valve

After significant work at optimisation, the General valve will give a pulse shown in fig. (2.2), FWHM's as low as  $120 \mu\text{s}$  are possible and the peak molecular density is likely to be less than  $10^{13}$  molecules /  $\text{cm}^3$ . The recently designed Nijmegen pulsed valve<sup>78</sup> (NPV) however is likely to give  $10^{14}$  molecules /  $\text{cm}^3$  at its peak with a FWHM below  $50 \mu\text{s}$ , this would mark a significant improvement for photostop. Not only would this allow more photostopped cold O or SH to be produced but also fewer molecules should follow the photostop event which could potentially reduce collisional trap loss. As well as this, more favourable velocity distributions in the beams peak are predicted.

The Nijmegen valve operates using the Lorentz force on a light weight magnetic strip. When closed, the strip has a small pin with a plug on its end that seals a conical 1 mm O-ring hole. The strip is attached to two Aluminium electrodes and is taught between them to provide a significant vertical force pushing the valve closed. The strip also sits close between two high field strength rare-earth magnets. When a current of up to 1 kA is applied through electrodes attached to the strip by a controllable TTL pulse, the strip experiences a force from the magnets that twists the metal such that the plug leaves the hole. Once the current pulse ends the plug then is forced by tension back into the hole thus sealing the valve. It has been reported that this valve has worked without fail for over  $10^8$  pulses, thus showing acceptable reliability. The valve is small and relatively simply constructed, the use of very light weight materials in the strip and cleverly designed electronics to allow huge currents with minimal power heating are important to this valve. The 1-2 W that passes through the strip and electrodes is relatively low thus allowing the valve to remain cool, an important feature to retain low and consistent translational temperatures in

the produced molecular beam. Use of this valve instead of the General valve would be the most effective upgrade for a photostop experiment.

Supporting data for the work presented in this chapter are available under open access through Durham University Collections at <https://doi.org/10.15128/r1z029p4763>.

## Chapter 5

# Unstable cluster detection

### 5.1 Introduction

As an aside to the Photostop work, this chapter will present work done on (1+1') resonance enhanced multiphoton ionisation (REMPI) of nitric oxide clusters with argon. This work was an extension of work done by the author and M. Litwinowicz. This previous work was described in great detail in a report (access can be provided by the author) by M. Litwinowicz and will only briefly be reviewed here to give context to the new work and external literature.<sup>79</sup>

This work was completed with the intention of developing (1+1') REMPI velocity map imaging (VMI) as a non-destructive, spectroscopically sensitive technique for measuring weakly bound molecular clusters. Specifically it was hoped that the technique could prevent the dissociation of weakly bound clusters when they were excited to a resonant Rydberg state before ionisation, with the intent of extending the technique to work on atmospherically relevant clusters scattering experiments. Some interesting results and no clear evidence of a reduction in cluster destruction by the use of (1+1') REMPI-VMI instead of (1+1) REMPI-VMI were found.

### 5.2 Background

NOAr clusters have been studied extensively due to ease of formation, largely as benchmark tests for electronic structure calculations involving long range dispersion forces or as archetypal van-der Waals clusters.<sup>79</sup> The exact energies of the NOAr cluster are to some extent disputed but are likely to be close to the values shown in fig. (5.1), it is agreed in the literature that the addition of an Ar atom has a stabilising effect that is most prominent in the ionic state and least in the Rydberg state. A large amount of the work done on these clusters has been to study their dissociation dynamics and products, this is likely at least partly due to the ease with which the clusters will dissociate.<sup>80,81</sup>

The purpose of this (1+1') REMPI experiment was to see if counter-intuitive pulse sequencing,

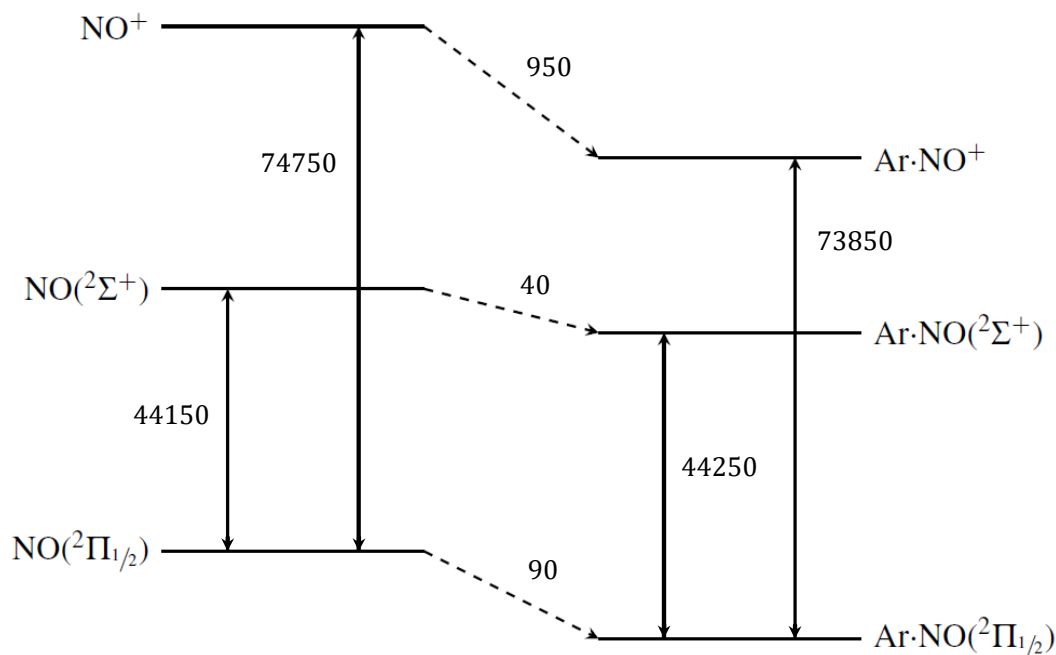


Figure 5.1: Molecular and cluster energy level diagram showing the ground, Rydberg and ionic states of NO and its ArNO cluster and the effect of clustering on the energies of the states, all energies given are in wavenumbers given to the nearest 10 to reflect small inconsistencies in literature values.<sup>79</sup>

similar to that used in Stimulated-Raman adiabatic-passage (STIRAP) experiments, could prevent the populating of a dissociative Rydberg intermediate state and thus provide a spectroscopically-sensitive soft ionisation method for unstable clusters that reduced cluster fragmentation. NOAr is a good candidate for this technique as its ground state geometry is a T-shape<sup>82</sup> but its excited state is linear,<sup>83</sup> this transition thus provides the necessary molecular rearrangement to cause cluster dissociation and so a method to bypass this state could reduce dissociation in the Rydberg state.

### 5.3 Previous work

Work was done using a similar experimental setup with only a single laser at 225/226 nm by the author and M. Litwinowicz. NOAr<sub>n</sub> clusters with n as high as 5 were detected and spectroscopic structure was observed for clusters with n=1 that was similar to that found in this work. Varying the conditions of the molecular beam source such as nozzle tension, nozzle opening time, backing pressure and the region of the molecular beam studied were shown to have an effect on the prevalence of cluster formation. A high backing pressure (5.5 Bar) with short opening time

(200  $\mu$ s) produced clusters most effectively in the coldest part of the molecular beam when the nozzle tension 'sweet spot' was found. These source conditions were used for work reported in this chapter.

## 5.4 Experimental

Fig. (4.1) shows the spectroscopic setup used for this experiment. The 225/226 nm laser was made in the same way as described in Chapter 4. The 323 nm laser was produced by doubling (KDP crystal) the output of a 532 nm pumped PDL dye laser containing DCM dye in DMSO. A custom delay line of appropriate length between oscillator and amplifier/pre-amplifier cells was introduced to the laser as the original optics could not be found. The 532 nm pumping light was generated by a Continuum Powerlite series laser and directed to the dye cells by dichroic mirrors. The 323 nm laser counter propagated against the 225/226 nm laser through the vacuum chamber. The lasers were overlapped temporally using a fast response photo-diode detector (ET-2000, Electro-Optics Technology) and tape measure. They were overlapped spatially at first by using the irises mounted beside the vacuum windows and then by maximising ion signal when the experiment was running.

The vacuum chamber was setup in the same way as described in chapter 4. The supersonic molecular beam was made by skimming (1 mm, Beam Dynamics) the output of a general valve with a 0.8 mm nozzle hole and a Teflon poppet. The nozzle tension, backing pressure and opening time were optimised according to previous work by the author and M. Litwinowicz. The chamber pressure under experimental conditions was typically  $2 \times 10^{-5}$  mBar and  $3 \times 10^{-7}$  mBar when the experiment was not running.

Data was collected by the same suite of programs described in Chapter 4 and the same VMI voltage conditions. The experiment was temporally sequenced in the same way as Chapter 4 with the addition of two channels in the pulse generator to control the timing of the 323 nm laser.

### 5.4.1 Fitting

Fig. (5.4) is fitted with a combination of two functions. The sharp rising edge at zero time delay is fitted to a Lorentzian function as this best represents the increase in laser power from the 225.95 nm laser with time. The longer decay is fitted to an exponential with a lifetime of 92 ns and all the data has had a constant (1+1) REMPI signal of 0.23 subtracted.

## 5.5 Results and discussion

A typical (1+1) REMPI VMI image of NOAr clusters, non-resonant NO signal and also thermal background NO signal is shown in fig. (5.2). The velocity profiles for the clustered and unclustered NO are comparable and show that the NOAr cluster was not fragmenting significantly during the ionisation process through a Rydberg state. VMI images of NO $\cdot$ Ar $_n$  with n greater than 1 (see



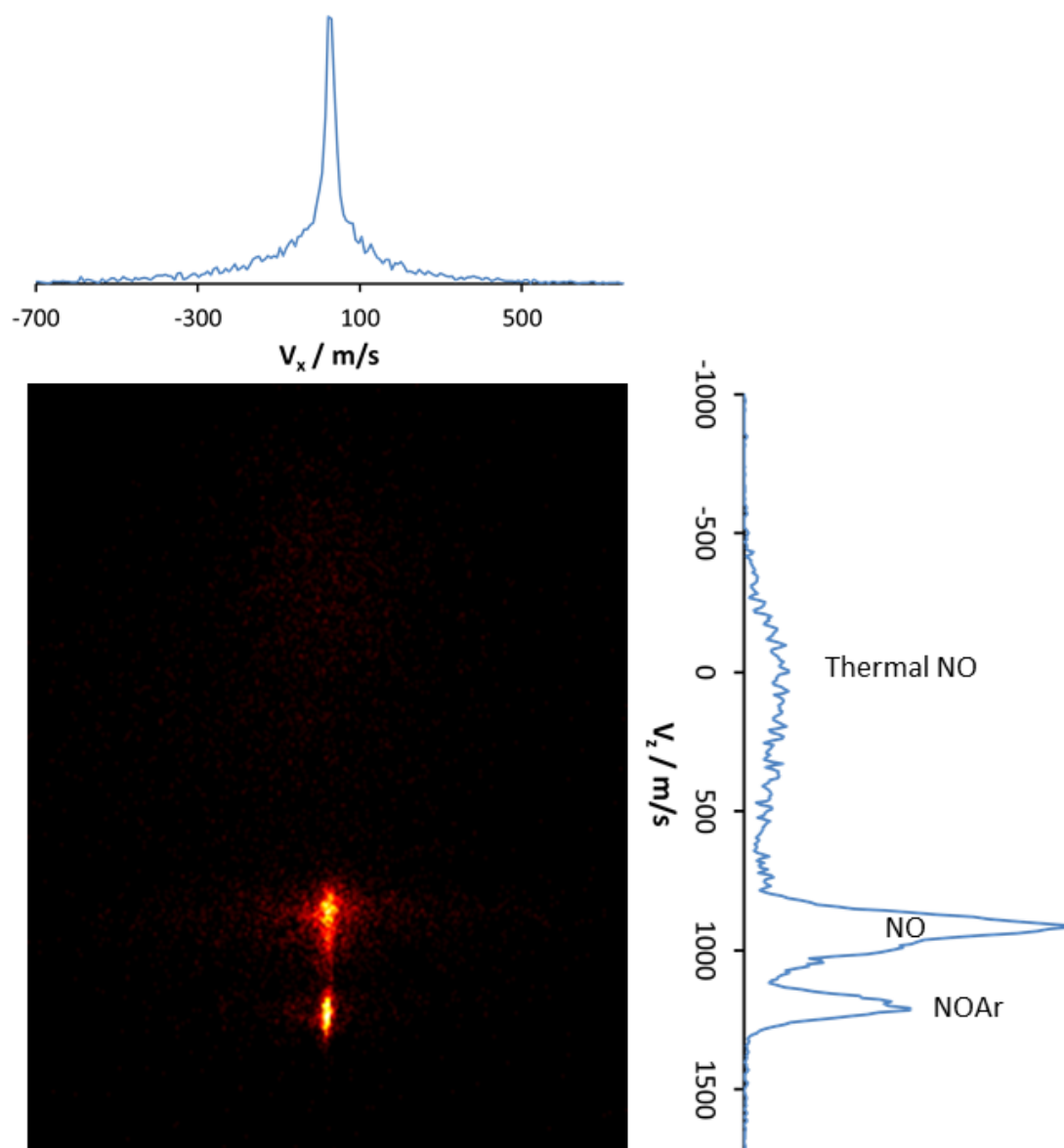


Figure 5.2: Velocity map image (crushed) taken without mass filtering to see NO, NOAr and thermal gas. Taken with a single laser wavelength at the NOAr fundamental transition (225.94 nm). Velocities are correct for NO mass fragments. The  $z$  axis corresponds to the molecular beam propagation direction and laser polarisation axis and the  $x$  to the laser propagation direction.

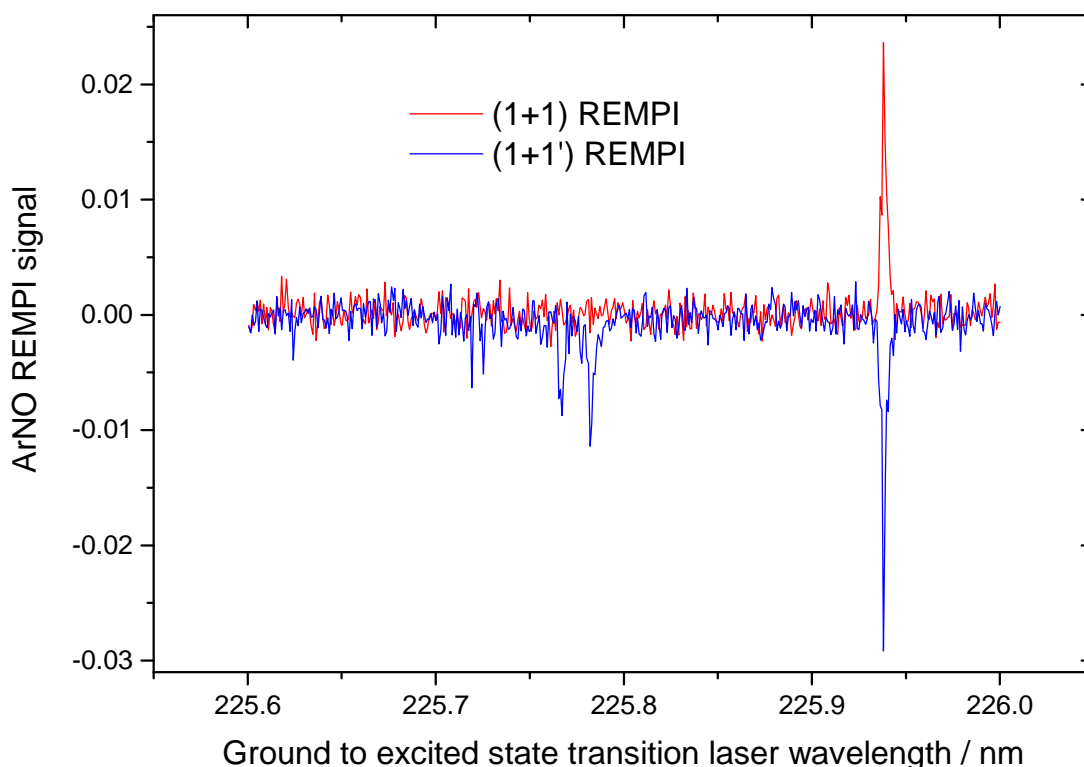


Figure 5.3: Spectra of ArNO clusters taken with (blue) and without (red) an additional 323 nm laser arriving 2 ns before the 226 nm laser. The fundamental transition (225.94 nm) is present in both spectra and the blue spectra features peaks corresponding to excited stretch vibrations of the ArNO (A) Rydberg state with rotational resolution.

M.Litwinowicz report) show significant fragmentation during ionisation which could not be reduced by (1+1') REMPI.

The REMPI spectrum taken in fig. (5.3) is comparable with spectra taken from literature although displays less structure than some external sources. Previous work by M. Litwinowicz had resolved excited stretch vibration transitions with a single laser, the lack of those transitions here should be attributed to a lower laser power.

Fig. (5.4) presents challenging data to interpret. It is standard for STIRAP (stimulated adiabatic Raman passage) experiments to feature signal enhancement by so called counter-intuitive pulse sequencing. This involves the laser pulse (P) dressing the intermediate to final state transition arriving before the pulse (S) dressing the initial and intermediate state. It should be made clear that this is not a STIRAP experiment but that the intention was to use counter-intuitive pulse sequencing to minimise population build up in the potentially dissociative or radiative Rydberg state.

It is not common for the P pulse to have a significant time gap before the S pulse arrives. In this experiment a time gap of up to 200 ns between the pulses still resulted in a measurable increase in NOAr<sup>+</sup> yield relative to the (1+1) REMPI experiment. The most intuitive way to interpret this

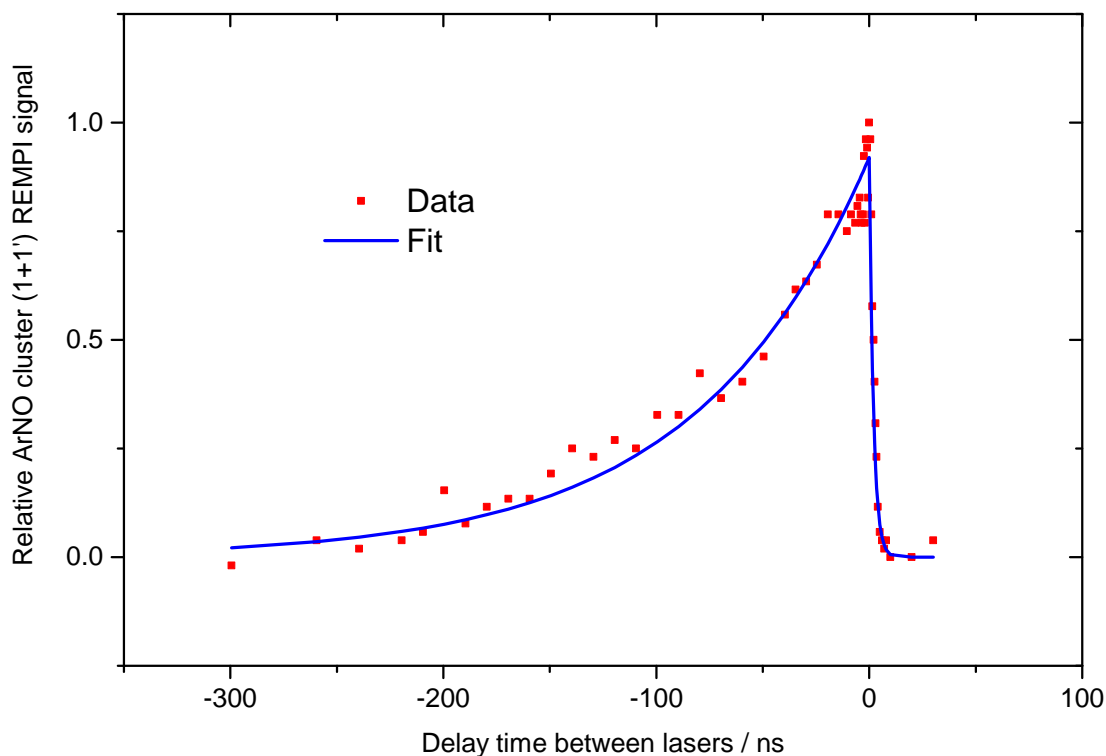


Figure 5.4: Time dependence of the (1+1') REMPI signal from NOAr clusters. A negative time delay implies the 323 nm arriving before the 225.95 nm whereas a positive delay has the 225.95 nm laser arriving first. The data was taken by averaging the TOF ion signal on an oscilloscope and then subtracting the constant (1+1) REMPI signal (signal of 0.23), the fit is an exponential fit with a sharp Lorentzian near zero time delay.

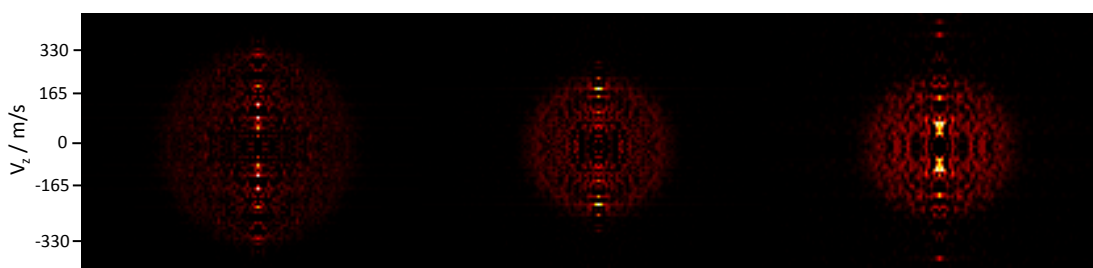


Figure 5.5: Sequence of velocity map images (reconstructed inverse Abel transformations) of non-resonant NO ions formed from photodissociation of NO-Ar<sub>n</sub> clusters. The left hand image was formed from counter-propagating, temporally and spatially overlapped lasers at 224.9 and 323.5 nm, the middle image from 225.3 and 323.5 nm and the right hand image from only 225.3 nm. V<sub>z</sub> is the molecular beam and laser polarisation axis. No clear difference is observed between the images with the exception of the change in size when increasing the 225/224 nm laser energy.

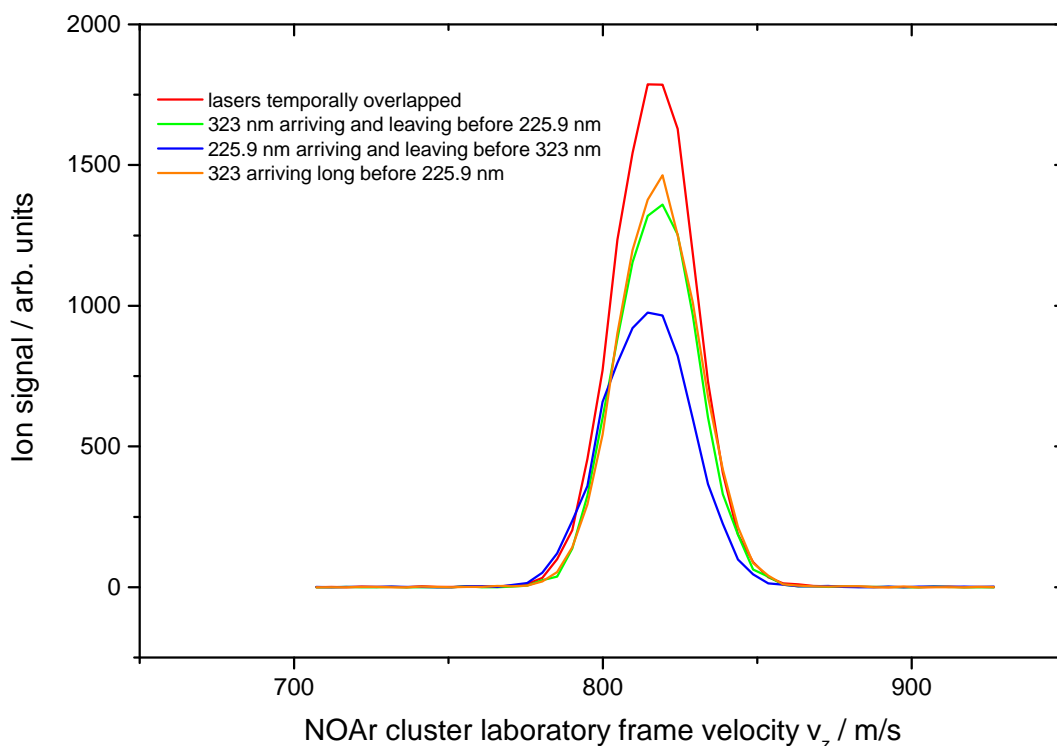


Figure 5.6: Velocity distributions of NOAr clusters taken under different laser field conditions, measured by  $(1+1')$  REMPI-VMI. All experimental conditions were constant except the timing of the lasers relative to each other.

result is that the P pulse is coupling the Rydberg and ionisation states of NOAr into a superposition of states. This superposition of states has a coherence lifetime given from the exponential decay of 92 ns. However this is not necessarily a legitimate interpretation of the data as this superposition would have been formed between two completely unoccupied molecular electronic states and the author is unsure if this is physically realistic or if this lifetime is meaningful.

The velocity map images in fig. (5.5) show the dissociation of NOAr clusters when excited to the Rydberg state with enough energy to overcome the binding energy of the cluster in that state. From this figure and additional work it was clear that the use of the 323 nm laser at varying time delays relative to the 225 nm laser had no qualitative influence on the appearance of the photodissociation spheres. Thus this provided no evidence to suggest  $(1+1')$  REMPI with STIRAP pulse ordering could bi-pass a dissociating Rydberg state and allow the clusters to retain their ground state bonding.

Fig. (5.6) effectively illustrates that the use of  $(1+1')$  REMPI relative to  $(1+1)$  REMPI increased NOAr<sup>+</sup> signal but had no influence on the velocity distribution of the ions, implying that any dissociation in the intermediate Rydberg state of NOAr was not quenched. It is possible that the  $(1+1')$  process could quench dissociation of larger clusters but no evidence of this was found.

## 5.6 Conclusion

The proposed development of a new technique for non-destructive ionisation of atmospherically relevant clusters has not been successful. Perplexing time dependent behaviour of the (1+1') REMPI was observed and NOAr cluster spectroscopic measurements were made that were consistent with the literature.

Although the (1+1') technique showed signal enhancement, it was not possible to measure spectroscopic resonances between the ionisation continuum and Rydberg state dressed by the 323 nm laser. Additionally the second laser did not allow for spectroscopic structure of larger clusters to be determined, this indicates but does not confirm that the technique does not reduce the dissociation of the clusters during the ionisation process. This data neither confirms or disproves the hypothesis that the use of (1+1') REMPI can provide a softer, rovibrationally state specific ionisation mechanism and reduce cluster dissociation in its intermediate Rydberg state.

Future work may be carried out on  $\text{HCl}(\text{H}_2\text{O})_n$  clusters using the (1+1') REMPI VMI detection technique to see if the technique is more successful with atmospherically relevant species.

Supporting data for the work presented in this chapter are available under open access through Durham University Collections at <https://doi.org/10.15128/r1pg15bd90j>.

## Chapter 6

# Conclusions and future work

These experiments demonstrate that photostop can produce trapped atomic and molecular radicals and thus satisfy the key aim of this body of work. The SH radical number density presented in Chapter 2 is only an estimate and still requires a successful experiment, improving on the work in Chapter 3, to confirm this number. The O atomic number density in Chapter 4 is based on measurement and so can be given a reliable confidence interval.

Although the trap densities achieved in this work for both SH and O are low compared with Stark and Zeeman deceleration or laser cooling experiments, this does not necessarily preclude sympathetic cooling in a vast excess of refrigerant atoms and combining photostop with a microwave trap would result in no foreseeable additional losses. The modest molecular-beam source used could be improved as discussed in Chapter 5, yielding up to a factor of ten increase in the number of trapped radicals by using the Neijmegen Pulsed Valve.

Additionally, a magnetic trap with a smaller volume and greater potential gradient would increase the trapped SH density. The modest trapping lifetime could be increased by improved differential pumping and by using a shorter and higher-density molecular beam pulse to minimise the amount of background gas in the trap. Alternatively the trapped cold species could be moved from the trapping location to another nearby trap, out of the way of the subsequent molecular beam pulses, this could potentially allow for build up of density from multiple photostop experiments. Simulation work to investigate this potential solution has been started by colleagues and is on-going but is beyond the scope of this thesis.

Photostop could be used to slow and trap other species such as SO, CN, CO, Cl, I and potentially even larger molecules. When determining if a candidate is suitable for photostop, one must consider several things and weigh up the probability of experimental success. The spectroscopic nature of the precursor molecule including its absorption cross-section, dissociation probability and mechanism and the availability of the necessary dissociation wavelength are all important. The physical properties of the precursor are also important as the molecule must be compatible with long term laboratory use and supersonic expansion, it must also be readily available or synthetically

feasible. Additionally the proposed method of detection of the photostop species must be considered alongside the likely background problems associated with detecting the cold molecules alongside their hot precursors, this is a challenging parameter to anticipate but can be crucial to the success of a photostop experiment. Any future photostop experiment must consider all these parameters.

Demonstrating the accumulation of a trapped photostop species is another experimental aim for the future. As photostop does not require opening and closing of the trap, it should be possible to accumulate molecular density from multiple molecular beam pulses. It was not possible to measure this effect in this thesis due to low densities and high background gas concentrations alongside relatively short trap lifetimes. To measure this in future the easiest method to employ would be to run the photostop trapping experiment at 10 Hz repetition rate and then again at 5 Hz. The experiment run at 10 Hz should result in a steady-state with a higher trap density than at 5 Hz as the trapped species will have less time to leave the trap between loading instances. Assuming that background gas can be evacuated between the molecular beam shots and does not build up as the experiment progresses.

The sympathetic cooling of triplet oxygen with ultracold Rb atoms could lead to an indirect cooling method for creating ultracold RbO (estimated electric dipole moment of 8.5 D) by coherent association of the ultracold atoms. This idea would involve the co-trapping of photostopped O atoms with magneto-optically trapped Rb atoms, followed by sympathetic cooling and coherent magneto or photoassociation. The necessary scattering theory calculations to find the location of potential Feshbach resonances for the association as well as the molecular simulation necessary to interrogate required sympathetic cooling lifetimes have not yet been performed. It is likely that more than an order of magnitude increase in atomic oxygen trapping lifetime would be required for this experiment to be successful.

# Appendix A

## Basic and Auxiliary Results

### A.1 Basic Results

#### A.1.1 Molecular beam mechanical chopper arm

Generating molecular beam sources with shorter temporal spreads, more intense maxima and a narrower distribution of particle velocities is useful for almost all pulsed molecular beam experiments. This experiment is no different, as the dissociation laser fires at or just after the concentration peak of the molecular beam, around half of the beam will fly ballistically through any cold molecules that are created by photostop, this will knock some cold molecules out of the trap. Another problem is that a small amount of effusive slow moving molecules from the General valve arrive at the trap so late that they can interact with the probe laser and generate one colour signal under conditions explained in chapters 2 and 4. To solve these problems there are two common solutions.

The choice is generally between a better quality molecular beam pulsed valve, most likely the Nijmegen valve,<sup>78</sup> that will shorten and sharpen the pulse or a chopper wheel that effectively chops the beam at either side into a narrower but no sharper source.<sup>84</sup>

A third option that was investigated here and in Edinburgh by S. Greeves and his group is that of a mechanical arm block. To make this shutter, a voice actuator coil (VAC) and arm are taken from a hard disk drive. A driving circuit has been designed by a group in Melbourne<sup>85</sup> that will allow quick opening and closing of the arm by the VAC through the use of an H-Bridge circuit and a capacitor of  $>200 \mu\text{F}$  in series with an  $110 \Omega$  resistor. The circuit allows for a TTL pulse to trigger a high current pulse by discharging the capacitor through the VAC, this rapidly accelerates the arm. Once the arm has moved from its start to its end position, the pulse of current is followed up by a holding current controlled by a resistor in parallel with the capacitor to hold the arm in place. These electronics allow for the arm to move as quickly as possible into the molecular beams path and thus shorten the width of the pulse. For the purposes of this experiment it was only necessary to trim the tail of the beam and block any slow moving molecules. The circuit was



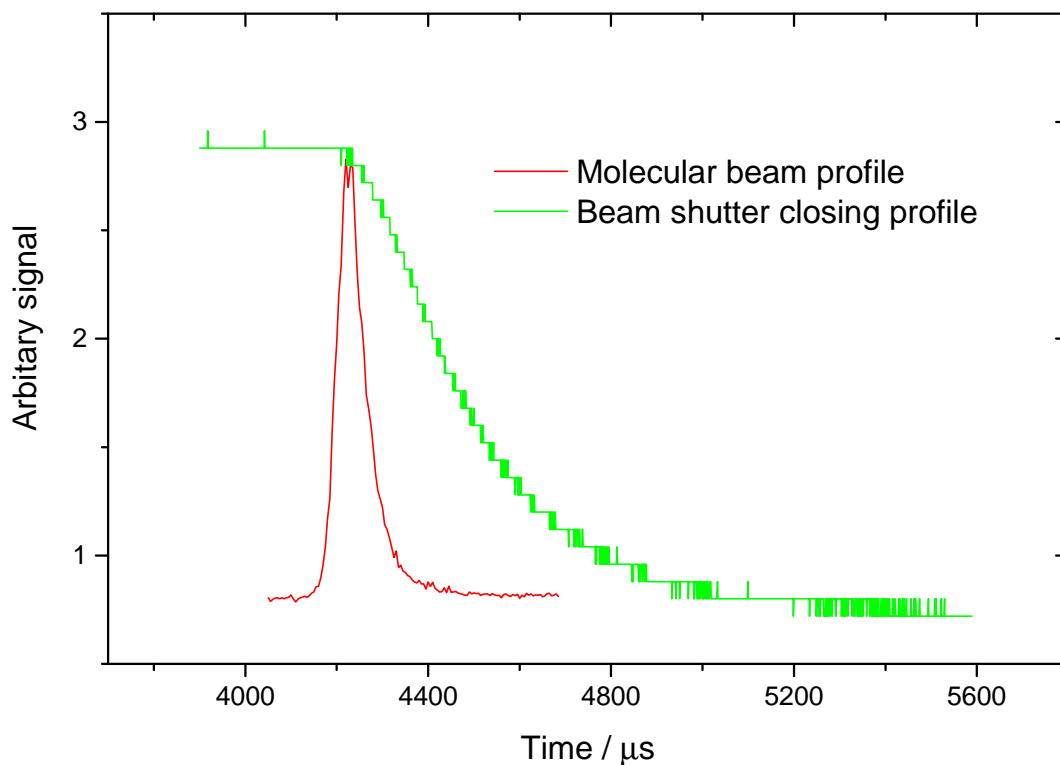


Figure A.1: Typical molecular beam profile from SH REMPI signal super-imposed against the fastest closing shutter profile possible. The shutter closing profile is measured by closing across a helium-neon laser of comparable width to the molecular beam that is detected by a nanosecond response time photodiode. It is clear that the shutter does not close rapidly enough to affect the main molecular beam.

therefore set to close fast and remain closed until opening again in the gap between experiments.

To achieve any meaningful change in the molecular beam profile, the shutter must close across the 3 mm beam profile in  $<200 \mu\text{s}$ . This means an average speed of 15 m/s must be reached across the beam profile. This is not an easy target and can only be achieved through the use of a very light weight but long shutter arm.

A shutter has been constructed that moves at speeds of up to 7 m/s. The shutter appeared to operate stably, however after an hour of constant operation at 5 Hz the arm started to break during deceleration, subsequent testing also resulted in significant heating of the VAC and component failure. As is clear from fig. (A.1) the current best shutter speed was not sufficient to have a significant effect on the molecular beam profile.

# Appendix B

## Derivations

### B.1 Explanation of oxygen REMPI absolute measurement

Here I give a brief explanation of the equations that lead to the determination of an ionisation efficiency for atomic oxygen REMPI. This derivation is based upon the more detailed work by D. J. Bamford *et al.*<sup>77</sup> and assume a square temporal probe laser pulse.

Let us imagine the REMPI process as a four state system, state 0 is the ground state with population  $n_0$ . State 1 is the Rydberg state to which the multiphoton absorption process excites, it has population  $n_1$ . State 2 is the ionised state of the system with population  $n_2$  and state three is a state that state 1 can decay into with a known decay rate  $K_f$  and population  $n_3$ .

The population in state 0 can be described by,

$$\frac{dn_0}{dt} = -\sigma^{(2)}F^2n_0, \quad (\text{B.1.1})$$

in which  $F$  represents the laser fluence in photons  $\text{cm}^{-2} \text{s}^{-1}$  and  $\sigma^{(2)}$  the two photon absorption cross section in  $\text{cm}^4 \text{s}$ . Also the population in state 1 is described by,

$$\frac{dn_1}{dt} = \sigma^{(2)}F^2n_0 - n_1(\sigma^iF + K_f), \quad (\text{B.1.2})$$

in which  $\sigma^i$  is the ionisation cross section from the Rydberg state in  $\text{cm}^2$ . Finally the population in state 2 can be described by,

$$\frac{dn_2}{dt} = n_1\sigma^iF, \quad (\text{B.1.3})$$

for brevity, I will exclude a population description of state 3 as it is not needed in the derivation. The important quantity here is  $n_2$ , as it is dependent on  $n_1$ , this must first be found. As we are interested only in the result of the REMPI process we can write an equation in  $n_1$  after REMPI has occurred,

$$n_1 = \left( \frac{\sigma^{(2)}F^2n_0}{K_f + \sigma^iF - \sigma^{(2)}F^2} \right) \left( \exp(-\sigma^{(2)}F^2\tau_p) - \exp((K_f + \sigma^iF)\tau_p) \right), \quad (\text{B.1.4})$$

in which  $\tau_f$  is the width of the laser pulse in seconds. Following this, a combination of eqn. (B.1.4) and eqn. (B.1.3) will give,

$$\frac{dn_2}{dt} = \left( \frac{\sigma^i \sigma^{(2)} F^3 n_0}{K_f + \sigma^i F - \sigma^{(2)} F^2} \right) \left( \exp(-\sigma^{(2)} F^2 \tau_p) - \exp(-(K_f + \sigma^i F) \tau_p) \right), \quad (\text{B.1.5})$$

this rate equation can then be used at a time after REMPI has occurred to give the ionised state population,

$$\frac{n_2}{n_0} = \left( \frac{\sigma^{(2)} \sigma^i F^3}{K_f + \sigma^i F - \sigma^{(2)} F^2} \right) \left( \frac{1 - \exp(-\sigma^{(2)} F^2 \tau_p)}{\sigma^{(2)} F^2} - \frac{1 - \exp(-(K_f + \sigma^i F) \tau_p)}{K_f + \sigma^i F} \right), \quad (\text{B.1.6})$$

this equation thus gives a linear relationship between the ground state population before REMPI and the ionised state population after REMPI. By using this equation with experimental parameters such as the MCP efficiency, the probing volume, the laser pulse width and the trap volume, an absolute value in atomic oxygen density can be assigned to every event measured on the MCP in the correct mass range.

# Appendix C

## Experimental proposals

### C.1 Super rotor using Photostop and Stark deceleration

Photostop could be combined with a linear decelerator that has already successfully focused and decelerated a molecule like OCS. The generation of slow molecules with high (near unity) rotational state purity from a decelerator allows for some interesting potential experiments.<sup>55</sup> Photostop could be used as the final stopping event on already decelerated state pure molecules. As well as being a stopping event, it could potentially be used to create translationally cold but rotationally hot molecular super rotors.

A super rotor is commonly described as a group of molecules that are quasi-bound as their rotational state is such that their rotational energy exceeds their molecular bonding strength, the rotors should also be vibrationally quantum state pure and rotating coherently. Rotating coherence is a specific quantum principle, a quantum system has rotational coherence if the  $t = 0$  spatial alignment of the wavefunctions probability density that make the systems wavepacket is reformed periodically in time at regular intervals and is subject to broadening. Thus coherence can be observed by an oscillating increasing and decreasing signal from a rotational wavepacket as in fig. (C.2). These coherent molecules often have lifetimes long enough for their study; however they will eventually be thermalised by inelastic collisions and become non-coherent. The inelastic collision rates responsible for thermalisation are approximately inversely proportional to the  $J$  rotational quantum number of the rotor and so a higher rotational speed will allow for longer lifetimes.

When a molecules rotational quantum number  $J$  exceeds 30 it becomes poor at thermalizing through collisions and losing its rotational energy, as demonstrated by Khodorkovsky *et al.*<sup>86</sup> As the rotational period becomes significantly less than the collision time, defined as the time molecules spend in the intermolecular potentials, the interactions between molecules become much

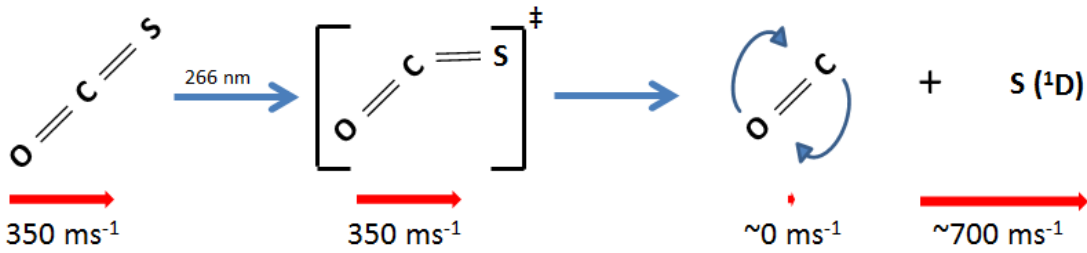


Figure C.1: Proposed scheme for creation of translationally cold CO super rotors by photostop of a stark aligned beam of OCS. The numbers quoted are a possible spectroscopic scheme that would photostop  $J = 36, 37$  and  $38$  with a 1-2 nm bandwidth laser or just  $J = 37$  with a narrow band laser.

more elastic. This phenomenon preventing rotational energy thermalisation is described by,

$$a = \frac{t_{\text{coll}}}{t_{\text{rot}}}, \quad (\text{C.1.1})$$

in which  $a$  is named the adiabaticity parameter and the times,  $t$ , are the times for collision and rotation respectively. As  $a$  increases, collisions become poorer at thermalizing a sample. Thus the lifetime of a sample of super rotors can be improved by increasing their rotational energy and lowering their translational energy. Although fig. (C.2) shows super rotor lifetimes of only 0.5 ns this figure is taken at atmospheric pressure and the lifetime is limited by collisions thus the use of a high vacuum system could significantly increase this lifetime as well as alignment to an axis instead of just a plane.

These factors make a potential photostop-stark deceleration experiment to form CO super rotors using an ultra-short femtosecond pulse smaller than the rotational period an interesting possibility as shown in fig. (C.1). Previous work<sup>87</sup> has shown that  $J > 30$  vibrationally cold CO molecules can be produced by photodissociation of OCS suggesting photostop could create translationally cold super rotors. Also, because a stark decelerator can select a single rotational state and spatially align it to an electric field, using a femtosecond laser for the photostop will allow the rotors to be rotating in phase coherently.

Photodissociation will produce molecules in a wide range of  $J$  states, only a few  $J$  states will be created at rest when the bandwidth of the laser pulse is taken into account. Previous experiments have used Raman spectroscopy to measure the rotational excitation and system coherence. The difficulty in applying this technique to cold molecules would be its poor sensitivity; a technique such as REMPI would have a much more suitable sensitivity and could perhaps be used instead.

Experiments have been proposed and conducted<sup>88</sup> to form long lived super rotors using optical centrifuges<sup>89</sup> which can potentially be combined with He buffer gas cooling to create cold super rotors in a molecular beam.<sup>90</sup> Briefly an optical centrifuge works by aligning a molecule to an often infrared polarised laser radiation field. The molecule aligns to the external field based on its

polarisability anisotropy,

$$U_0 = -\frac{1}{4}\Delta a E^2 \cos^2(\theta), \quad (\text{C.1.2})$$

the molecule experiences a potential energy  $U_0$ , dependent on the difference between the molecules parallel and perpendicular electric field polarisability  $\Delta a$  and the electric field  $E$  that will vary with the angle,  $\theta$ , between the radiation field and molecular axis. The plane of polarisation is then rotated at an increasing speed thus spinning a molecule based on its moment of inertia much like a normal centrifuge would. The process ends when the molecule is dissociated, leaves the radiation field as the polarisation spin changes too quickly such that  $U_0$  cannot contain the molecule or the laser field is stopped. If the process remains controlled and the molecules are simply released by an end to the radiation field then they will remain spinning at the end rotational frequency of the laser plane polarisation until they undergo collisions and exchange their rotational energy.

The proposed formation of quantum state pure super rotors poses some interesting quantum mechanical questions. In the formation of super rotors by optical centrifuges, the molecules can effectively rotate in a continuous range of frequencies. The coherent super rotors can be observed at a specific group rotational frequency and are coherent to that frequency but are not quantum state pure. Instead the wavepacket that describes the groups' coherence is made up of the wavefunctions of several individual rotational energy states in superposition, thus effectively any frequency can be made within the confines of the optics. This is illustrated by

$$\Psi(x, t) = \psi_E(x)e^{-\frac{iEt}{\hbar}} + \psi_{E'}(x)e^{-\frac{iE't}{\hbar}} \quad (\text{C.1.3})$$

$$|\Psi(x, t)|^2 = |\psi_E(x)|^2 + |\psi_{E'}(x)|^2 + 2\psi(x)\psi_{E'}(x)e^{-\frac{i(E'-E)t}{\hbar}} = f(t) \quad (\text{C.1.4})$$

where  $|\Psi(x, t)|^2$  is a particles normalised probability density when described by a linear combination of two Eigenfunctions,  $\psi_E(x)e^{-\frac{iEt}{\hbar}}$ , that are solutions to the time dependent Schrodinger equation. The third term in eqn. (C.1.4) describes the superposition of the linearly combined functions that creates a wavepacket. Crucially as the molecules rotational frequency coherence is a time varying property, unlike the systems energy, it must be described by a wavepacket and not a time-independent solution to the Schrodinger equation.<sup>91</sup> If  $\psi(x, t)$  is a single Eigenfunction then the probability density of the particle it describes is not dependent on a time coordinate and is described by

$$\Psi(x, t) = \psi_E(x)e^{-\frac{iEt}{\hbar}} \quad (\text{C.1.5})$$

$$|\Psi(x, t)|^2 = (\psi_E(x)e^{-\frac{iEt}{\hbar}}) \times (\psi_E(x)e^{-\frac{iEt}{\hbar}}) = |\psi_E(x)|^2 = f(x), \quad (\text{C.1.6})$$

in which the particles position probability is not time dependent and so cannot possess properties such as coherence.

However if cold super rotors were made by Photostop then intuitively the expected cold quantum system would contain only one rotational energy level as only one level would be at the correct

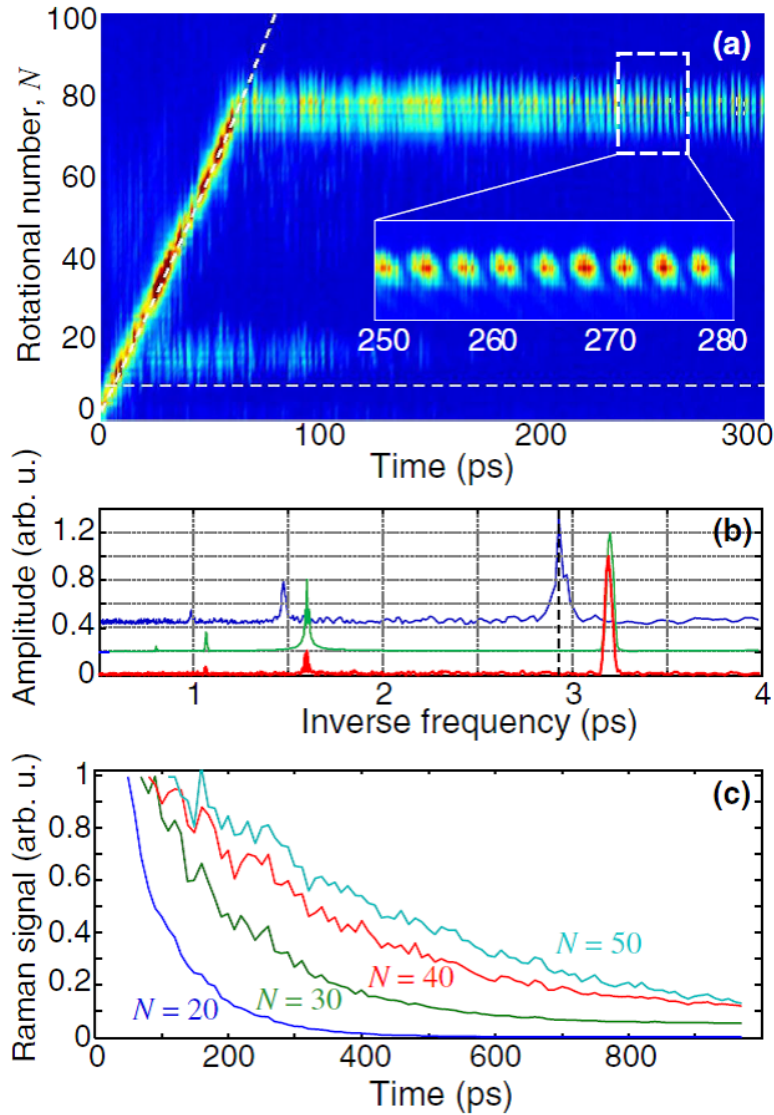


Figure C.2: top figure shows Raman scattered light intensity of super rotor  $O_2$  during a centrifuge spin (gradient) and oscillations of the coherent free rotational wavepacket that is left after spinning (flat line.) Middle figure shows a Fourier transform of the oscillation of the free wavepacket showing multiple constituent rotational frequencies for low rotational quantum number (blue) and high (green and red.) Final figure shows collisional lifetimes of super rotor molecules demonstrating the result of eqn. (C.1.1) giving longer lifetimes for higher rotational states, figure is taken from Korobenko *et al.*

photostop conditions. However the uncertainty principle forces a femtosecond laser to have a significantly larger bandwidth than a nanosecond laser, thus the bandwidth of the laser can span several rotational states and thus provide the correct photostop energy for multiple rotational states. Because of this the product ensemble can contain multiple wavefunctions and thus can display fractional revival of rotational coherence.

The experiment could be unsuccessful due to too long dissociation lifetimes relative to rotational periods which could completely blur any significant rotational coherence of the molecules. During dissociation, the ensemble wavepacket is projected onto the transition states potential energy surface and then back down to the product. This process is likely to take  $>100$  fs and could cause complete loss of coherence.

### **C.1.1 Photostop for creation of quantum state pure high rotational states**

In a very similar but crucially different vein to the possible super rotors experiment, a stark decelerated beam of OCS could be dissociated by an energetically narrow ns laser pulse to yield a rotationally excited state pure sample of cold and trappable CO. A significant advantage to photostopping and trapping high rotational states using a beam with a narrow velocity distribution and a low bandwidth laser is that nearby rotational states to the photostopped state will at their slowest be moving at over 50 m/s. This is in contrast to the SH trapping experiment in which high rotational states can be created with near zero laboratory frame velocity which is problematic for isolating the trappable species. This is due to the much larger energy gaps between rotational states at high  $J$  values.

This experiment could allow the study of quantum state pure translationally cold but rotationally hot molecules that could potentially be collided with other molecular beams to study high rotationally excited species scattering events.



# Bibliography

- [1] S. Y. T. van de Meerakker, H. L. Bethlem, N. Vanhaecke and G. Meijer, *Chemical Reviews*, 2012, **112**, 4828–4878.
- [2] N. Balakrishnan, *The Journal of Chemical Physics*, 2016, **145**, 150901.
- [3] B. K. Stuhl, M. T. Hummon and J. Ye, *Annual Review of Physical Chemistry*, 2014, **65**, 501–518.
- [4] L. D. Carr, D. DeMille, R. V. Krems and J. Ye, *New Journal of Physics*, 2009, **11**, 055049.
- [5] N. WARNER, *Doctoral*, Durham University, 2016.
- [6] S. Jochim, M. Bartenstein, A. Altmeyer, G. Hendl, S. Riedl, C. Chin, J. H. Denschlag and R. Grimm, *Science*, 2003, **302**, 2101–2103.
- [7] G. Scoles, *Atomic and Molecular Beam Methods*, Oxford University Press, 1988.
- [8] B. Yan, P. F. H. Claus, B. G. M. van Oorschot, L. Gerritsen, A. T. J. B. Eppink, S. Y. T. van de Meerakker and D. H. Parker, *Review of Scientific Instruments*, 2013, **84**, 023102.
- [9] S. Ospelkaus, K.-K. Ni, D. Wang, M. H. G. de Miranda, B. Neyenhuis, G. Quéméner, P. S. Julienne, J. L. Bohn, D. S. Jin and J. Ye, *Science*, 2010, **327**, 853–857.
- [10] J. J. Hudson, D. M. Kara, I. J. Smallman, B. E. Sauer, M. R. Tarbutt and E. A. Hinds, *Nature*, 2011, **473**, 493–U232.
- [11] J. Baron, W. C. Campbell, D. DeMille, J. M. Doyle, G. Gabrielse, Y. V. Gurevich, P. W. Hess, N. R. Hutzler, E. Kirilov, I. Kozyryev, B. R. O’Leary, C. D. Panda, M. F. Parsons, E. S. Petrik, B. Spaun, A. C. Vutha and A. D. West, *Science*, 2014, **343**, 269–272.
- [12] V. Zhelyazkova, A. Cournol, T. E. Wall, A. Matsushima, J. J. Hudson, E. A. Hinds, M. R. Tarbutt and B. E. Sauer, *Physical Review A*, 2014, **89**, 053416.
- [13] M. T. Hummon, T. V. Tscherebul, J. Kłos, H.-I. Lu, E. Tsikata, W. C. Campbell, A. Dalgarno and J. M. Doyle, *Physical Review Letters*, 2011, **106**, 053201.

- [14] M. H. Steinecker, D. J. McCarron, Y. Zhu and D. DeMille, *ChemPhysChem*, 2016, **17**, 3664–3669.
- [15] A. Prehn, M. Ibrügger, R. Glöckner, G. Rempe and M. Zeppenfeld, *Physical Review Letters*, 2016, **116**, 063005.
- [16] P. K. Molony, P. D. Gregory, Z. Ji, B. Lu, M. P. Köppinger, C. R. Le Sueur, C. L. Blackley, J. M. Hutson and S. L. Cornish, *Physical Review Letters*, 2014, **113**, year.
- [17] T. Shimasaki, M. Bellos, C. D. Bruzewicz, Z. Lasner and D. DeMille, *Physical Review A*, 2015, **91**, 021401.
- [18] C. E. Heiner, D. Carty, G. Meijer and H. L. Bethlem, *Nature Physics*, 2007, **3**, 115–118.
- [19] J. Lim, M. D. Frye, J. M. Hutson and M. R. Tarbutt, *Physical Review A*, 2015, **92**, 053419.
- [20] L. P. Parazzoli, N. J. Fitch, P. S. Żuchowski, J. M. Hutson and H. J. Lewandowski, *Physical Review Letters*, 2011, **106**, 193201.
- [21] A. O. G. Wallis and J. M. Hutson, *Physical Review Letters*, 2009, **103**, 183201.
- [22] A. O. G. Wallis, E. J. J. Longdon, P. S. Żuchowski and J. M. Hutson, *The European Physical Journal D*, 2011, **65**, arxiv:1009.5505.
- [23] T. V. Tscherbul, J. Klos and A. A. Buchachenko, *Physical Review A*, 2011, **84**, year.
- [24] M. Warehime and J. Klos, *Physical Review A*, 2015, **92**, 032703.
- [25] J. van Veldhoven, H. L. Bethlem and G. Meijer, *Physical Review Letters*, 2005, **94**, 083001.
- [26] D. P. Dunseith, S. Truppe, R. J. Hendricks, B. E. Sauer, E. A. Hinds and M. R. Tarbutt, *Journal of Physics B: Atomic, Molecular and Optical Physics*, 2015, **48**, 045001.
- [27] W. G. Doherty, M. T. Bell, T. P. Softley, A. Rowland, E. Wrede and D. Carty, *Physical Chemistry Chemical Physics*, 2011, **13**, 8441–8447.
- [28] C. J. Rennick, J. Lam, W. G. Doherty and T. P. Softley, *Physical Review Letters*, 2014, **112**, 023002.
- [29] A. Trottier, D. Carty and E. Wrede, *Molecular Physics*, 2011, **109**, 725–733.
- [30] A. Trottier, D. Carty and E. Wrede, *Molecular Physics*, 2011, **109**, 725–733.
- [31] B. Da-Xiao, D. Lian-Zhong, X. Liang and Y. Jian-Ping, *Chinese Physics B*, 2015, **24**, 113702.
- [32] C. J. Rennick, J. Lam, W. G. Doherty and T. P. Softley, *Physical Review Letters*, 2014, **112**, 023002.
- [33] N. WARNER, *Doctoral*, Durham University, 2016.

- [34] J. S. Eardley, N. Warner, L. Z. Deng, D. Carty and E. Wrede, *Phys. Chem. Chem. Phys.*, 2017, **19**, 8423–8427.
- [35] N. Wells and I. C. Lane, *Physical Chemistry Chemical Physics*, 2011, **13**, 19036.
- [36] D. P. Dunseith, S. Truppe, R. J. Hendricks, B. E. Sauer, E. A. Hinds and M. R. Tarbutt, *J. Phys. B: At. Mol. Opt. Phys.*, 2015, **48**, 045001.
- [37] B. Da-Xiao, D. Lian-Zhong, X. Liang and Y. Jian-Ping, *Chinese Physics B*, 2015, **24**, 113702.
- [38] B. Weiner, H. Levene, J. Valentini and A. Baronavski, *Journal of Chemical Physics*, 1989, **90**, 1403–1414.
- [39] S. Hoekstra, J. J. Gilijamse, B. Sartakov, N. Vanhaecke, L. Scharfenberg, S. Y. T. van de Meerakker and G. Meijer, *Physical Review Letters*, 2007, **98**, 133001.
- [40] A. Mizouri, L. Z. Deng, J. S. Eardley, N. H. Nahler, E. Wrede and D. Carty, *Physical Chemistry Chemical Physics*, 2013, **15**, 19575–19579.
- [41] H. Keller-Rudek, G. K. Moortgat, R. Sander and R. Sørensen, *Earth System Science Data*, 2013, **5**, 365–373.
- [42] J. B. Milan, W. J. Buma and C. A. deLange, *Journal of Chemical Physics*, 1996, **105**, 6688–6712.
- [43] M. Ashfold, W. Hartree, A. Salvato, B. Tutcher and A. Walker, *Journal of the Chemical Society-Faraday Transactions*, 1990, **86**, 2027–2034.
- [44] B. TUTCHER, *Ph.D. thesis*, Bristol University, 1988.
- [45] D. HIRST and M. GUEST, *Molecular Physics*, 1982, **46**, 427–435.
- [46] P. Bruna and G. Hirsch, *Molecular Physics*, 1987, **61**, 1359–1380.
- [47] C. Western, *PGOPHER*, <http://pgopher.chm.bris.ac.uk/>.
- [48] *The Python Language Reference — Python 2.7.11 Documentation*, <https://docs.python.org/2/reference/>.
- [49] S. I. Babic and C. Akyel, *Progress In Electromagnetics Research C*, 2008, **5**, 12.
- [50] B. K. Stuhl, M. T. Hummon, M. Yeo, G. Quemener, J. L. Bohn and J. Ye, *Nature*, 2012, **492**, 396–+.
- [51] G. Morley, I. Lambert, D. Mordaunt, S. Wilson, M. Ashfold, R. Dixon and C. Western, *J. Chem. Soc.-Faraday Trans.*, 1993, **89**, 3865–3875.

- [52] D. P. Dunseith, S. Truppe, R. J. Hendricks, B. E. Sauer, E. A. Hinds and M. R. Tarbutt, *Journal of Physics B: Atomic, Molecular and Optical Physics*, 2015, **48**, 045001.
- [53] D.-H. Lee, Y. Yoon, B. Kim, J. Y. Lee, Y. S. Yoo and J. W. Hahn, *Applied Physics B*, 2002, **74**, 435–440.
- [54] D. J. Wren, *Appl. Spectrosc., AS*, 1980, **34**, 627–632.
- [55] O. Nourbakhsh, J. M. Michan, T. Mittertreiner, D. Carty, E. Wrede, P. Djuricanin and T. Momose, *Molecular Physics*, 2015, **113**, 4007–4018.
- [56] J. Onvlee, S. N. Vogels and S. Y. T. van de Meerakker, *ChemPhysChem*, 2016, **17**, 3583–3595.
- [57] S. Hou, S. Li, L. Deng and J. Yin, *J. Phys. B-At. Mol. Opt. Phys.*, 2013, **46**, 045301.
- [58] M. Kirste, X. Wang, H. C. Schewe, G. Meijer, K. Liu, A. van der Avoird, L. M. C. Janssen, K. B. Gubbels, G. C. Groenenboom and S. Y. T. van de Meerakker, *Science*, 2012, **338**, 1060–1063.
- [59] Y. Liu, M. Vashishta, P. Djuricanin, S. Zhou, W. Zhong, T. Mittertreiner, D. Carty and T. Momose, *Phys. Rev. Lett.*, 2017, **118**, 093201.
- [60] H. L. Bethlem, G. Berden and G. Meijer, *Phys. Rev. Lett.*, 1999, **83**, 1558–1561.
- [61] Y. Nakano, Y. Hosho, K. Sadamori and T. Ishiwata, *Chem. Phys. Lett.*, 2012, **535**, 26–29.
- [62] E. S. Shuman, J. F. Barry and D. DeMille, *Nature*, 2010, **467**, 820–823.
- [63] A. M. Jayich, X. Long and W. C. Campbell, *Physical Review X*, 2016, **6**, 041004.
- [64] J. Jankunas, K. S. Reisman and A. Osterwalder, *Journal of Chemical Physics*, 2015, **142**, 104311.
- [65] T. Cremers, S. Chefdeville, V. Plomp, N. Janssen, E. Sweers and S. Y. T. van de Meerakker, *Physical Review A*, 2018, **98**, 033406.
- [66] I. C. Lane, *Physical Review A*, 2015, **92**, 022511.
- [67] F. Lique, J. Klos, M. H. Alexander, S. D. Le Picard and P. J. Dagdigian, *Monthly Notices of the Royal Astronomical Society*, 2018, **474**, 2313–2322.
- [68] E. Abrahamsson, R. V. Krems and A. Dalgarno, *The Astrophysical Journal*, 2007, **654**, 1171.
- [69] W. L. Wang, C. Rosa and J. Brandao, *Chemical Physics Letters*, 2006, **418**, 250–254.
- [70] D. Xie, C. Xu, T.-S. Ho, H. Rabitz, G. Lendvay, S. Y. Lin and H. Guo, *The Journal of Chemical Physics*, 2007, **126**, 074315.
- [71] A. T. J. B. Eppink and D. H. Parker, *Review of Scientific Instruments*, 1997, **68**, 3477–3484.

- [72] E. Wrede, S. Laubach, S. Schulenburg, A. Brown, E. R. Wouters, A. J. Orr-Ewing and M. N. R. Ashfold, *Journal of Chemical Physics*, 2001, **114**, 2629–2646.
- [73] D. M. Neumark, *Journal of Physical Chemistry A*, 2008, **112**, 13287–13301.
- [74] S. J. Matthews, S. Willitsch and T. P. Softley, *Phys. Chem. Chem. Phys.*, 2007, **9**, 5656–5663.
- [75] W. B. Gao, T. Hoger, J. B. Halpern and H. Zacharias, *Acta Physico-Chimica Sinica*, 2003, **19**, 875–878.
- [76] E. L. Flynn, *Doctoral*, Durham University, 2008.
- [77] D. J. Bamford, L. E. Jusinski and W. K. Bischel, *Physical Review A*, 1986, **34**, 185–198.
- [78] B. Yan, P. F. H. Claus, B. G. M. van Oorschot, L. Gerritsen, A. T. J. B. Eppink, S. Y. T. van de Meerakker and D. H. Parker, *Review of Scientific Instruments*, 2013, **84**, 023102.
- [79] A. M. Bush, J. M. Dyke, P. Mack, D. M. Smith and T. G. Wright, *Journal of Chemical Physics*, 1998, **108**, 406–415.
- [80] H. L. Holmes-Ross, R. J. Valenti, H.-G. Yu, G. E. Hall and W. D. Lawrance, *Journal of Chemical Physics*, 2016, **144**, 044309.
- [81] B. F. Parsons, D. W. Chandler, E. C. Sklute, S. L. Li and E. A. Wade, *The Journal of Physical Chemistry A*, 2004, **108**, 9742–9749.
- [82] Y. Sumiyoshi and Y. Endo, *Journal of Chemical Physics*, 2007, **127**, 184309.
- [83] H. Cybulski and B. Fernandez, *Journal of Physical Chemistry A*, 2012, **116**, 7319–7328.
- [84] J. Lam, C. J. Rennick and T. P. Softley, *Review of Scientific Instruments*, 2015, **86**, 053108.
- [85] R. E. Scholten, *Review of Scientific Instruments*, 2007, **78**, 026101.
- [86] Y. Khodorkovsky, U. Steinitz, J.-M. Hartmann and I. S. Averbukh, *Nat Commun*, 2015, **6**, 7791.
- [87] N. Sivakumar, I. Burak, W. Y. Cheung, P. L. Houston and J. W. Hepburn, *J. Phys. Chem.*, 1985, **89**, 3609–3611.
- [88] A. Korobenko, A. A. Milner and V. Milner, *Phys. Rev. Lett.*, 2014, **112**, 113004.
- [89] J. Karczmarek, J. Wright, P. Corkum and M. Ivanov, *Phys. Rev. Lett.*, 1999, **82**, 3420–3423.
- [90] W. H. al-Qady, R. C. Forrey, B. H. Yang, P. C. Stancil and N. Balakrishnan, *Phys. Rev. A*, 2011, **84**, 054701.
- [91] D. J. Tannor, *Introduction to Quantum Mechanics a Time-Dependent Perspective*, University science books, Sausalito, California, 1989.